# Mixed-Mode Oscillations with Multiple Time Scales*

Mathieu Desroches[†]
John Guckenheimer[‡]
Bernd Krauskopf[§]
Christian Kuehn[¶]
Hinke M. Osinga[§]
Martin Wechselberger[‖]

**Abstract.** Mixed-mode oscillations (MMOs) are trajectories of a dynamical system in which there is an alternation between oscillations of distinct large and small amplitudes. MMOs have been observed and studied for over thirty years in chemical, physical, and biological systems. Few attempts have been made thus far to classify different patterns of MMOs, in contrast to the classification of the related phenomena of bursting oscillations. This paper gives a survey of different types of MMOs, concentrating its analysis on MMOs whose small-amplitude oscillations are produced by a local, multiple-time-scale "mechanism." Recent work gives substantially improved insight into the mathematical properties of these mechanisms. In this survey, we unify diverse observations about MMOs and establish a systematic framework for studying their properties. Numerical methods for computing different types of invariant manifolds and their intersections are an important aspect of the analysis described in this paper.
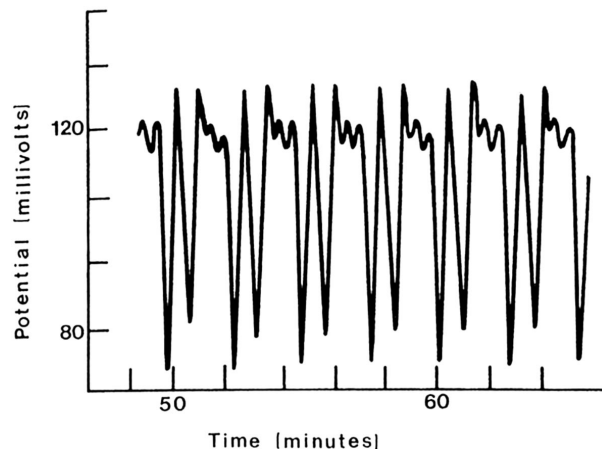
---

**Fig. 1** *Bromide ion electrode potential in the Belousov–Zhabotinsky reaction. Reprinted with permission from Hudson, Hart, and Marinko,* J. Chem. Phys., *71 (4), 1601–1606, (1979).* ©1979, *American Institute of Physics.*

**1. Introduction.** Oscillations with clearly separated amplitudes have been observed in several application areas, notably in chemical reaction dynamics. Figure 1 reproduces Figure 12 in Hudson, Hart, and Marinko [106]. It shows a time series of complex chemical oscillations of the Belousov–Zhabotinsky (BZ) reaction [18, 242] in a stirred tank reactor. The series appears to be periodic, and there is evident structure of the oscillations within each period. In particular, pairs of small-amplitude oscillations (SAOs) alternate with pairs of large-amplitude oscillations (LAOs). The result is an example of a *mixed-mode oscillation*, or MMO, displaying cycles of (at least) two distinct amplitudes. There is no accepted criterion for this distinction between amplitudes, but the separation between large and small is clear in the case of Figure 1. The pattern of consecutive large and small oscillations in an MMO is an aspect that draws immediate attention. Customarily, the notation $L_1^{s_1} L_2^{s_2} \cdots$ is used to label series that begin with $L_1$ LAOs, followed by $s_1$ SAOs, $L_2$ LAOs, $s_2$ SAOs, and so on. We will call $L_1^{s_1} L_2^{s_2} \cdots$ the MMO *signature*; it may be periodic or aperiodic. Signatures of periodic orbits are abbreviated by giving the signature of one period. Thus, the time series in Figure 1, which appears to be periodic, has signature $2^2$. As Hudson, Hart, and Marinko varied the flow rate through their reactor, MMOs with varied signatures were observed, as well as simple oscillations with only large or only small amplitudes. Similar results to those presented in their paper have been found in other experimental and model chemical systems. Additionally, MMOs have been observed in laser systems and in neurons. We present an overview with references to experimental studies of MMOs in these and other areas in Table 4 of the last section of this survey.

Dynamical systems theory studies qualitative properties of solutions of differential equations. The theory investigates bifurcations of equilibria and periodic orbits, describing how these limit sets depend upon system parameters. MMOs may be periodic orbits, but we then ask questions that go beyond those typically examined by standard/classical dynamical systems theory. Specifically, we seek to dissect the MMOs into their epochs of SAOs and LAOs, identify each of these epochs with geometric objects in the state space of the system, and determine how transitions are made

between them. When the transitions between epochs are much faster than the oscillations within the epochs, we are led to seek models for MMOs with multiple time scales.

Early studies of MMOs in model systems typically limited their investigations to cataloging the patterns of MMO signatures found as a parameter is varied. Barkley [16] is an exception: he assessed the capability of multiple-time-scale models for MMOs to produce the behavior observed by Hudson, Hart, and Marinko in [106]. He compared the MMOs from these experiments and from a seven-dimensional model for the BZ reaction proposed by Showalter, Noyes, and Bar-Eli [207] with three-dimensional multiple-time-scale models. Barkley was unable to produce a three-dimensional model with the qualitative characteristics of the MMOs in the larger model, but such models with many of the desired properties were subsequently found. This paper discusses two of these models, emphasizing the one proposed and studied by Koper [123]. Koper's model is similar to a normal form for singular Hopf bifurcation [87], a codimension-one bifurcation that arises in the context of systems with two slow variables and one fast variable. Our central focus is upon MMOs whose SAOs are a byproduct of local phenomena occurring in generic multiple-time-scale systems. Analogous to the role of normal forms in bifurcation theory, understanding the multiple-time-scale dynamics of MMOs in their simplest manifestations leads to insights into the properties of MMOs in more complex systems. We also revisit the Showalter, Noyes, and Bar-Eli model and highlight the role of multiple time scales in the MMOs of this example.

The geometry of multiple-time-scale dynamical systems is intricate. Section 2 provides a short review. Beginning with the work of the "Strasbourg" school [50] and Takens' work [216] on "constrained vector fields" in the 1970s, geometric methods have been used to study generic multiple-time-scale systems with two slow variables and one fast variable. *Folded singularities* are a prominent phenomenon in this work. As described in section 2, they lie on a fold of the *critical manifold*, where an attracting and a repelling sheet meet. Folded singularities yield equilibria of a *desingularized reduced vector field* that is constructed in the singular limit of the time-scale parameter. More recently, Dumortier and Roussarie [57] and Krupa, Szmolyan, and Wechselberger [144, 214] introduced singular blow-up techniques for the analytical study of the dynamics near folded singularities. These methods give information about *canard orbits* that connect attracting and repelling *slow manifolds*.

Canard orbits organize the number of SAOs for MMOs associated with folded nodes. The unfoldings of folded nodes [88, 237], folded saddle-nodes [86, 144], and singular Hopf bifurcations [87] give insight into the characteristics of MMOs and how they are formed as system parameters vary. Passage of trajectories through the region of a folded node is one mechanism for generating MMOs that we discuss at length in section 3.1 and illustrate with examples in sections 4 and 5. *Singular Hopf bifurcation* and the closely related *folded saddle-node bifurcation of type II* together constitute a second mechanism that produces SAOs and MMOs in a robust manner within systems having two slow variables and one fast variable. These bifurcations occur when a (true) equilibrium of the slow-fast system crosses a fold curve of a critical manifold. Singular Hopf bifurcation is discussed in section 3.2 and also illustrated in sections 4 and 5. We discuss a third mechanism for producing SAOs in slow-fast systems that is organized by a *Hopf bifurcation in the layer equations* and requires two fast variables. We call this mechanism a *dynamic Hopf bifurcation* and distinguish trajectories that pass by a dynamic Hopf bifurcation with a *delay* and trajectories with a *tourbillon* [235], whose SAOs have larger magnitude than those of a delayed Hopf bifurcation. Dynamic Hopf bifurcation is discussed in section 3.4 and illustrated in sections 6 and 7.

Complementary to theoretical advances in the analysis of slow-fast systems, numerical methods have been developed to compute and visualize geometric structures that shape the dynamics of these systems. Slow manifolds and canard orbits can now be computed in concrete systems; see Guckenheimer [87, 91] and Desroches, Krauskopf, and Osinga [42, 43, 44, 45]. The combination of new theory and new numerics has produced new understanding of MMOs in many examples that have been studied previously. This paper reviews and synthesizes these advances. It is organized as follows. Section 2 gives background about relevant parts of geometric singular perturbation theory. Multiple-time-scale mechanisms that produce SAOs in MMOs are then discussed and illustrated in section 3. The four subsequent sections provide case studies that illustrate and highlight recent theoretical advances and computational techniques. More details on the computational methods used in this paper can be found in section 8. The final section 9 includes a brief survey of the MMO literature and discusses other mechanisms that are not associated with a split between slow and fast variables.

**2. Geometric Singular Perturbation Theory of Slow-Fast Systems.** We consider here a slow-fast vector field that takes the form

$$(2.1) \qquad \begin{cases} \varepsilon\, \dot{x} = \varepsilon\, \frac{dx}{d\tau} = f(x, y, \lambda, \varepsilon), \\ \dot{y} = \quad \frac{dy}{d\tau} = g(x, y, \lambda, \varepsilon), \end{cases}$$

where $(x, y) \in \mathbb{R}^m \times \mathbb{R}^n$ are state-space variables, $\lambda \in \mathbb{R}^p$ are system parameters, and $\varepsilon$ is a small parameter $0 < \varepsilon \ll 1$ representing the ratio of time scales. The functions $f : \mathbb{R}^m \times \mathbb{R}^n \times \mathbb{R}^p \times \mathbb{R} \to \mathbb{R}^m$ and $g : \mathbb{R}^m \times \mathbb{R}^n \times \mathbb{R}^p \times \mathbb{R} \to \mathbb{R}^n$ are assumed to be sufficiently smooth, typically $C^\infty$. The variables $x$ are fast and the variables $y$ are slow. System (2.1) can be rescaled to

$$(2.2) \qquad \begin{cases} x' = \frac{dx}{dt} = f(x, y, \lambda, \varepsilon), \\ y' = \frac{dy}{dt} = \varepsilon\, g(x, y, \lambda, \varepsilon) \end{cases}$$

by switching from the slow time scale $\tau$ to the fast time scale $t = \tau/\varepsilon$.

Several viewpoints have been adopted to study slow-fast systems, starting with asymptotic analysis [58, 165] using techniques such as matched asymptotic expansions [119, 149]. Geometric singular perturbation theory (GSPT) takes a geometric point of view and focuses upon invariant manifolds, normal forms for singularities, and analysis of their unfoldings [10, 71, 113, 114, 218]. Fenichel's seminal work [71] on invariant manifolds was an initial foundation of GSPT and is also called Fenichel theory. A third viewpoint was adopted by a group of French mathematicians in Strasbourg. Using nonstandard analysis, they made many important discoveries [19, 20, 22, 23, 49, 50] about slow-fast systems. This paper adopts the GSPT viewpoint. We only focus on the results of GSPT that are necessary to study MMOs. There are other important techniques that are part of GSPT, such as the exchange lemma [113, 115], the blow-up method [57, 143, 237], and slow-fast normal form theory [10], that are not described in this paper.

**2.1. The Critical Manifold and the Slow Flow.** Solutions of a slow-fast system frequently exhibit slow and fast epochs characterized by the speed at which the solution advances. As $\varepsilon \to 0$, the trajectories of (2.1) converge during fast epochs to solutions of the *fast subsystem* or *layer equations*

$$(2.3) \qquad \begin{cases} x' = f(x, y, \lambda, 0), \\ y' = 0. \end{cases}$$

During slow epochs, on the other hand, trajectories of (2.2) converge to solutions of

(2.4)
$$\begin{cases} 0 = f(x, y, \lambda, 0), \\ \dot{y} = g(x, y, \lambda, 0), \end{cases}$$

which is a differential-algebraic equation (DAE) called the *slow flow* or *reduced system*. One goal of GSPT is to use the fast and slow subsystems (2.3) and (2.4) to understand the dynamics of the full system (2.1) or (2.2) for $\varepsilon > 0$. The algebraic equation in (2.4) defines the *critical manifold*

$$S := \{(x, y) \in \mathbb{R}^m \times \mathbb{R}^n \mid f(x, y, \lambda, 0) = 0\}.$$

We remark that $S$ may have singularities [142], but we assume here that this does not happen so that $S$ is a smooth manifold. The points of $S$ are equilibrium points for the layer equations (2.3).

Fenichel theory [71] guarantees persistence of $S$ (or a subset $M \subset S$) as a slow manifold of (2.1) or (2.2) for $\varepsilon > 0$ small enough if $S$ (or $M$) is *normally hyperbolic*. The notion of normal hyperbolicity is defined for invariant manifolds more generally, effectively stating that the attraction to and/or repulsion from the manifold is stronger than the dynamics on the manifold itself; see [68, 69, 70, 97] for the exact definition. Normal hyperbolicity is often difficult to verify when there is only a single time scale. However, in our slow-fast setting, $S$ consists entirely of equilibria and the requirement of normal hyperbolicity of $M \subset S$ is satisfied as soon as all $p \in M$ are hyperbolic equilibria of the layer equations, that is, the Jacobian $(D_x f)(p, \lambda, 0)$ has no eigenvalues with zero real part. We call a normally hyperbolic subset $M \subset S$ *attracting* if all eigenvalues of $(D_x f)(p, \lambda, 0)$ have negative real parts for $p \in M$; similarly, $M$ is called *repelling* if all eigenvalues have positive real parts. If $M$ is normally hyperbolic and neither attracting nor repelling, we say it is of *saddle type*.

Hyperbolicity of the layer equations fails at points on $S$ where its projection onto the space of slow variables is singular. Generically, such points are folds in the sense of singularity theory [10]. At a fold point $p_*$, we have $f(p_*, \lambda, 0) = 0$ and $(D_x f)(p_*, \lambda, 0)$ has rank $m - 1$ with left and right null vectors $w$ and $v$, such that $w \cdot [(D_{xx}^2 f)(p_*, \lambda, 0)(v, v)] \neq 0$ and $w \cdot [(D_y f)(p_*, \lambda, 0)] \neq 0$. These inequalities state that the tangencies of the critical manifold to the affine spaces of fast variables are similar to a quadratic function. Singularity theory makes the stronger statement that there are local coordinates in which the function $f$ becomes $y_1 = x_1^2$ [10]. The set of fold points forms a submanifold of codimension one in the $n$-dimensional critical manifold $S$. In particular, when $m = 1$ and $n = 2$, the fold points form smooth curves that separate attracting and repelling sheets of the two-dimensional critical manifold $S$. In this paper we do not consider more degenerate singular points of the projection of $S$ onto the space of slow variables.

Away from fold points the implicit function theorem implies that $S$ is locally the graph of a function $h(y) = x$. Then the reduced system (2.4) can be expressed as

(2.5)
$$\dot{y} = g(h(y), y, \lambda, 0).$$

We can also keep the DAE structure and write (2.4) as the restriction to $S$ of the vector field

(2.6)
$$\begin{cases} \dot{x} = \pm (D_x f)^{-1} (D_y f) \, g, \\ \dot{y} = g, \end{cases}$$

on $\mathbb{R}^m \times \mathbb{R}^n$ by observing that $f = 0$ and $\dot{y} = g$ imply $\dot{x} = \pm (D_x f)^{-1} (D_y f) g$. The vector field (2.6) blows up when $f$ is singular. It can be *desingularized* by scaling time by $\pm \det (D_x f)$, where we choose the sign so that the orientation of trajectories remains unchanged on the attracting sheets of $S$. This desingularized system plays a prominent role in much of our analysis. If $S$ is normally hyperbolic, not only $S$, but also the slow flow on $S$ persists for $\varepsilon > 0$; this is made precise in the following fundamental theorem.

THEOREM 2.1 (Fenichel's theorem [71]). *Suppose $M = M_0$ is a compact normally hyperbolic submanifold (possibly with boundary) of the critical manifold $S$ of (2.2) and that $f, g \in C^r$, $r < \infty$. Then for $\varepsilon > 0$ sufficiently small the following hold:*

(F1) *There exists a locally invariant manifold $M_\varepsilon$ diffeomorphic to $M_0$. Local invariance means that $M_\varepsilon$ can have boundaries through which trajectories enter or leave.*

(F2) *$M_\varepsilon$ has a Hausdorff distance of $O(\varepsilon)$ from $M_0$.*

(F3) *The flow on $M_\varepsilon$ converges to the slow flow as $\varepsilon \to 0$.*

(F4) *$M_\varepsilon$ is $C^r$-smooth.*

(F5) *$M_\varepsilon$ is normally hyperbolic and has the same stability properties with respect to the fast variables as $M_0$ (attracting, repelling, or saddle type).*

(F6) *$M_\varepsilon$ is usually not unique. In regions that remain at a fixed distance from the boundary of $M_\varepsilon$, all manifolds satisfying (F1)–(F5) lie at a Hausdorff distance $O(e^{-K/\varepsilon})$ from each other for some $K > 0$ with $K = O(1)$.*

*The normally hyperbolic manifold $M_0$ has associated local stable and unstable manifolds*

$$W_{\text{loc}}^s(M_0) = \bigcup_{p \in M_0} W_{\text{loc}}^s(p) \qquad and \qquad W_{\text{loc}}^u(M_0) = \bigcup_{p \in M_0} W_{\text{loc}}^u(p),$$

*where $W_{\text{loc}}^s(p)$ and $W_{\text{loc}}^u(p)$ are the local stable and unstable manifolds of $p$ as a hyperbolic equilibrium of the layer equations, respectively. These manifolds also persist for $\varepsilon > 0$ sufficiently small: there exist local stable and unstable manifolds $W_{\text{loc}}^s(M_\varepsilon)$ and $W_{\text{loc}}^u(M_\varepsilon)$, respectively, for which conclusions (F1)–(F6) hold if we replace $M_\varepsilon$ and $M_0$ by $W_{\text{loc}}^s(M_\varepsilon)$ and $W_{\text{loc}}^s(M_0)$ (or similarly by $W_{\text{loc}}^u(M_\varepsilon)$ and $W_{\text{loc}}^u(M_0)$).*

We call $M_\varepsilon$ a *Fenichel manifold*. Fenichel manifolds are a subclass of *slow manifolds*, invariant manifolds on which the vector field has speed that tends to 0 on the fast time scale as $\varepsilon \to 0$. We use the convention that objects in the singular limit have subscript 0, whereas the associated perturbed objects have subscripts $\varepsilon$. Geometrically, the stable manifold $W_{\text{loc}}^s(M_\varepsilon)$ of a Fenichel manifold $M_\varepsilon$ consists of points whose trajectories approach $M_\varepsilon$ in forward time; similarly, $W_{\text{loc}}^u(M_\varepsilon)$ consists of points whose trajectories approach $M_\varepsilon$ in backward time.

**2.1.1. The Critical Manifold and the Slow Flow in the Van der Pol Equation.** Let us illustrate these general concepts of GSPT with an example. One of the simplest systems in which the concepts are manifest, and historically perhaps also the first, is the Van der Pol equation [225, 226, 227] with constant forcing $\lambda \in \mathbb{R}$ given by

(2.7)
$$\begin{cases} \varepsilon \dot{x} = y - \frac{1}{3}x^3 + x, \\ \dot{y} = \lambda - x. \end{cases}$$

This slow-fast system has only one fast and one slow variable, but it already exhibits complicated dynamics that were truly surprising when they were first discovered [50]. By setting $\varepsilon = 0$ in (2.7), we obtain the reduced system with an algebraic equation
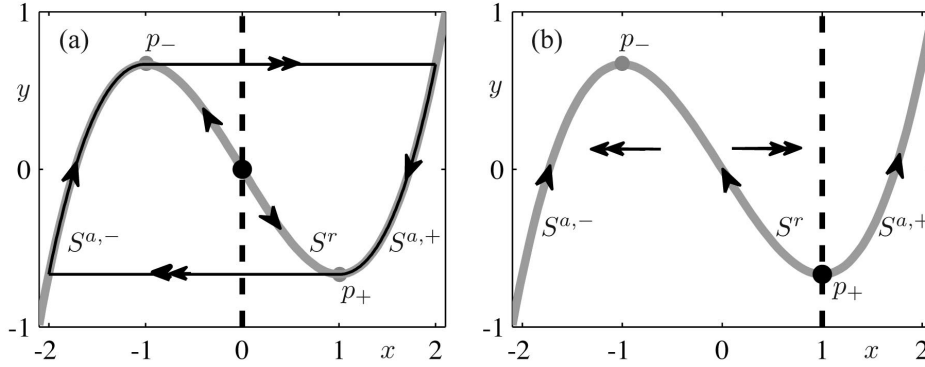
**Fig. 2** *Phase portraits of the Van der Pol equation (2.7) for $\lambda = 0$ (a) and for $\lambda = 1$ (b). Shown are the critical manifold $S$ (gray solid curve) and the $y$-nullcline (dashed line); double arrows indicate the direction of the fast flow and single arrows that of the slow flow. Panel (a) shows a candidate for a relaxation oscillation (black) surrounding an unstable equilibrium. Panel (b) is the moment of the singular Hopf bifurcation with a folded singularity at the local minimum $p_+$.*

that defines the critical manifold of (2.7) as the cubic curve

$$(2.8) \qquad S = \{(x,y) \in \mathbb{R}^2 \mid y = \tfrac{1}{3}x^3 - x =: c(x)\}.$$

It is normally hyperbolic away from the local minimum and maximum $p_\pm = (\pm 1, \mp \tfrac{2}{3})$ of the cubic, where $S$ has a fold with respect to the fast variable $x$. At $p_\pm$ normal hyperbolicity fails, since $\frac{\partial}{\partial x} f(x, y, \lambda, 0) = 1 - x^2$ is zero at $p_\pm$. Hence, $p_\pm$ are the fold points and they naturally decompose the critical manifold into three branches,

$$S = S^{a,-} \cup \{p_-\} \cup S^r \cup \{p_+\} \cup S^{a,+},$$

where $S^{a,-} := S \cap \{x < -1\}$, $S^{a,+} := S \cap \{x > 1\}$, and $S^r = S \cap \{-1 < x < 1\}$. From the sign of $\frac{\partial}{\partial x} f(x, y, \lambda, 0)$ we conclude that the two branches $S^{a,-}$ and $S^{a,+}$ are attracting, and the branch $S^r$ is repelling. The critical manifold $S$ is shown as the gray cubic curve in Figure 2; note that $S$ and its attracting/repelling nature does not depend on $\lambda$, so it is the same in both panel (a), where $\lambda = 0$, and panel (b), where $\lambda = 1$. The dynamics of any point not on $S$ is entirely controlled by the direction of the fast variable $x$, which is indicated in Figure 2 by the horizontal double arrows; observe that the middle branch of $S$ is repelling and the two unbounded branches are attracting.

To obtain the slow flow (2.5) on $S$ in the Van der Pol equation (2.7) it is not actually necessary to solve the cubic equation $y = c(x)$ for $x$ on $S^{a,-}$, $S^r$, and $S^{a,+}$. It is more convenient to write the slow (reduced) flow in terms of the fast variable $x$. To this end, we differentiate $f(x, y, \lambda, 0) = y - c(x) = 0$ with respect to $\tau$ and obtain

$$\dot{y} = \dot{x}\, x^2 - \dot{x} = \dot{x}\, (x^2 - 1).$$

Combining this result with the equation for $\dot{y}$ we get

$$(2.9) \qquad (x^2 - 1)\, \dot{x} = \lambda - x \qquad \text{or} \qquad \dot{x} = \frac{\lambda - x}{x^2 - 1}.$$

The direction of the slow flow on $S$ is indicated in Figure 2 by the arrows on the gray curve. The slow flow does depend on $\lambda$, because the direction of the flow is partly determined by the location of the equilibrium at $x = \lambda$ on $S$. The slow flow is well defined on $S^{a,-}$, $S^r$, and $S^{a,+}$, but not at $x = \pm 1$ (as long as $\lambda \neq \pm 1$). We can desingularize the slow flow near $x = \pm 1$ by rescaling time with the factor $(x^2 - 1)$. This gives the equation $\dot{x} = \lambda - x$ of the *desingularized reduced flow*. Note that this time rescaling reverses the direction of time on the repelling branch $S^r$, so care must be taken when relating the phase portrait of the desingularized system to the phase portrait of the slow flow.

Let us now focus specifically on the case for $\lambda = 0$, shown in Figure 2(a), because it is representative for the range $|\lambda| < 1$. The $y$-nullcline of (2.7), defined by $\dot{y} = 0$, is shown as the dashed black vertical line (the $x$-nullcline is $S$) and the origin is the only equilibrium, which is a source for this value of $\lambda$. The closed curve is a singular orbit composed of two fast trajectories starting at the two fold points $p_\pm$ concatenated with segments of $S$. Such continuous concatenations of trajectories of the layer equations and the slow flow are called *candidates* [20]. The singular orbit follows the slow flow on $S$ to a fold point, then it *jumps*, that is, it makes a transition to a fast trajectory segment that flows to another branch of $S$. The same mechanism returns the singular orbit to the initial branch of $S$. It can be shown [143, 165] that the singular orbit perturbs for $\varepsilon > 0$ to a periodic orbit of the Van der Pol equation that lies $O(\varepsilon^{2/3})$ close to this candidate. Van der Pol introduced the term *relaxation oscillation* to describe periodic orbits that alternate between epochs of slow and fast motion.

**2.2. Singular Hopf Bifurcation and Canard Explosion.** The dynamics of slow-fast systems in the vicinity of points on the critical manifold where normal hyperbolicity is lost can be surprisingly complicated and nothing like what we know from systems with a single time scale. This section addresses the phenomenon known as a *canard explosion*, which occurs in planar slow-fast systems after a *singular Hopf bifurcation*. We discuss this first for the example of the Van der Pol equation (2.7).

**2.2.1. Canard Explosion in the Van der Pol Equation.** As mentioned above, the phase portrait in Figure 2(a) is representative of a range of $\lambda$-values. However, the phase portrait for $\lambda = 1$, shown in Figure 2(b), is degenerate. Linear stability analysis shows that for $\varepsilon > 0$ the unique equilibrium point $(x, y) = (\lambda, \frac{1}{3}\lambda^3 - \lambda)$ is a source for $|\lambda| < 1$, but a sink for $|\lambda| > 1$. A Hopf bifurcation occurs for $\lambda = \pm 1$. A *Hopf bifurcation* of a dynamical system is characterized by a simple pair of purely imaginary eigenvalues at an equilibrium point crossing the imaginary axis with nonzero speed as a parameter is varied [148]. As a result, one finds a family of periodic orbits emerging from the bifurcation point. One distinguishes two generic cases: the *supercritical* Hopf bifurcation where the bifurcating periodic orbits are stable, and the *subcritical* Hopf bifurcation where the bifurcating periodic orbits are unstable. The type of Hopf bifurcation is determined by the sign of the *Lyapunov coefficient* (the coefficient of the third-order term in the associated Hopf normal form), which is required to be nonzero for the Hopf bifurcation to be generic. Near a generic Hopf bifurcation, the amplitude of the periodic orbits is comparable to the square root of the distance of the parameter to the bifurcation point. For the Van der Pol equations (2.7) a supercritical Hopf bifurcation occurs at $\lambda_H = \pm 1$, and the bifurcating periodic orbits exist in the parameter interval $|\lambda| < 1$.

The analysis of how the observed stable dynamics of the Van der Pol equation (2.7) changes with $\lambda$ from a stable focus to relaxation oscillations when $\varepsilon > 0$ is small was a major development in the theory of slow-fast systems. Figure 3(a) shows the result
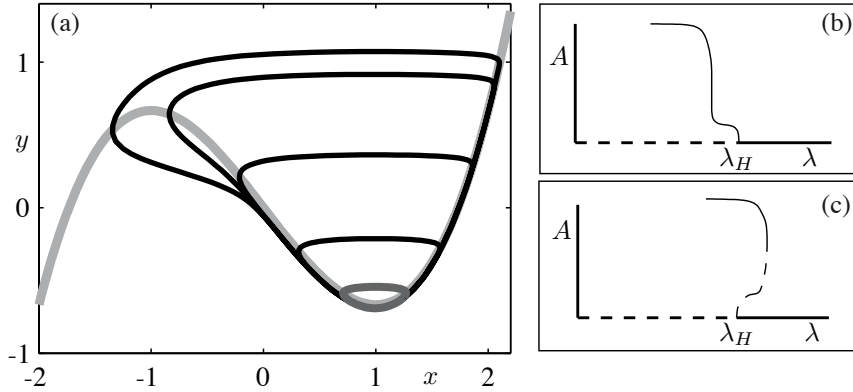
**Fig. 3** *Numerical continuation of periodic orbits in the Van der Pol equation (2.7) for $\varepsilon = 0.05$. Panel (a) shows a selection of periodic orbits: the dark gray orbit is a typical small limit cycle near the Hopf bifurcation at $\lambda = \lambda_H$, whereas all the black orbits occur in a very small parameter interval at $\lambda \approx 0.993491$. Panels (b) and (c) are sketched bifurcation diagrams corresponding to supercritical and subcritical singular Hopf bifurcations; here, A denotes the amplitude of the limit cycle.*

of a numerical continuation in the parameter $\lambda$ of the periodic orbit for $\varepsilon = 0.05$ that emerges from the Hopf bifurcation. Close to the Hopf bifurcation at $\lambda_H = 1.0$ the periodic orbit (dark gray curve) is small, as is to be expected. However, as $\lambda$ decreases, the periodic orbit grows very rapidly, where it follows the repelling slow manifold $S_\varepsilon^r$ for a long time. In fact, the values of $\lambda$ for all black orbits in Figure 3(a) are $\lambda \approx 0.993491$, that is, they agree to six decimal places. Note that we show the growing orbits only up to a characteristic intermediate size: the largest periodic orbit in Figure 3(a) just encompasses the fold point $p_-$. Upon further continuation in $\lambda$ this periodic orbit continues to grow rapidly until it reaches the shape of a relaxation oscillation; compare with Figure 2(a).

The Hopf bifurcation at $\lambda_H = 1$ occurs when the equilibrium moves over the fold point $p_+$. It is called a singular Hopf bifurcation. The eigenvalues at the Hopf bifurcation have magnitude $O(\varepsilon^{-1/2})$, so that the periodic orbit is born at the Hopf bifurcation with an intermediate period between the fast $O(\varepsilon^{-1})$ and slow $O(1)$ time scales. The size of this periodic orbit grows rapidly from diameter $O(\varepsilon^{1/2})$ to diameter $O(1)$ in an interval of parameter values $\lambda$ of length $O(\exp(-K/\varepsilon))$ (for some $K > 0$ fixed) that is $O(\varepsilon)$ close to $\lambda_H$. Figures 3(b) and (c) are sketches of possible bifurcation diagrams in $\lambda$ for the singular Hopf bifurcation in a supercritical case (which one finds in the Van der Pol system) and in a subcritical case, respectively; the vertical axis represents the maximal amplitude of the periodic orbits. The two bifurcation diagrams are sketches that highlight the features described above. There is a very small interval of $\lambda$ where the amplitude of the oscillation grows in a square-root fashion, as is to be expected near a Hopf bifurcation [148]. However, the amplitude then grows extremely rapidly until it reaches a plateau that corresponds to relaxation oscillations.

The rapid growth in amplitude of the periodic orbit near the Hopf bifurcation is called a *canard explosion*. The name canard derives originally from the fact that some periodic orbits during the canard explosion look a bit like a duck [50]. In fact, the largest periodic orbit in Figure 3(a) is an example of such a "duck-shaped" orbit. More generally, and irrespective of its actual shape, one now refers to a trajectory as a

*canard orbit* if it follows a repelling slow manifold for a time of $O(1)$ on the slow time scale. A canard orbit is called a *maximal canard* if it joins attracting and repelling slow manifolds. Since the slow manifolds are not unique, this definition depends upon the selection of specific attracting and repelling slow manifolds; compare (F6) of Theorem 2.1. Other choices yield trajectories that are exponentially close to one another. In the Van der Pol equation (2.7) the canard explosion occurs $O(e^{-K/\varepsilon})$-close in parameter space to the point where the manifolds $S_\varepsilon^{a,+}$ and $S_\varepsilon^r$ intersect in a maximal canard. It is associated with the parameter value $\lambda = 1$, where the equilibrium lies at the fold point $p_+$ of the critical manifold $S$; see Figure 2(b).

**2.3. Singular Hopf Bifurcation and Canard Explosion in Generic Planar Systems.** In the Van der Pol equation (2.7) the singular Hopf bifurcation takes place at $\lambda = 1$, where the equilibrium lies at a fold point. In a generic family of slow-fast planar systems a singular Hopf bifurcation does not happen exactly at a fold point, but at a distance $O(\varepsilon)$ in both phase space and parameter space from the coincidence of the equilibrium and the fold point. One can obtain a generic family by modifying the slow equation of the Van der Pol equation (2.7) to

$$\dot{y} = \lambda - x + a\,y.$$

In this modified system the equilibrium and the fold point still coincide at $x = 1$, but the Hopf bifurcation occurs for $x = \sqrt{1 + \varepsilon\,a}$. A detailed dynamical analysis of canard explosion and the associated singular Hopf bifurcation using geometric or asymptotic methods exists for planar slow-fast systems [12, 13, 57, 58, 141, 143]; we summarize these results as follows.

THEOREM 2.2 (canard explosion in $\mathbb{R}^2$ [143]). *Suppose a planar slow-fast system has a generic fold point $p_* = (x_p, y_p) \in S$, that is,*

(2.10)

$$f(p_*, \lambda, 0) = 0, \quad \frac{\partial}{\partial x} f(p_*, \lambda, 0) = 0, \quad \frac{\partial^2}{\partial x^2} f(p_*, \lambda, 0) \neq 0, \quad \frac{\partial}{\partial y} f(p_*, \lambda, 0) \neq 0.$$

*Assume the critical manifold is locally attracting for $x < x_p$ and repelling for $x > x_p$ and there exists a folded singularity for $\lambda = 0$ at $p_*$, namely,*

(2.11)        $$g(p_*, 0, 0) = 0, \quad \frac{\partial}{\partial x} g(p_*, 0, 0) \neq 0, \quad \frac{\partial}{\partial \lambda} g(p_*, 0, 0) \neq 0.$$

*Then a singular Hopf bifurcation and a canard explosion occur at*

(2.12)                                        $$\lambda_H = H_1\,\varepsilon + O(\varepsilon^{3/2}) \qquad and$$
(2.13)                                        $$\lambda_c = (H_1 + K_1)\,\varepsilon + O(\varepsilon^{3/2}).$$

*The coefficients $H_1$ and $K_1$ can be calculated explicitly from normal form transformations [143] or by considering the first Lyapunov coefficient of the Hopf bifurcation [145].*

In the singular limit we have $\lambda_H = \lambda_c$. For any $\varepsilon > 0$ sufficiently small, the linearized system [90, 148] at the Hopf bifurcation point has a pair of *singular eigenvalues* [27]

$$\sigma(\lambda; \varepsilon) = \alpha(\lambda; \varepsilon) + i\,\beta(\lambda; \varepsilon),$$

with $\alpha(\lambda_H; \varepsilon) = 0$, $\frac{\partial}{\partial \lambda} \alpha(\lambda_H; \varepsilon) \neq 0$, and

$$\lim_{\varepsilon \to 0} \beta(\lambda_H; \varepsilon) = \infty \text{ on the slow time scale } \tau, \text{ and}$$

$$\lim_{\varepsilon \to 0} \beta(\lambda_H; \varepsilon) = 0 \quad \text{on the fast time scale } t.$$
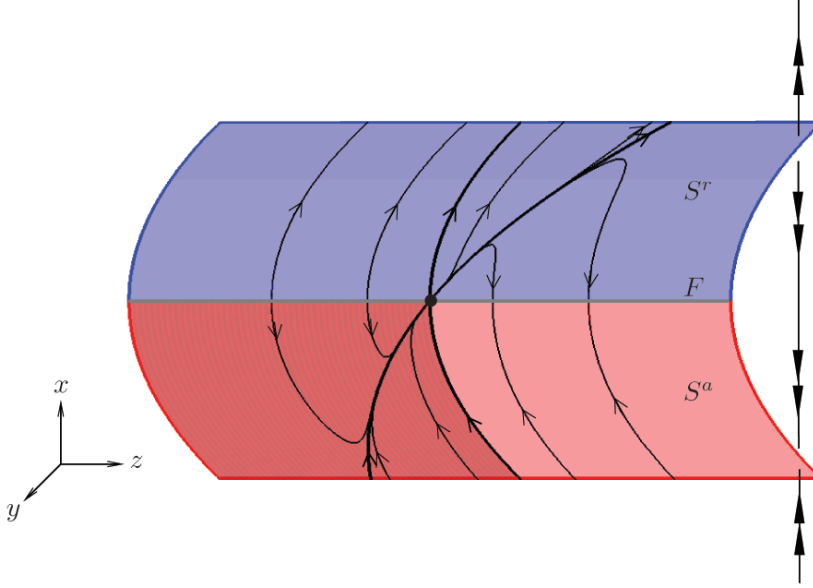
**Fig. 4** *The critical manifold $S$ with attracting sheet $S^a$ (red) and repelling sheet $S^r$ (blue) that meet at a fold curve $F$ (gray). The fast flow transverse to $S$ is indicated by double (large) arrows and the slow flow on $S$ near a folded node by single (small) arrows; see also Figure 5(b). The darker shaded region of $S^a$ is the funnel, consisting of all points that pass through the folded node.*

### 2.4. Folded Singularities in Systems with One Fast and Two Slow Variables.
A canard explosion for a planar system happens in an exponentially small parameter interval. However, as soon as there is more than one slow variable, canard orbits can exist for $O(1)$ ranges of a parameter. To illustrate this, we consider (2.1) for the special case $m = 1$ and $n = 2$ and write it as

$$(2.14) \qquad \begin{cases} \varepsilon\,\dot{x} = & f(x, y, z, \lambda, \varepsilon), \\ \dot{y} = g_1(x, y, z, \lambda, \varepsilon), \\ \dot{z} = g_2(x, y, z, \lambda, \varepsilon). \end{cases}$$

We assume that the critical manifold $S = \{f = 0\}$ of (2.14) has an attracting sheet $S^a$ and a repelling sheet $S^r$ that meet at a fold curve $F$, as is shown in Figure 4. We also assume that the fold points $p_* \in F$ on $S$ are generic in the sense of singularity theory, that is,

$$f(p_*, \lambda, 0) = 0, \qquad \frac{\partial f}{\partial x}(p_*, \lambda, 0) = 0,$$

$$\frac{\partial^2 f}{\partial x^2}(p_*, \lambda, 0) \neq 0, \qquad D_{(y,z)}f(p_*, \lambda, 0) \text{ has full rank one.}$$

The slow flow is not defined on the fold curve before desingularization. At most fold points, trajectories approach or depart from both the attracting and repelling sheets of $S$. In generic systems, there may be isolated points, called *folded singularities*, where the trajectories of the slow flow switch from incoming to outgoing. Folded singularities are equilibrium points of the desingularized slow flow. As described

above, the desingularized slow flow can be expressed as

(2.15)
$$\begin{cases} \dot{x} = \left(\frac{\partial}{\partial y}f\right) g_1 + \left(\frac{\partial}{\partial z}f\right) g_2, \\ \dot{y} = \qquad\quad - \left(\frac{\partial}{\partial x}f\right) g_1, \\ \dot{z} = \qquad\quad - \left(\frac{\partial}{\partial x}f\right) g_2, \end{cases}$$

restricted to $S$. A fold point $p_* \in F$ is a folded singularity if

$$g_1(p_*, \lambda, 0) \frac{\partial f}{\partial y}(p_*, \lambda, 0) + g_2(p_*, \lambda, 0) \frac{\partial f}{\partial z}(p_*, \lambda, 0) = 0.$$

Figure 4 shows an example of the slow flow on $S$ and the thick dot on $F$ is the folded singularity at which $F$ changes from attracting to repelling (with respect to the slow flow).

There are different possibilities for the stability of $p_*$ in (2.15). Let $\sigma_1$ and $\sigma_2$ denote the eigenvalues of the Jacobian matrix of (2.15) restricted to $S$ and evaluated at a folded singularity $p_*$. We call $p_*$ a

$$\begin{cases} \textit{folded saddle} & \text{if} \quad \sigma_1\,\sigma_2 < 0, \quad \sigma_{1,2} \in \mathbb{R}, \\ \textit{folded node} & \text{if} \quad \sigma_1\,\sigma_2 > 0, \quad \sigma_{1,2} \in \mathbb{R}, \\ \textit{folded focus} & \text{if} \quad \sigma_1\,\sigma_2 > 0, \quad \text{Im}(\sigma_{1,2}) \neq 0. \end{cases}$$

Figure 5 shows phase portraits of the (linearized) slow flow, in panels (a) and (b), and the associated desingularized slow flow, in panels (c) and (d), respectively. Panels (a) and (c) are for the case of a folded saddle and panels (b) and (d) of a folded node. Note that the phase portraits for the slow flow in Figure 5(a) and (b) are obtained by reversing the direction of the flow on $S^r$ where $\frac{\partial}{\partial x}f > 0$, that is, by reversing the arrows in the phase portraits of the desingularized slow flow in panels (c) and (d) in the half planes where $x > 0$. It is an important observation that the trajectories of the slow flow that lie along the eigendirections of the folded saddle or node connect the two sheets of the critical manifold through the folded singularity in finite (slow) time; such a trajectory is called a *singular canard*. We remark that there are no singular canards for the case of a folded focus, which is why it is not shown here. For the case of a folded node one generically has an inequality of the form $|\sigma_1| > |\sigma_2|$, and we write $|\sigma_s| > |\sigma_w|$, replacing the numeric labels with $s$ and $w$ to emphasize the strong and weak eigendirections. Notice further for the case of the folded node in Figure 5(b) that the strong singular canard $\tilde{\gamma}_s$ and the fold curve $F$ bound a full (shaded) sector of trajectories that cross from $S^a$ to $S^r$ by passing through the folded node. This sector and the corresponding region for the full system (2.14) are called the *funnel* of the folded node. The linearized system in Figure 5(b) should be compared with Figure 4, which shows a nonlinear slow flow near a folded node and, hence, also has a funnel consisting of a full sector of trajectories that pass through the folded singularity.

Singular canards act as candidates of maximal canards of the full system for $\varepsilon > 0$. This is described in the next theorem [19, 23, 31, 214, 237].

THEOREM 2.3 (canards in $\mathbb{R}^3$). *For the slow-fast system* (2.14) *with $\varepsilon > 0$ sufficiently small the following hold:*

(C1) *There are no maximal canards generated by a folded focus.*

(C2) *For a folded saddle the two singular canards $\tilde{\gamma}_{1,2}$ perturb to maximal canards $\gamma_{1,2}$.*

(C3.1) *For a folded node let $\mu := \sigma_w/\sigma_s < 1$. The singular canard $\tilde{\gamma}_s$ ("the strong canard") always perturbs to a maximal canard $\gamma_s$. If $\mu^{-1} \notin \mathbb{N}$, then the*
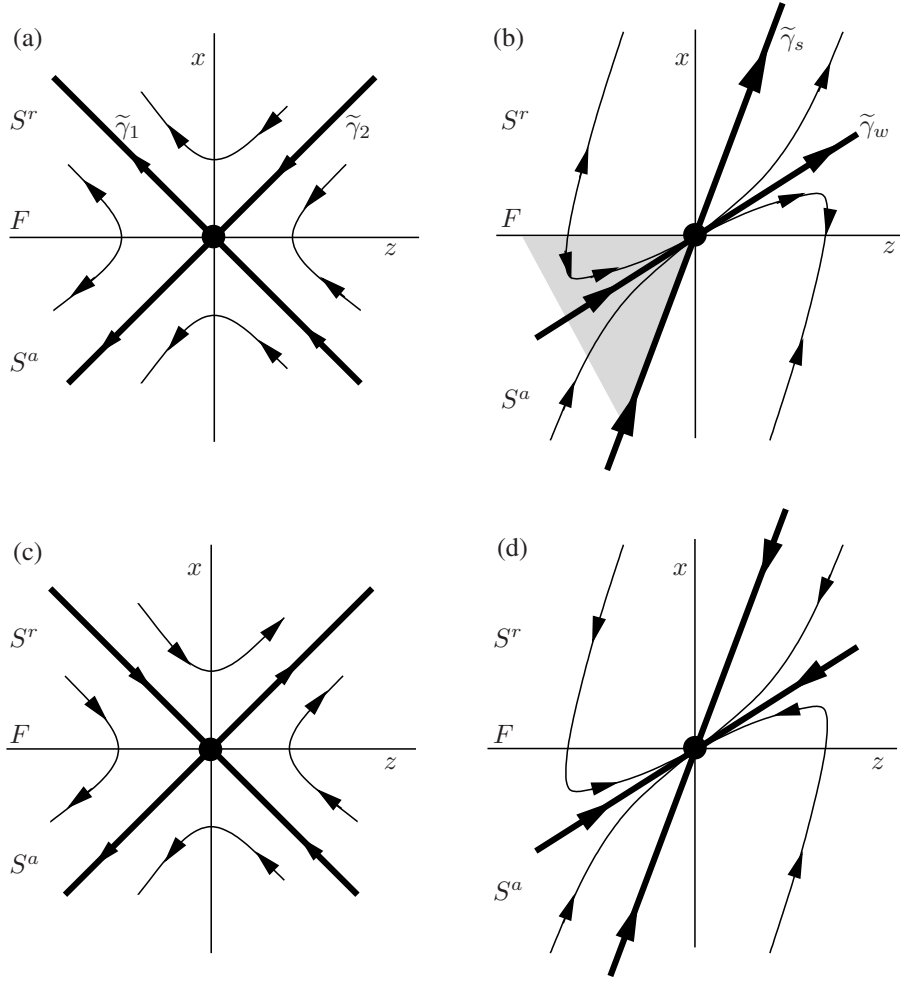
**Fig. 5**  *Phase portraits of the locally linearized slow flow near a folded saddle (a) and a folded node (b); the singular canards defined by the eigendirections are shown as thick lines. The corresponding desingularized slow flow is shown in panels (c) and (d), respectively.*

singular canard $\tilde{\gamma}_w$ *("the weak canard") also perturbs to a maximal canard $\gamma_w$. We call $\gamma_s$ and $\gamma_w$ primary canards.*

(C3.2)  *For a folded node suppose $k > 0$ is an integer such that $2k+1 < \mu^{-1} < 2k+3$ and $\mu^{-1} \neq 2(k+1)$. Then, in addition to $\gamma_{s,w}$, there are $k$ other maximal canards, which we call secondary canards.*

(C3.3)  *The primary weak canard of a folded node undergoes a transcritical bifurcation for odd $\mu^{-1} \in \mathbb{N}$ and a pitchfork bifurcation for even $\mu^{-1} \in \mathbb{N}$.*

The proof of this theorem is based upon analysis of a canonical (normal) form of a slow-fast system near a folded singularity. Recall that a maximal canard corresponds to a (transverse) intersection of the slow manifolds $S_\varepsilon^a$ and $S_\varepsilon^r$ near a folded singularity. After a rescaling of coordinates (a "blow-up"), the canonical system becomes a regular perturbation problem and the variational equation along the "blown-up" singular canards ($\varepsilon = 0$ problem) becomes a classical *Weber equation* that also arises

in mathematical physics [176]. Properties of the Weber equation imply a transverse intersection of $S_\varepsilon^a$ and $S_\varepsilon^r$ for $\mu^{-1} \notin \mathbb{N}$ and, hence, existence of maximal canards (parts (C2)–(C3.1)) for sufficiently small perturbations $0 < \varepsilon \ll 1$. The proof of parts (C3.2)–(C3.3) is more involved and is based upon an extension of *Melnikov theory* [236] to show the bifurcation of secondary canards from the primary weak canard for $\mu^{-1} \in \mathbb{N}$.

**3. Slow-Fast Mechanisms for MMOs.** In this section we present key theoretical results of how MMOs arise in slow-fast systems with SAOs occurring in a localized region of the phase space. More specifically, we discuss four local mechanisms that give rise to such SAOs:

- passage near a folded node, discussed in section 3.1;
- singular Hopf bifurcation, discussed in section 3.2;
- three-time-scale problems with a singular Hopf bifurcation, discussed in section 3.3;
- the tourbillon mechanism of a dynamic Hopf bifurcation, discussed in section 3.4.

In sections 3.1–3.4 our major focus is on how the local mechanism under consideration gives rise to SAOs. To this end, we introduce relevant normal forms and model systems and provide precise statements on the nature of the resulting SAOs. It is in the nature of the subject that some of this material is quite technical. However, this analysis allows us to estimate quantities that can be measured in examples of MMOs produced from both numerical simulations and experimental data. Specifically, we consider the number of SAOs and the changes in their amplitudes from cycle to cycle. These characteristics of each local mechanism are illustrated and discussed in terms of underlying geometric concepts, with pointers to the case studies in sections 4–7. Furthermore, we show in sections 3.1–3.4 how the respective local mechanism results in MMOs in the presence of a *global return mechanism* that takes the trajectory back to the region with SAOs. Such global return mechanisms are found in models; see section 3.2 and the case studies in sections 4–5 for examples with an S-shaped slow manifold. We also consider the geometry of nearby slow manifolds that are associated with the approach to and departure from the SAO regions.

**3.1. MMOs Due to a Folded Node.** Folded nodes are only defined for the singular limit (2.4) of system (2.1) on the slow time scale. However, they are directly relevant to MMOs because, for $\varepsilon > 0$ small enough, trajectories of (2.1) that flow through a region where the reduced system has a folded node undergo small oscillations. Benoît [19, 20] first recognized these oscillations. Wechselberger and collaborators [31, 214, 237] gave a detailed analysis of folded nodes, while Guckenheimer and Haiduc [88] and Guckenheimer [86] computed intersections of slow manifolds near a folded node and flow maps along trajectories passing through these regions. From Theorem 2.3 we know that the eigenvalue ratio $0 < \mu < 1$ at the folded node is a crucial quantity that determines the dynamics in a neighborhood of the folded node. In particular, $\mu$ controls the maximal number of oscillations. The studies mentioned above use normal forms to describe the dynamics of oscillations near a folded node. Two equivalent versions of these normal forms are

$$(3.1) \qquad \begin{cases} \varepsilon\,\dot{x} = y - x^2, \\ \quad\dot{y} = z - x, \\ \quad\dot{z} = -\nu \end{cases}$$

and

(3.2)
$$\begin{cases} \varepsilon \dot{x} = y - x^2, \\ \dot{y} = -(\mu + 1)x - z, \\ \dot{z} = \frac{1}{2}\mu. \end{cases}$$

Note that $\mu$ is the eigenvalue ratio of system (3.2) and that $\nu \neq 0$ and $\mu \neq 0$ imply that no equilibria exist in (3.1) and (3.2). If we replace $(x, y, z)$ in system (3.1) by $(u, v, w)$ and call the time variable $\tau_1$, then we obtain system (3.2) via the coordinate change

$$x = (1 + \mu)^{1/2}\, u, \quad y = (1 + \mu)\, v, \quad z = -(1 + \mu)^{3/2}\, w$$

and the rescaling of time $\tau = \tau_1 / \sqrt{1 + \mu}$, which gives

(3.3)
$$\nu = \frac{\mu}{2(1 + \mu)^2} \quad \text{or} \quad \mu = \frac{-1 + \sqrt{1 - 8\nu}}{-1 - \sqrt{1 - 8\nu}}.$$

Therefore, in system (3.1) the number of secondary canards changes with the parameter $\nu$: when $\nu$ is small, $\mu \approx 2\nu$. Applying the "standard" scaling [214] $x = \varepsilon^{1/2}\, \bar{x}$, $y = \varepsilon\, \bar{y}$, $z = \varepsilon^{1/2}\, \bar{z}$, and $t = \varepsilon^{1/2}\, \bar{t}$ to system (3.1), and dropping the bars for notational convenience, yields

(3.4)
$$\begin{cases} \dot{x} = y - x^2, \\ \dot{y} = z - x, \\ \dot{z} = -\nu. \end{cases}$$

Hence, the phase portraits of system (3.1) for different values of $\varepsilon$ are topologically equivalent via linear maps. The normal form (3.4) describes the dynamics in the neighborhood of a folded node, which is at the origin here, with eigenvalue ratio $\mu$ as given in (3.3). Trajectories that come from $y = \infty$ with $x > 0$ and pass through the folded-node region make a number of oscillations in the process, before going off to $y = \infty$ with $x < 0$. There are no returns to the folded-node region in this system.

Let us first focus on the number of small oscillations. If $2k + 1 < \mu^{-1} < 2k + 3$ for some $k \in \mathbb{N}$ and $\mu^{-1} \neq 2(k + 1)$, then the primary strong canard $\gamma_s$ twists once and the $i$th secondary canard $\xi_i$, $1 \leq i \leq k$, twists $2i + 1$ times around the primary weak canard $\gamma_w$ in an $O(1)$ neighborhood of the folded-node singularity in system (3.4), which corresponds to an $O(\sqrt{\varepsilon})$ neighborhood in systems (3.1) and (3.2) [214, 237]. (A twist corresponds to a half rotation.) We illustrate this in Figure 6 for system (3.4) with $\nu = 0.025$. Note that $\nu = 0.025$ corresponds to $\mu \approx 0.0557$. Hence, $2k + 1 < \mu^{-1} \approx 17.953 < 2k + 3$ for $k = 8$, so Theorem 2.3 states that there exist eight secondary canards $\xi_i$, $1 \leq i \leq 8$, along with the strong and weak canards $\gamma_{s/w}$. Figure 6 shows the attracting slow manifold $S_\varepsilon^a$ and the repelling slow manifold $S_\varepsilon^r$ of (3.4) in a three-dimensional region bounded by the planes $\{z = \pm \alpha\}$, denoted $\Sigma_\alpha$ and $\Sigma_{-\alpha}$, with $\alpha = 0.14$; see section 8 for details on how these computations were done. Even though the rescaled normal form (3.4) no longer depends on $\varepsilon$, we still indicate the $\varepsilon$-dependence of the slow manifolds to distinguish them from the attracting and repelling sheets of the critical manifold; furthermore, $S_\varepsilon^a$ and $S_\varepsilon^r$ can be thought of as the slow manifolds of (3.1) or (3.2). Both manifolds are extensions of Fenichel manifolds and illustrate how the slow manifolds intersect near the fold curve of the critical manifold; the fold curve is the $z$-axis. Due to the symmetry

$$(x, y, z, t) \mapsto (-x, y, -z, -t)$$

of the normal form (3.4), the two slow manifolds $S_\varepsilon^a$ and $S_\varepsilon^r$ are each other's image under rotation by $\pi$ about the $y$-axis. The intersection curves in Figure 6(a) are the
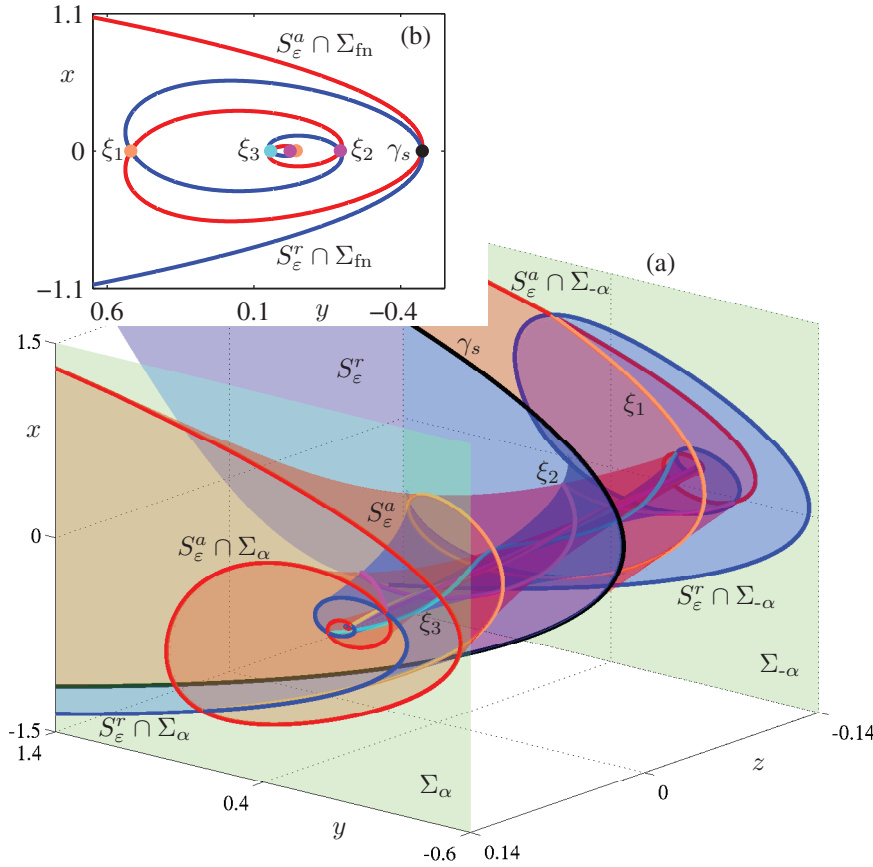
**Fig. 6** *Invariant slow manifolds of (3.4) with $\nu = 0.025$ in a neighborhood of the folded node. Both the attracting slow manifold $S^a_\varepsilon$ (red) and the repelling slow manifold $S^r_\varepsilon$ (blue) are extensions of Fenichel manifolds. The primary strong canard $\gamma_s$ (black curve) and three secondary canards $\xi_1$ (orange), $\xi_2$ (magenta), and $\xi_3$ (cyan) are the first four intersection curves of $S^a_\varepsilon$ and $S^r_\varepsilon$; the inset shows how these objects intersect a cross-section orthogonal to the fold curve $\{x = 0, y = 0\}$.*

canard orbits; labeled are the primary strong canard $\gamma_s$ (black) and the first three secondary canards $\xi_1$ (orange), $\xi_2$ (magenta), and $\xi_3$ (cyan). The inset panel (b) shows the intersection curves of $S^a_\varepsilon$ and $S^r_\varepsilon$ with the plane $\Sigma_{\mathrm{fn}} := \{z = 0\}$ that contains the folded node at the origin. Canard orbits are identified in $\Sigma_{\mathrm{fn}}$ as intersection points; only $\gamma_s$ and $\xi_1$–$\xi_3$ are labeled, but notice that there are further canards (including the weak canard $\gamma_w$) very close together in the center of the figure.

A trajectory entering the fold region becomes trapped in a region bounded by strips of $S^a_\varepsilon$ and $S^r_\varepsilon$ and two of their intersection curves. The intersection curves are maximal canards, and the trajectory is forced to follow the oscillations of these two bounding canard orbits. In order to illustrate how many canards there are and precisely how many oscillations they make, we show in Figure 7(a) the flow map of (3.4) with $\nu = 0.025$. Due to the strong contraction along $S^a_\varepsilon$, the flow map through the fold region is strongly contracting in one direction for trajectories that
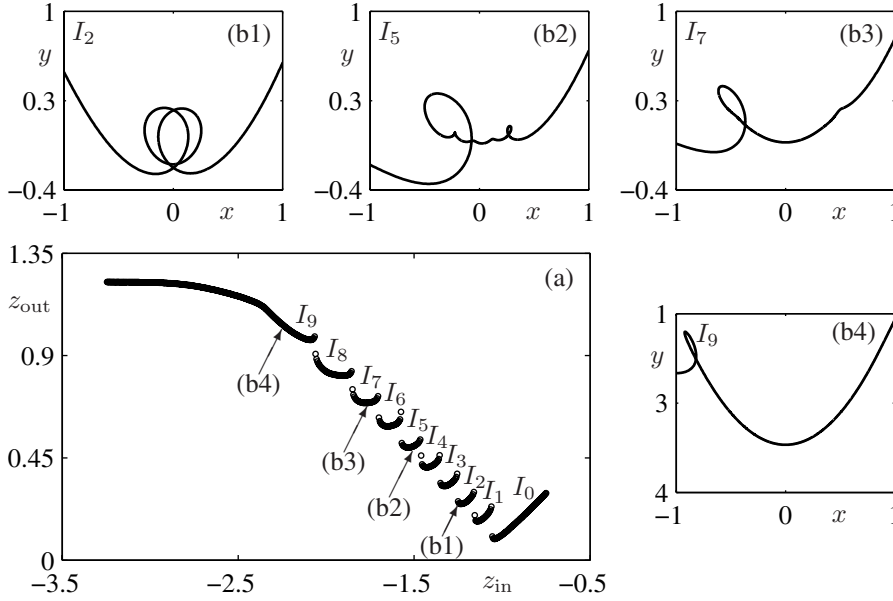
**Fig. 7**  *Numerical study of the number of rotational sectors for system (3.4) with $\nu = 0.025$. Panel (a) illustrates the flow map through the folded node by plotting the $z$-coordinates $z_{\mathrm{out}}$ of the first return to a cross-section $x = -10$ of 500 trajectories with equally spaced initial values $(x, y, z) = (20, 400, z_{\mathrm{in}})$, where $-3.25 \leq z_{\mathrm{in}} \leq -0.75$. Panels (b1)–(b4) show four trajectories projected onto the $(x, y)$-plane that correspond to the points labeled in panel (c), where $z_{\mathrm{in}} = -1.25$ in panel (b1), $z_{\mathrm{in}} = -1.5$ in panel (b2), $z_{\mathrm{in}} = -1.75$ in panel (b3), and $z_{\mathrm{in}} = -2.25$ in panel (b4).*

do not extend along $S_\varepsilon^r$. Hence, the flow map will be almost one-dimensional and can be approximated by following trajectories starting on the critical manifold far away from the fold curve. The flow map shown in Figure 7(a) was obtained by integrating 500 equally spaced initial values on the line segment $\{x = 20, \; y = x^2 = 400, \; -3.25 \leq z \leq -0.75\}$ until they reach the plane $x = -10$; plotted are the $z$-coordinates of the final values versus the initial values. One can see ten segments in this flow map that are separated by discontinuities. These discontinuities mark sectors on the line segment $\{x = 20, \; y = x^2 = 400, \; -3.25 \leq z \leq -0.75\}$ that correspond to an increasing number of SAOs; in fact, each segment corresponds to a two-dimensional sector $I_i$, $0 \leq i \leq 9$, on the attracting sheet $S_\varepsilon^a$ of the slow manifold. The outer sector $I_0$ on the right in Figure 7(a) is bounded on the left by the primary strong canard $\gamma_s$; sector $I_1$ is bounded by $\gamma_s$ and the first maximal secondary canard $\xi_1$; sectors $I_i$, $i = 2, \ldots, 8$, are bounded by maximal secondary canard orbits $\xi_{i-1}$ and $\xi_i$; and the last (left outer) sector $I_9$ is bounded on the right by $\xi_8$. On one side of the primary strong canard $\gamma_s$ and each maximal secondary canard $\xi_i$, $1 \leq i \leq 8$, trajectories follow the repelling slow manifold $S_\varepsilon^r$ and then jump with decreasing values of $x$. On the other side of $\gamma_s$ and $\xi_i$, trajectories jump back to the attracting slow manifold and make one more oscillation through the folded-node region before flowing toward $y = \infty$. The four panels (b1)–(b4) in Figure 7 show portions of four trajectories projected onto the $(x, y)$-plane; their initial values are $(x, y, z) = (20, 400, z_{\mathrm{in}})$ with $z_{\mathrm{in}}$ as marked in panel (a), that is, $z_{\mathrm{in}} = -1.25$, $z_{\mathrm{in}} = -1.5$, $z_{\mathrm{in}} = -1.75$, and $z_{\mathrm{in}} = -2.25$ for (b1)–(b4), respectively. The trajectory in panel (b1) was chosen from the sector $I_2$, bounded by $\xi_1$ and $\xi_2$;

this trajectory makes two oscillations. The trajectory in panel (b2) comes from $I_5$ and, indeed, it makes five oscillations. The other two trajectories, in panels (b3) and (b4), make seven and nine oscillations, respectively, but some of these oscillations are too small to be visible.

The actual widths of the rotational sectors in Figure 7 are very similar due to the $\varepsilon$-dependent rescaling used to obtain (3.4). When the equations depend on $\varepsilon$ as in (3.1) and (3.2), however, the widths of the sectors depend on $\varepsilon$. In fact, all sectors are very small except for the sector corresponding to maximal rotation, which is bounded by $\xi_k$ and the primary weak canard. For an asymptotic analysis of the widths of the rotational sectors that organize the oscillations, system (3.2) is more convenient, because the eigenvalues of the desingularized slow flow are $-\mu$ and $-1$. Brøns, Krupa, and Wechselberger [31] found the following result.

THEOREM 3.1 (widths of rotational sectors). *Consider system* (2.14) *and assume it has a folded-node singularity. At an $O(1)$ distance from the fold curve, all secondary canards are in an $O(\varepsilon^{(1-\mu)/2})$ neighborhood of the primary strong canard. Hence, the widths of the rotational sectors $I_i$, $1 \le i \le k$, is $O(\varepsilon^{(1-\mu)/2})$ and the width of sector $I_{k+1}$ is $O(1)$.*

Note that, as $\mu \to 0$ (the folded saddle-node limit), the number of rotational sectors increases indefinitely and the upper bounds on their widths decrease to $O(\varepsilon^{1/2})$.

**3.1.1. Folded Node with a Global Return Mechanism.** A global return mechanism may reinject trajectories to the folded-node funnel to create an MMO. In this situation, we create a candidate trajectory as is illustrated in Figure 8. Starting from the folded node we follow the fast flow until it returns to the funnel and then flows back to the folded node. Let us denote by $\delta$ the distance from the singular strong canard $\tilde{\gamma}_s$, measured on a cross-section at a distance $O(1)$ away from the fold, at which the candidate trajectory returns to the funnel. Provided that certain technical conditions are satisfied, one can show that this candidate gives rise to an MMO periodic orbit with signature $1^s$, where the number $s$ of SAOs is as predicted by Theorem 3.1; this theorem also implies that the candidate is most likely to pass through the sector $I_{k+1}$ of maximal rotation, where $k$ is determined by the eigenvalue ratio $\mu$. Overall, we have the following result.

THEOREM 3.2 (generic $1^{k+1}$ MMOs [31]). *Consider system* (2.14) *with the following assumptions:*

  (A0)  *Assume that $0 < \epsilon \ll 1$ is sufficiently small, $\varepsilon^{1/2} \ll \mu$, and $k \in \mathbb{N}$ is such that $2k + 1 < \mu^{-1} < 2k + 3$.*
  (A1)  *The critical manifold $S$ is (locally) a folded surface.*
  (A2)  *The corresponding reduced problem possesses a folded-node singularity.*
  (A3)  *There exists a candidate periodic orbit (as constructed in Figure 8), which consists of fast fibers of the layer problem, a global return segment, and a segment on $S^a$ within the funnel that starts at distance $\delta$ from $\tilde{\gamma}_s$ (as measured at a distance $O(1)$ away from the fold $F$).*
  (A4)  *An appropriate transversality hypothesis is satisfied.*
*Then there exists a stable MMO with signature $1^{k+1}$.*

The transversality hypothesis of (A4) is cumbersome to formulate in a general setting. In the context of an S-shaped manifold, it concerns the projection of the two fold curves onto the opposite sheets of the attracting slow manifold and the flow along these sheets; see [31].

Theorem 3.2 requires not only sufficiently small $0 < \varepsilon \ll 1$, but also $\mu \gg \varepsilon^{1/2}$ (while $0 < \mu < 1$). However, $\varepsilon$ is usually of the order $O(10^{-2})$ in applications, so that
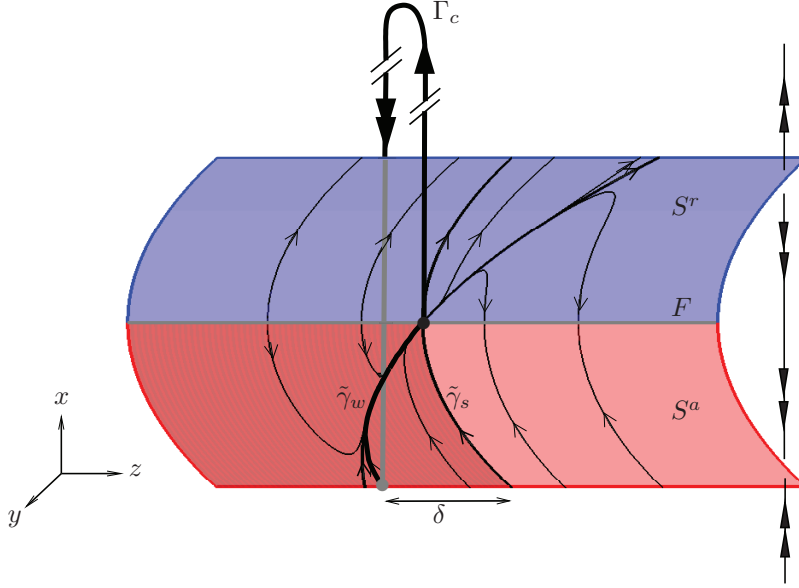
**Fig. 8**  *Schematic diagram of the candidate periodic orbit $\Gamma_c$ that gives rise to MMOs with SAOs produced by a folded-node singularity. The candidate $\Gamma_c$ approaches the folded node along the attracting sheet $S^a$ (red) of the critical manifold (red) in the sector of maximal rotation associated with the weak singular canard $\tilde{\gamma}_w$. The distance to the strong singular canard $\tilde{\gamma}_s$ is labeled $\delta$. When the trajectory reaches the folded node (black dot) it jumps along a layer and proceeds to make a global return.*

$\mu$ must be close to 1 in order for the theorem to apply. Therefore, such maximal MMO signatures are seldom seen in applications. Furthermore, the SAOs for an MMO with signature $1^{k+1}$ tend to be too small to be readily visible.

Figure 7 illustrates that the amplitudes of the SAOs are much larger for trajectories that approach the folded node close to the strong canard and lie in one of the sectors $I_i$ with $i \leq k$ rather than $I_{k+1}$. We know from Theorem 3.1 that the maximal width of a sector $I_i$ with $i \leq k$ is bounded from above by $O(\varepsilon^{(1-\mu)/2})$ with $\mu < 1/3$. When $\delta$ is $O(\varepsilon^{(1-\mu)/2})$ one may actually find stable MMOs with $i \leq k$ SAOs, which is the following result [31].

THEOREM 3.3 (stable MMOs with signature $1^i$).  *Suppose system* (2.14) *satisfies assumptions* (A0)–(A3) *of Theorem* 3.2 *and, the following additional assumption:*

(A5)  *For $\delta = 0$, the global return point is on the singular strong canard $\tilde{\gamma}_s$ and as $\delta$ passes through zero the return point crosses $\tilde{\gamma}_s$ with nonzero speed.*

*Suppose now that $\delta = O(\varepsilon^{(1-\mu)/2}) > 0$. Then, for sufficiently small $0 < \varepsilon \ll 1$ and $k \in \mathbb{N}$ such that $2k + 1 < \mu^{-1} < 2k + 3$, the following holds. For each $i$, $1 \leq i \leq k$, there exist subsectors $\tilde{I}_i \subset I_i$ with corresponding distance intervals $(\delta_i^-, \delta_i^+)$ of widths $O(\varepsilon^{(1-\mu)/2})$, which have the property that if $\delta \in (\delta_i^-, \delta_i^+)$, then there exists a stable MMO with signature $1^i$.*

Theorem 3.3 says that we should observe a succession of stable $1^i$ MMOs with increasingly more SAOs as $\delta$ increases (assuming that $\mu$ remains fixed in such a parameter variation). In the transition from a $1^i$ to a $1^{i+1}$ MMO signature, that is, in the regions in between intervals $(\delta_i^-, \delta_i^+)$ and $(\delta_{i+1}^-, \delta_{i+1}^+)$, we expect to find

more complicated signatures, which are usually a mix of $1^i$ and $1^{i+1}$. Geometrically, different stable MMOs are selected as one moves the flow map in Figure 7(a) up or down; since the rotational sector $I_{k+1}$ for general $\varepsilon$-dependent systems has much larger width than the other sectors, one should expect that the transitions through $I_i$ with $i \leq k$ happen rather quickly during a parameter-induced variation of $\delta$.

If $\mu = O(\varepsilon^{1/2})$, that is, assumption (A0) does not hold, then we may still expect stable MMO signatures of type $1^{k+1}$, as soon as the global returns falls inside the funnel region and $\delta = O(1)$ [144]; note that $k = O(1/\varepsilon^{1/2})$ and the amplitudes of the SAOs for such an MMO will again be tiny. If $\mu = O(\varepsilon^{1/2})$ and $\delta = O(\varepsilon^{1/2})$ as well, the mixed MMO signatures with larger-amplitude SAOs are more likely to occur. For example, Figure 20 in section 4 displays an MMO of type $1^2 1^3$ in the Koper model. Here, global returns come very close to the secondary maximal canard $\xi_2$, first slightly to the left (hence, into the rotational sector $I_2$ with two SAOs) and then slightly to the right (hence, into the rotational sector $I_3$ with three SAOs), creating this MMO signature.

The theory described so far does not capture all of the possible dynamics near a folded node. If higher-order terms are included in the normal forms (3.1)–(3.2), then equilibria may appear in an $O(\varepsilon^{1/2})$ neighborhood of the folded node as soon as $\mu = O(\varepsilon^{1/2})$ or smaller. This observation motivates our study of the singular Hopf bifurcation in three dimensions.

**3.2. MMOs Due to a Singular Hopf Bifurcation.** Equilibria of a slow-fast system (2.1) always satisfy $f(x, y, \lambda, \varepsilon) = 0$; generically, they are located in regions where the associated critical manifold $S$ is normally hyperbolic. However, in generic one-parameter families of slow-fast systems, the equilibrium may cross a fold of $S$. When this happens the folded singularity at which the equilibrium crosses the fold curve is an actual equilibrium of the slow-fast system. In generic vector fields with two slow variables the folded singularity thus created is a folded saddle-node, which exists exactly at the specific parameter value at which the equilibrium crosses the fold curve; one speaks of a *folded saddle-node of type II* [162]. This is distinguished from the *folded saddle-node of type I* [214, 144], which refers to a saddle-node bifurcation of the reduced flow only, meaning that it does *not* involve a true equilibrium of the full system. This distinction stems from the fact that—as we have seen with the examples of the folded saddle and the folded node—a singularity of the reduced system need not be the projection of an equilibrium of the full slow-fast system. However, a folded saddle-node of type II is an actual equilibrium of the full system. Importantly, this implies that, when $\varepsilon > 0$, the system has a singular Hopf bifurcation which occurs generically at a distance $O(\varepsilon)$ in parameter space from the folded saddle-node bifurcation of type II [87].

In order to obtain a normal form for the singular Hopf bifurcation, we follow [87] and add higher-order terms to the normal form (3.1) of the folded node, to obtain

$$(3.5) \qquad \begin{cases} \varepsilon\,\dot{x} = y - x^2, \\ \quad\dot{y} = z - x, \\ \quad\dot{z} = -\nu - a\,x - b\,y - c\,z. \end{cases}$$

As with (3.1), we apply the standard scaling [214] $x = \varepsilon^{1/2}\,\bar{x}$, $y = \varepsilon\,\bar{y}$, $z = \varepsilon^{1/2}\,\bar{z}$, and $t = \varepsilon^{1/2}\,\bar{t}$; system (3.5) then becomes

$$(3.6) \qquad \begin{cases} \bar{x}' = \bar{y} - \bar{x}^2, \\ \bar{y}' = \bar{z} - \bar{x}, \\ \bar{z}' = -\nu - \varepsilon^{1/2}\,a\,\bar{x} - \varepsilon\,b\,\bar{y} - \varepsilon^{1/2}\,c\,\bar{z}. \end{cases}$$

This scaled vector field provides an $O(\varepsilon^{1/2})$ zoom of the neighborhood of the folded singularity where SAOs are expected to occur. The scaling removes $\varepsilon$ from the first equations, while the coefficients $a$, $b$, and $c$ of the third equation become $\varepsilon$-dependent; $\nu$ remains fixed. Note that the coefficient of $\bar{y}$ tends to 0 faster than those of $\bar{x}, \bar{z}$ as $\varepsilon \to 0$. This feature makes the definition of normal forms for slow-fast systems somewhat problematic: scalings of the state-space variables and the singular perturbation parameter $\varepsilon$ interact with each other. These $\varepsilon$-dependent scalings play an important role in "blow-up" analysis of fold points and folded singularities.

In contrast to the normal form (3.1) of a folded node, system (3.6) possesses equilibria for all values of $\nu$. If $\nu = O(1)$, then these equilibria are far from the origin, with coordinates that are $O(\varepsilon^{-1/2})$ or larger. Since we want to study the dynamics near a folded singularity, the $\varepsilon$-dependent terms in (3.6) play little role in this parameter regime and the system can be regarded as an inconsequential perturbation of the folded-node normal form (3.4); hence, if $\nu = O(1)$, then Theorems 3.2 and 3.3 apply. On the other hand, if $\nu = O(\varepsilon^{1/2})$ or smaller, then one equilibrium lies within an $O(1)$-size domain of the phase space. This equilibrium is determined by the coefficients $a$ and $c$ (to leading order) and plays an important role in the local dynamics near a folded singularity [87, 144]. In particular, the equilibrium undergoes a singular Hopf bifurcation for $\nu = O(\varepsilon)$ [87]. Thus, for parameter values $\nu = O(\varepsilon^{1/2})$ or smaller, the higher-order terms in the third equation of (3.6) are crucial.

So what is the most appropriate normal form of a system that undergoes a singular Hopf bifurcation? Several groups have derived system (3.5), but drop the term $by$ because it has higher order in $\varepsilon$ after the scaling. However, this term appears in the formula for the lowest-order term in $\varepsilon$ of the first Lyapunov coefficient of the Hopf bifurcation of (3.5) and, hence, must be retained if we hope to determine a complete unfolding of the singular Hopf bifurcation [87].

The MMOs that occur close to the singular Hopf bifurcation have a somewhat different character than those generated via the folded-node mechanism. Guckenheimer and Willms [95] observed that a subcritical (ordinary) Hopf bifurcation may result in large regions of the parameter space being funneled into a small neighborhood of a saddle equilibrium with unstable complex eigenvalues. After trajectories come close to the equilibrium, SAOs grow in magnitude as the trajectory spirals away from the equilibrium. Similar MMOs may pass near a singular Hopf bifurcation. Then the equilibrium is a saddle-focus and trajectories on the attracting Fenichel manifold are funneled into a region close to the one-dimensional stable manifold of the equilibrium. SAOs occur as the trajectory spirals away from the equilibrium. We review here our (still incomplete) understanding of singular Hopf bifurcations and the MMOs passing nearby.

The normal form (3.5) does not yield MMOs because there is no global return mechanism; trajectories that leave the vicinity of the equilibrium point and the fold curve flow to infinity in finite time. This property can be changed by adding a cubic term to the normal form that makes the critical manifold S-shaped, similar to the Van der Pol equation:

(3.7)
$$\begin{cases} \varepsilon \, \dot{x} = y - x^2 - x^3, \\ \quad \dot{y} = z - x, \\ \quad \dot{z} = -\nu - a \, x - b \, y - c \, z. \end{cases}$$

This modification of the normal form for the singular Hopf bifurcation was derived previously as a "reduced" model for MMOs [123, 139]. System (3.7) introduces only
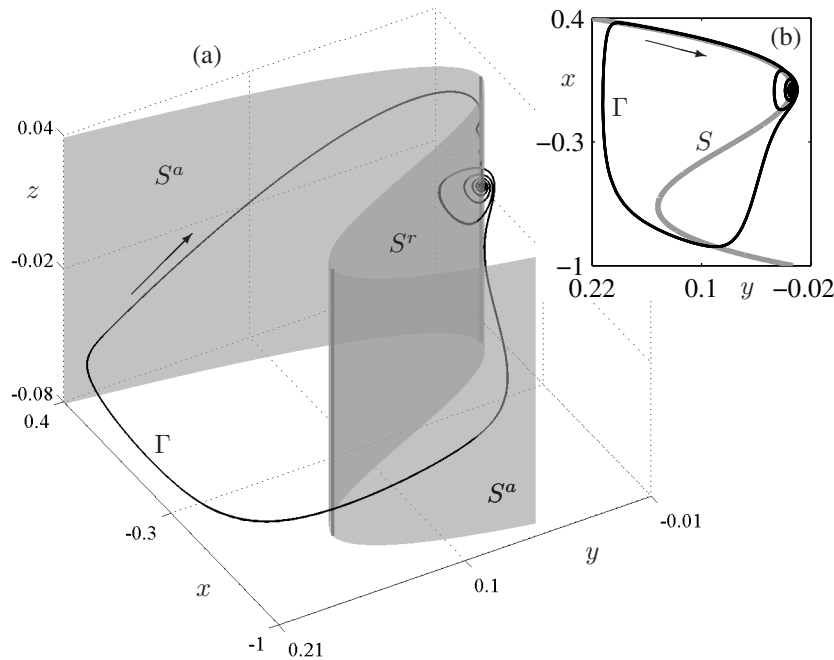
**Fig. 9**  *Phase portrait of an MMO periodic orbit $\Gamma$ (black curve) for system (3.7) with $(\nu, a, b, c, \varepsilon) = (0.0072168, -0.3872, -0.3251, 1.17, 0.01)$. The critical manifold $S$ (gray) is the S-shaped surface with folds at $x = 0$ and $x = -\frac{2}{3}$. The orbit $\Gamma$ is composed of two slow segments near the two attracting sheets of $S$ and two fast segments, with SAOs in the region near the equilibrium $p$ on the repelling sheet $S^r$ of $S$ just past the fold at $x = 0$. Panel (a) shows a three-dimensional view and panel (b) the projection onto the $(x, y)$-plane.*

a small perturbation near the origin, but the S-shaped critical manifold creates the possibility that trajectories leaving a neighborhood of the origin might return, as illustrated in Figure 9. Figure 9 shows an example of the overall structure of MMOs in system (3.7) with small $\nu$, namely, for $(\nu, a, b, c, \varepsilon) = (0.0072168, -0.3872, -0.3251, 1.17, 0.01)$; note that $\nu = O(\varepsilon)$. The S-shaped critical manifold $S$ is the gray surface in Figure 9(a); a top view is shown in panel (b). The manifold $S$ has two fold curves, one at $x = 0$ and one at $x = -\frac{2}{3}$, that decompose $S$ into one repelling and two attracting sheets. For our choice of parameters there exists a saddle-focus equilibrium $p$ on the repelling sheet that is close to the origin (which is the folded-node singularity). The equilibrium $p$ has a pair of unstable complex conjugate eigenvalues. A stable MMO periodic orbit $\Gamma$, shown as the black curve in Figure 9, interacts with $p$ as follows. Starting just past the fold at $x = 0$, that is, in the region near the origin with $x < 0$, the orbit $\Gamma$ spirals away from $p$ along its two-dimensional unstable manifold and repeatedly intersects the repelling sheet $S^r$ of $S$. As soon as $\Gamma$ intersects the repelling slow manifold (not shown), it jumps to the attracting sheet of $S$ with $x < -\frac{2}{3}$. The orbit $\Gamma$ then follows this sheet to the fold at $x = -\frac{2}{3}$, after which it jumps to the attracting sheet of $S$ with $x > 0$. Then $\Gamma$ returns to the neighborhood of $p$ and the periodic motion repeats.

The MMO periodic orbit $\Gamma$ displayed in Figure 9 is only one of many types of complex dynamics present in system (3.7). One aspect of the complex dynamics
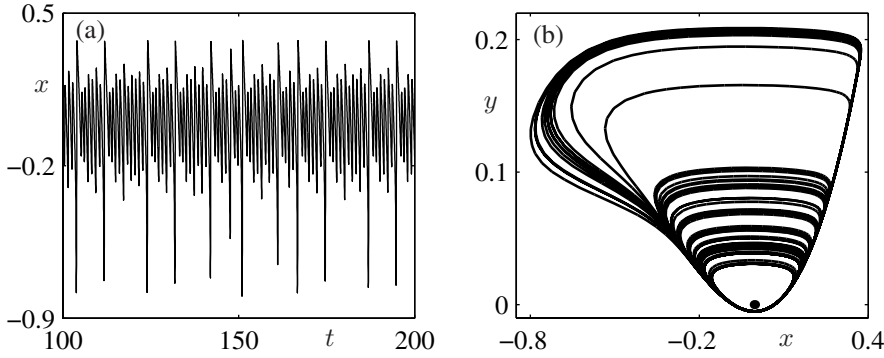
**Fig. 10**  *A chaotic MMO trajectory of system* (3.7) *with* $(\nu, a, b, c, \varepsilon) = (0.004564, -0.2317, 0.2053,$
$1.17, 0.01)$. *Panel* (a) *shows the time series of the $x$-coordinate of the trajectory from $t = 100$*
*to $t = 200$, and panel* (b) *the projection of the trajectory onto the $(x, y)$-plane.*

in system (3.7) is the fate of the periodic orbits created in the Hopf bifurcation.
There are parameter regimes for (3.7) with stable periodic orbits of small amplitude
created by a supercritical Hopf bifurcation. Subsequent bifurcations of these periodic
orbits may be period-doubling or torus bifurcations [87]. Period-doubling cascades
can give rise to small-amplitude chaotic invariant sets that may be associated with
chaotic MMOs. For example, Figure 10 plots a chaotic MMO trajectory for (3.7) with
$(\nu, a, b, c, \varepsilon) = (0.004564, -0.2317, 0.2053, 1.17, 0.01)$ that arises from such a period-
doubling cascade of the periodic orbit emerging from the singular Hopf bifurcation.
It appears that it is chaotic because of the nonperiodicity of its time series, shown
for the $x$-coordinate in Figure 10(a). A two-dimensional projection onto the $(x, y)$-
plane is shown in panel (b). Note that this trajectory does not come close to either
the equilibrium point $p$ or the folded singularity at the origin. As $\nu$ decreases from
the value used in Figure 10 (where $\nu$ is already of order $O(\varepsilon)$), the large-amplitude
epochs of the trajectories become less frequent and soon disappear, resulting in a
small-amplitude chaotic attractor. Section 4 discusses a rescaled subfamily of (3.7),
giving further examples of complex dynamics and some analysis of the organization
of MMOs associated with this system.

We would like to characterize the parameter regimes with MMOs for which the
SAOs are solely or partially due to spiraling along the unstable manifold $W^u(p)$ of a
saddle-focus $p$. Analysis of this issue appears to be significantly more complicated than
that for folded nodes and has barely begun. We offer a few insights into locating these
parameter regimes. First, we think of $\nu$ in the normal form (3.7) of the singular Hopf
bifurcation as the "primary" bifurcation parameter and seek ranges of $\nu$ where MMOs
are found. If the Hopf bifurcation at $\nu = \nu_H$ is supercritical, then, for parameters
close enough to the Hopf bifurcation, the limit set of $W^u(p)$ is just the bifurcating
stable periodic orbit. The onset of MMOs is observed to occur at a distance $\nu = O(\varepsilon)$
from the Hopf bifurcation due to a new type of bifurcation [87]. This bifurcation
occurs at parameters where $p$ is a saddle-focus and $W^u(p)$ is tangent to the two-
dimensional repelling Fenichel manifold $S_\varepsilon^r$. At first glance one might think that two
unstable objects in a dynamical system cannot intersect. However, recall that $W^u(p)$
consists of trajectories that approach $p$ as $t \to -\infty$, while $S_\varepsilon^r$ consists of forward
trajectories that remain slow for an $O(1)$ time on the slow time scale. Consequently,
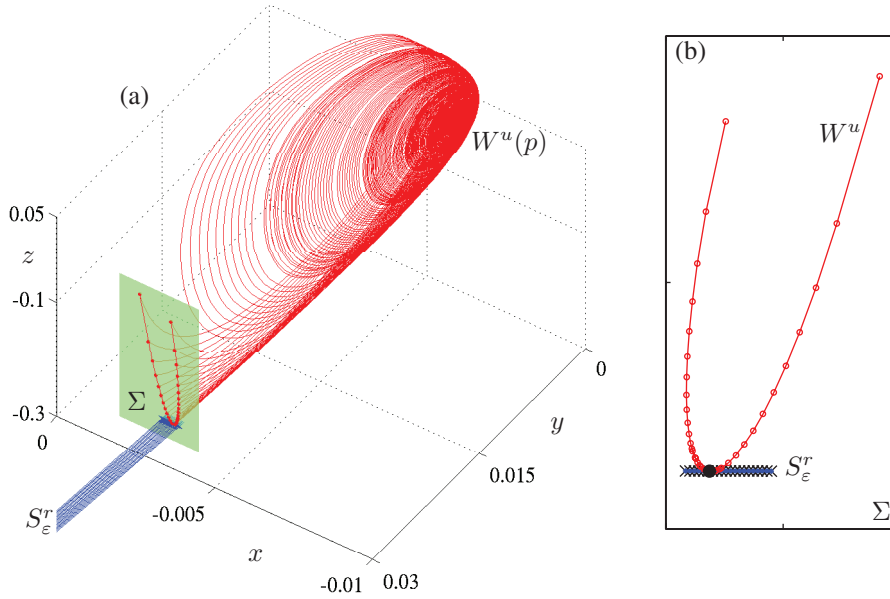
**Fig. 11**   *Tangency between the unstable manifold $W^u(p)$ of the equilibrium and the repelling slow manifold $S^r_\varepsilon$ of (3.7) with $(\nu, a, b, c, \varepsilon) = (0.007057, 0.008870, -0.5045, 1.17, 0.01)$. Panel (a) shows trajectories of $W^u(p)$ (red) and $S^r_\varepsilon$ (blue) that are terminated on the green cross-section $\Sigma$ defined by $y = 0.3$. The intersections $W^u(p) \cap \Sigma$ (with points on computed trajectories marked "o") and $S^r_\varepsilon \cap \Sigma$ (with points on computed trajectories marked "x") are shown in panel (b).*

it is possible for a single trajectory to satisfy the criteria to belong to both of these objects. Figure 11 illustrates an example of a tangency between $W^u(p)$ and $S^r_\varepsilon$ for (3.7) with $(\nu, a, b, c, \varepsilon) = (0.007057, 0.008870, -0.5045, 1.17, 0.01)$ (note that $\nu = O(\varepsilon)$ and, hence, is very close to $\nu_H \approx -8.587 \times 10^{-5}$). Shown are a collection of trajectories on $W^u(p)$ (red) that start close to $p$ and end in the cross-section $\Sigma := \{y = 0.3\}$, together with a collection of trajectories on $S^r_\varepsilon$ that start on the repelling sheet of the critical manifold and also end in $\Sigma$; see section 8.1 for details of the method used to compute these manifolds. Figure 11(b) shows the tangency of the two intersection curves of $W^u(p)$ and $S^r_\varepsilon$ with $\Sigma$.

The number of SAOs that an MMO periodic orbit $\Gamma$ makes along $W^u(p)$ is determined by how close $\Gamma$ comes to $p$ and by the ratio of real to imaginary parts of the complex eigenvalues of $p$. The only way to approach $p$ is along its stable manifold $W^s(p)$, so an MMO like that displayed in Figure 9 must come very close to $W^s(p)$. The minimum distance $d$ between an MMO and $W^s(p)$ is analogous to the distance $\delta$ of a trajectory from the primary strong canard in the case of folded nodes. Unlike for the case of a folded node, the maximal amplitude of the SAOs observed near $W^u(p)$ is largely independent of $d$. What does change as $d \to 0$ is that the epoch of SAOs increases in length and begins with oscillations that are too small to be detectable. There has been little investigation of how the parameters of the normal form (3.7) influence $d$, but Figure 8 in Guckenheimer [87] illustrates that $d$ depends upon the

parameter $c$ in a complex manner. It is known that there are parameter regions where the global returns of MMO trajectories are close to $W^s(p)$. Nevertheless, since MMOs are not found immediately adjacent to a supercritical Hopf bifurcation, the ratio of real to imaginary parts of the complex eigenvalues remains bounded away from 0 on MMO trajectories. This prevents the appearance of extraordinarily long transients with oscillations that grow arbitrarily slowly like those found near a subcritical Hopf bifurcation; see section 5 and also [89, Figure 5].

The singular Hopf and folded-node mechanisms for creating SAOs are not mutually exclusive and can be present in a single MMO in the transition regime with $\nu = O(\varepsilon^{1/2})$. The specific behavior that one finds depends in part on whether the equilibrium $p$ near the singular Hopf bifurcation is a saddle-focus with a pair of complex eigenvalues or a saddle with two real eigenvalues. The MMO displayed in Figure 21 contains some SAOs that lie inside the rotational sectors between the attracting and repelling slow manifolds and some SAOs that follow the unstable manifold of the saddle-focus equilibrium. On the other hand, we note that SAOs cannot be associated with a saddle equilibrium that has only real eigenvalues; this occurs in a parameter region with $\nu > (a + c)\varepsilon^{1/2}$ (to leading order), but $\nu = O(\varepsilon^{1/2})$ here. Hence, in this situation SAOs are solely associated with the folded-node-type mechanism described for $\nu = O(1)$ (that is, $\mu = O(1)$). Krupa and Wechselberger [144] analyzed the transition regime $\nu = O(\varepsilon^{1/2})$ and showed that the folded-node theory can be extended into this parameter regime provided the global return mechanism projects into the funnel region.

Slow-fast systems with a single fast variable, like the ones we have used to study folded nodes and singular Hopf bifurcations, do not have fast oscillations. Their fast subsystems are one-dimensional, and the trajectories of vector fields on the line are constrained to be monotone. This means that LAOs in these systems are always relaxation oscillations whose trajectories cross a critical manifold in order to change their orientation along the fast direction. Models of MMOs with LAOs that do not appear to be relaxation oscillations must, therefore, have at least two fast variables; the oscillations of the BZ reaction displayed in Figure 1 are such an example. The next section discusses systems with three time scales. Such systems can be viewed as intermediate between the cases of one and two fast variables, and they do feature "simple" MMOs with $L > 1$.

**3.3. MMOs in Three-Time-Scale Systems.** When the coefficients $\nu$, $a$, $b$, and $c$ in the normal forms (3.5) and (3.7) of the singular Hopf bifurcation are of order $O(\varepsilon)$ or smaller, then $z$ evolves slowly relative to $y$ and the system actually has three time scales: fast, slow, and superslow. Krupa, Popović, and Kopell [139] studied this regime with geometric methods and asymptotic expansions for the case $a = c = 0$. They observed MMOs for which the amplitudes of the SAOs remain relatively large. Their analysis is based upon rescaling the system such that it has two fast variables and one slow variable. To make the three-time-scale structure explicit, we set $\nu = \varepsilon\hat{\nu}$, $a = \varepsilon\hat{a}$, $b = \varepsilon\hat{b}$, and $c = \varepsilon\hat{c}$. Rescaling the singular Hopf normal form (3.7) of section 3.2 by $x = \varepsilon^{1/2}\,\bar{x}$, $y = \varepsilon\,\bar{y}$, $z = \varepsilon^{1/2}\,\bar{z}$, and $t = \varepsilon^{1/2}\,\bar{t}$ yields

(3.8)
$$\begin{cases} \dot{x} = y - x^2 - \varepsilon^{1/2}x^3, \\ \dot{y} = z - x, \\ \dot{z} = \varepsilon(-\hat{\nu} - \varepsilon^{1/2}\,\hat{a}\,x - \varepsilon\,\hat{b}\,y - \varepsilon^{1/2}\,\hat{c}\,z), \end{cases}$$

which is still a singularly perturbed system, but now has two fast variables, $x$ and $y$, and a slow variable $z$. An equilibrium lies within an $O(1)$-size domain around the
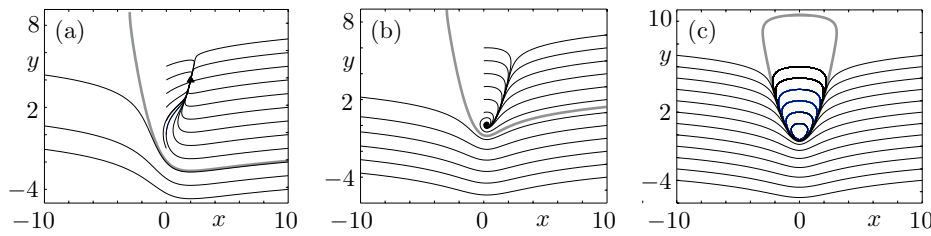
**Fig. 12** *Phase portraits of system (3.9) for three different values of $z$. Shown are several trajectories (black) and one trajectory (gray) that approximates a separatrix. For each $z$, there is a single equilibrium point $p$ at $(x, y) = (z, z^2)$. Panels (a)–(c) are for $z = 2$, $z = 0.25$, and $z = 0$, for which $p$ is a stable node, a stable focus, and a center surrounded by a continuous family of periodic orbits, respectively. The boundary of this family is the maximal canard.*

origin if $\hat{\nu} = O(\varepsilon^{1/2})$ or smaller, i.e., $\nu = O(\varepsilon^{3/2})$ or smaller. This equilibrium plays an important role in the dynamics if it is of saddle-focus type; in particular, it undergoes a Hopf bifurcation for $\hat{\nu} = O(\varepsilon)$, i.e., $\nu = O(\varepsilon^2)$.

We start the analysis by considering the two-dimensional layer problem of (3.8), in which $z$ acts as a parameter. It is given by

(3.9)
$$\begin{cases} \dot{x} = y - x^2, \\ \dot{y} = z - x, \\ \dot{z} = 0 \end{cases}$$

and is exactly the same as the system obtained in the analysis of the planar canard problem, where the parameter $\lambda$ is replaced by $z$; compare with system (2.7). System (3.9) has a unique equilibrium $p$ for each value of $z$, given by $(x, y) = (z, z^2)$. Figure 12 shows phase portraits of (3.9) in the $(x, y)$-plane for three different values of $z$, namely, $z = 2$, $z = 0.25$, and $z = 0$ in panels (a), (b), and (c), respectively. For $z > 0$, the equilibrium $p$ is an attracting fixed point in the $(x, y)$-plane; it is a node for $z > 1$ and a focus for $0 < z < 1$; note that this information also determines the type of equilibrium of (3.8) obtained for $\hat{\nu} = O(\varepsilon^{1/2})$ to leading order—the same argument can also be used to determine the basin boundary of the saddle-focus equilibrium in section 3.2. The basin boundary of $p$ is an unbounded trajectory that is shown in gray in panels (a) and (b). When $z = 0$, the vector field (3.9) has a time-reversing symmetry that induces the existence of a family of periodic orbits. Indeed, the function

$$H(x, y) = \exp(-2y)\,(y - x^2 + 1/2)$$

is an integral of the motion and the level curve $H = 0$ is a parabola that separates periodic orbits surrounding $p$ (the origin) from unbounded orbits that lie below the parabola and become unbounded with $x \to \pm\infty$ in finite time.

When $z$ remains small and is slowly varying compared to $x$ and $y$, system (3.8) can be viewed as a perturbation of (3.9). In this situation, changes in $H$ can be used to monitor the SAOs of trajectories. We demonstrate this with a numerical study of MMOs in the (unscaled) singular Hopf normal form (3.7), where we focus on the case $a = c = 0$ studied in [139]. We further fix $b = -0.005$ and $\varepsilon = 0.01$ and vary the parameter $\nu$. Then $\dot{z} = -\nu - by$, which implies that $z$ increases when $y$ is large but decreases when the system has SAOs and $y$ is small. More precisely, we want
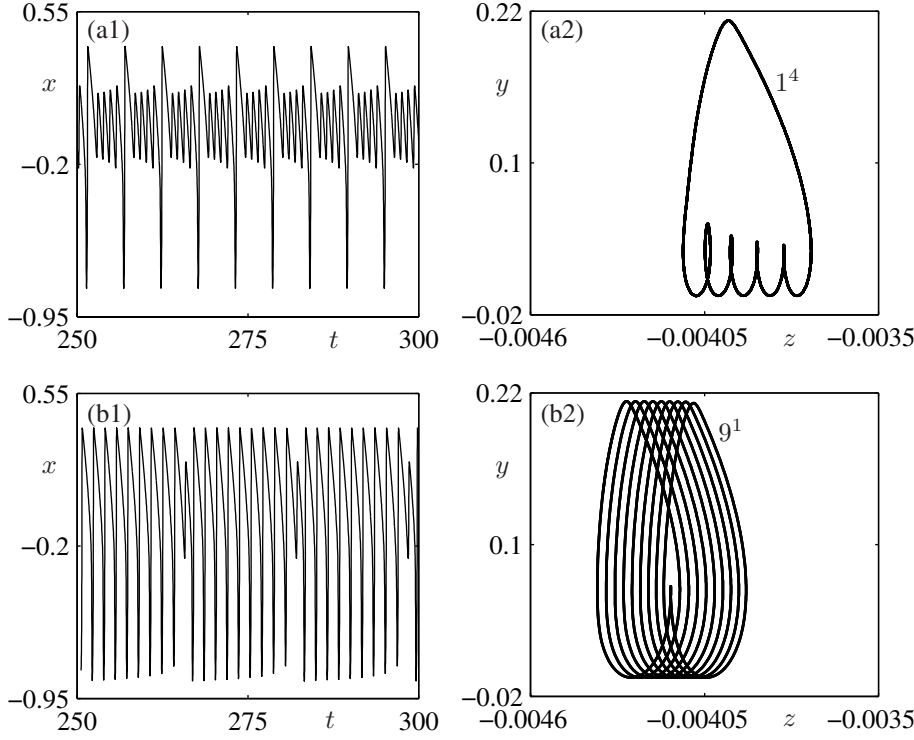
**Fig. 13**  *Stable periodic MMOs of system (3.7) with $(a, b, c, \varepsilon) = (0, -0.005, 0, 0.01)$. Row (a) shows the periodic MMO with signature $1^4$ for $\nu = 0.00015$ as a time series of $x$ in panel (a1) and in projection onto the $(z, y)$-plane in panel (a2); similar projections are shown in row (b) for $\nu = 0.00032$, where the periodic MMO has signature $9^1$.*

the average value of $z$ to increase during epochs of SAOs and decrease during epochs of LAOs. The changes in $z$ should be of sufficient magnitude to drive the trajectory across the slow manifolds and trigger a transition between these epochs.

Figure 13(a) displays a periodic MMO with signature $1^4$ found at $\nu = 0.00015$ (which is of order $O(\varepsilon^2)$). Note that, for this choice of parameters, $\dot{z} = 0$ on the plane $y = 0.03$. The projection in panel (a2) of the orbit onto the $(z, y)$-plane shows that $z$ decreases approximately from $-0.003713$ to $-0.004143$, while the trajectory makes four SAOs, and $z$ increases during a single LAO. Note that system (3.7) also possesses two equilibria with $z$-coordinates given by $\pm\sqrt{-\nu/(b\,\varepsilon)}$, which equals $\pm\sqrt{3}$ in this case. However, the MMO signature shown in panel (a2) is confined to the area near the origin (in the $z$-direction), so these two equilibria have no influence on the dynamics.

As $\nu$ increases, the value of $y$ for which $\dot{z} = 0$ increases, and trajectories have a propensity to pass more quickly through the region of SAOs. Figure 13(b) shows a periodic MMO with signature $9^1$ obtained for $\nu = 0.00032$. This value of $\nu$ lies close to the upper end of the range in which MMOs seem to exist for the chosen values of $(a, b, c, \varepsilon) = (0, -0.005, 0, 0.01)$, and $\dot{z} = 0$ when $y = 0.064$. As the projection in panel (b2) illustrates, the average value of $z$ increases ($|z|$ decreases) during each LAO, but it takes nine LAOs before it crosses the threshold into the region of SAOs. On the other hand, a single SAO takes the trajectory back to the region of LAOs.
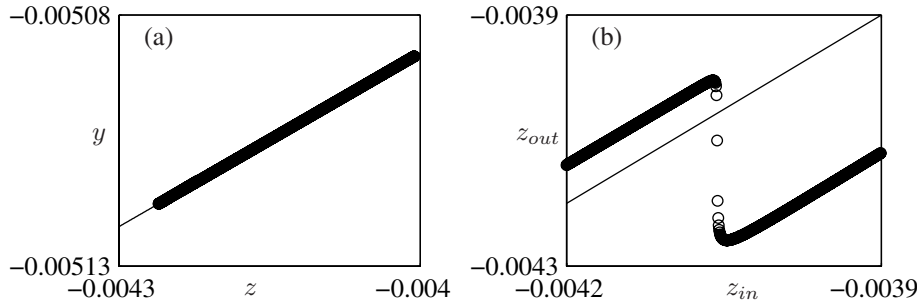
**Fig. 14** *Return map of system* (3.7) *with* $(\nu, a, b, c, \varepsilon) = (0.0003, 0, -0.005, 0, 0.01)$ *to the section* $x = 0$. *Panel* (a) *shows that the return is almost one dimensional along a line that is approximately given by* $y = 0.1153\, z - 0.004626$. *The* $z$-*coordinates of the returns for initial conditions along this line with* $z \in [-0.0043, -0.004]$ *are plotted versus their initial* $z$-*values in panel* (b).

For intermediate values of $\nu \in (0.00015, 0.00032)$, the system displays aperiodic MMOs as well as periodic MMOs with a variety of signatures. These signatures can be analyzed via an approximately one-dimensional return map to a cross-section at $x = 0$. Returns to this cross-section with $x$ decreasing appear to lie along a thin strip; this is illustrated in Figure 14(a) for $\nu = 0.0003$, for which the system appears to have aperiodic MMOs. The thin strip in Figure 14(a) is approximately given by the line $y = 0.1153\, z - 0.004626$ (and $x = 0$). If we take 600 initial conditions on this line with $z \in [-0.0043, -0.004]$, then their next returns to the cross-section fall onto two segments that are close to the initial line and within the segment $z \in [-0.0043, -0.004]$. Figure 14(b) graphs these returns, showing the $z$-coordinates $z_{\text{out}}$ of returns of the 600 initial conditions versus their initial $z$-coordinates $z_{\text{in}}$; the diagonal $z_{\text{out}} = z_{\text{in}}$ is also pictured. This figure suggests that the return map near the line segment can be approximated by a rank-one map with two segments of slopes close to one, separated by a steep segment for initial values $z_{\text{in}} \approx -0.004055$. The return map increases $z$ on the left "branch" of this map and decreases $z$ on the right branch. This is the behavior described above, since larger values of $z$ correspond to SAOs and smaller values to LAOs. Trajectories that do not hit the steep section of the map go back and forth repeatedly between the two branches. As $\nu$ varies, the "shape" of the return map remains qualitatively the same: the two branches still have slopes close to one, but their offset from the diagonal varies. Approximately for $\nu < 0.00013$, the image of the right branch, representing SAOs, maps to itself, while for $\nu > 0.00034$, the image of the left branch maps to itself, and the system only has a large periodic relaxation oscillation with no SAOs. In the range of $\nu$ where MMOs do exist, *kneading theory* for one-dimensional maps [41] can be applied to the numerically generated return maps to predict the signatures of the MMOs.

Further insight into the steep segment of the return map at $z = z_{\text{in}} \approx -0.004055$ comes from computing intersections of the attracting and repelling slow manifolds. We computed forward trajectories from initial conditions on the attracting sheet (with $x < -\frac{2}{3}$) and backward trajectories from initial conditions on the repelling sheet of the critical manifold to their intersection with the cross-section $\{x = 0\}$. Since the trajectories quickly converge to the attracting and repelling slow manifolds, their intersections with $\{x = 0\}$ give a good approximation of the intersection curves of the slow manifolds with $\{x = 0\}$. These two intersection curves have one point in

common, which is approximately $(y, z) = (-0.0050941, -0.0040564)$. Hence, this point lies in the region that gives rise to the steep segment shown in Figure 14(b). By definition, the intersection of the attracting and repelling slow manifolds is a maximal canard. Initial conditions on the cross-section $\{x = 0\}$ to one side of the repelling manifold result in SAOs, while trajectories on the other side result in fast jumps to the other sheet of the attracting slow manifold (with $x > 0$). Thus, we have confirmed numerically that canard orbits separate the two branches of the return map displayed in Figure 14(b); compare also with Figure 7(a), which illustrates that the one-dimensional return map calculated near a folded node has several steep sections that correspond to the primary strong canard and the maximal secondary canards of the problem.

**3.4. MMOs Due to the Tourbillon Mechanism of a Dynamic Hopf Bifurcation.** Recall from section 3.3 that the abrupt transitions between SAOs and LAOs in system (3.8) are a consequence of the three-time-scale structure, which allows us to view the system as having two fast variables and only one slow variable. Such a system with two or more fast variables may have a Hopf bifurcation in the layer equations. We now consider this situation, and assume that a pair of complex eigenvalues of the layer equations cross the imaginary axis as one follows a trajectory of the reduced system. Due to the complex eigenvalues in the fast directions, trajectories spiral around the slow manifold, which gives rise to oscillations. The amplitude of such an oscillation initially decreases (while the real part of the complex eigenvalues is negative) and then increase again (after the real part becomes positive). We refer to this situation as a *dynamic Hopf bifurcation*. Our primary goal is to determine when MMOs have SAOs that are associated with a dynamic Hopf bifurcation. Note that, unlike in systems with a single fast variable, this type of SAO is associated neither with a folded singularity of the critical manifold nor with a (singular) Hopf bifurcation of the system for $\varepsilon > 0$.

A well-known example of a dynamic Hopf bifurcation is the phenomenon of delayed Hopf bifurcation. For simplicity, we discuss it here for a system with one slow and two fast variables, the lowest dimensions possible. Consider a segment $L$ on the one-dimensional critical manifold $S$ along which the layer equations undergo a Hopf bifurcation. That means that the linearization of the layer equations along $L$ has a pair of complex eigenvalues $\alpha \pm i\beta$ that cross the imaginary axis transversally. In the case of a supercritical Hopf bifurcation, a one-parameter family of attracting periodic orbits of the layer equations, parameterized by the slow variable, emanates from the point $L_0 \in L$ where $\alpha = 0$. If a trajectory $u(t)$ of the full system comes close to $L$ near a point $L_u \in L$ that lies at a distance $\delta = |L_u - L_0| = O(1)$ from $L_0$, then $u(t)$ will come exponentially close to $L$ on the slow time scale. The layer equations undergo a Hopf bifurcation, but, in analytic systems, $u(t)$ remains close to $L$ for an $O(1)$ distance *after* the Hopf bifurcation has occurred [169]. This *delay* happens because it takes an $O(1)$ time for $u(t)$ to be repelled away from $L$. In particular, $u(t)$ does not immediately follow the periodic orbits of the layer equations emanating from $L_0$. The slow-fast analysis identifies a definite "jump" point (called a *buffer point*) at which $u(t)$ leaves $L$ and approaches the periodic orbits, if it has not done so earlier. There are SAOs along $L$ in a delayed Hopf bifurcation, but they are exponentially small near $L_0$ and the jump from $L$ to the periodic orbits may occur within a single period of the SAOs. Thus, SAOs near a delayed Hopf bifurcation are typically so small that they are unobservable in practical examples. This situation is reminiscent of MMOs associated with folded nodes with $\delta = O(1)$. More specifically, Theorem 3.2 predicts

maximal $1^{k+1}$ MMO signatures but, due to strong contraction toward the primary weak canard $\gamma_w$ on $S_{a,\varepsilon}$, only the final rotation is actually observed; see Figure 7(b4).

In a number of examples, such as those in sections 6 and 7, one actually observes MMOs with SAOs near a dynamic Hopf bifurcation whose amplitudes remain observably large. We adopt the term *tourbillon* from Wallet [235] to describe the trajectories passing through a dynamic Hopf bifurcation with oscillations whose amplitude remains above an observable threshold. We discuss the tourbillon and how it gives rise to MMOs also in systems with one slow and two fast variables. Consider the model system

$$(3.10) \qquad \begin{cases} \dot{x} = -y + z\,x, \\ \dot{y} = x + z\,y, \\ \dot{z} = \varepsilon \end{cases}$$

that is obtained by linearization of the layer equations for a dynamic Hopf bifurcation. This equation is separable in polar coordinates, yielding $\dot{r} = \varepsilon\,t\,r$ for trajectories that have initial conditions in the plane $\{z = 0\}$. Hence, the general solution is $r(t) = r(0)\exp(\varepsilon\,t^2/2)$, which means that the amplitude of a solution decreases for $z < 0$ and then increases for $z > 0$. We conclude that $\frac{r(1/\sqrt{\varepsilon})}{r(0)} = \exp(\frac{1}{2})$ and that the oscillations have almost constant amplitude over a time interval of $1/\sqrt{\varepsilon}$. If the $r$-coordinate of a trajectory decreases to $r = 1$ at a value of $z$ that is $O(\sqrt{\varepsilon})$, then the minimum amplitude of the oscillations associated with the dynamic Hopf bifurcation will still be observable. The amplitudes of these oscillations and the coupling of $\varepsilon$ with the distance of approach to the dynamic Hopf point characterize the tourbillon regime and distinguish it from a delayed Hopf bifurcation. When $\varepsilon$ is fixed in a system, the distinction between a delayed Hopf point and a tourbillon becomes blurred, but it is clear in many examples.

System (3.10) describes SAOs with distinctly nonzero amplitudes locally near the point where the dynamic Hopf bifurcation occurs in the layer equations. However, it does not account for characteristic abrupt transitions at the beginning and end of an SAO epoch within an MMO, such as those in sections 6 and 7, because these transitions depend upon mechanisms that are not part of the local analysis of system (3.10). There is as yet no comprehensive study of possible geometric mechanisms that determine the sudden start and the end of a section of SAOs arising from a tourbillon. This paper largely avoids this issue and concentrates on local mechanisms for generating the SAOs of MMOs. Nevertheless, the following example illustrates one mechanism for an abrupt jump away from SAOs of a tourbillon. Consider a "dynamic" section through the unfolding of the codimension-two Bogdanov–Takens bifurcation [90], defined as

$$(3.11) \qquad \begin{cases} \dot{x} = y, \\ \dot{y} = \lambda + z\,y - x^2 - x\,y, \\ \dot{z} = \varepsilon. \end{cases}$$

As before, we regard $z$ as a slowly varying parameter. For $\lambda > 0$ and $\varepsilon = 0$, the system has two straight lines of equilibria defined by $x = \pm\sqrt{\lambda}$ and $y = 0$. A supercritical Hopf bifurcation occurs along the line of equilibria with $x > 0$. The family of periodic orbits born at this bifurcation terminates at a homoclinic orbit. Moreover, there is always a bounded region of the $(x, y)$-plane in which oscillations around the equilibrium occur; this is the tourbillon region. The line of (saddle) equilibria with $x < 0$ of the layer equations perturbs to a Fenichel manifold of saddle type and its stable and unstable
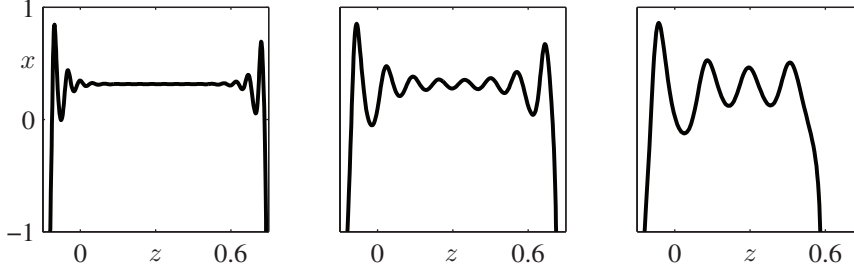
**Fig. 15** *Time series of the x-coordinate of a trajectory of* (3.11) *with initial point* $(x, y, z) = (-1, 0.8, -0.12)$. *Panels* (a)–(c) *are for* $\lambda = 0.1$ *and for* $\varepsilon = 0.006$, $\varepsilon = 0.012$, *and* $\varepsilon = 0.02$, *respectively.*

manifolds guide the entrance and exit to the tourbillon in this example. As we have seen, the number of oscillations and their minimum amplitude is determined by the magnitude both of the initial condition and of $\varepsilon$. This is illustrated in Figure 15 with trajectories of system (3.11) for $\lambda = 0.1$ and different values of $\varepsilon$, all starting from the initial condition $(x, y, z) = (-1, 0.8, -0.12)$ that lies outside the tourbillon region. Note that $x$ and $y$ are $O(1)$ quantities, and so the condition for a tourbillon is that $|z|$ is of order $\sqrt{\varepsilon}$. In Figure 15(a) for $\varepsilon = 0.006$ we do not find a tourbillon but observe oscillations that decay rapidly, are very small for a while, and then grow rapidly again before the trajectory jumps away. In panel (b) for $\varepsilon = 0.012$, on the other hand, the oscillations decay and then grow more gradually and they remain of observable size throughout. We conclude that $\varepsilon$ is now just about large enough to speak of a tourbillon region, passage through which results in seven SAOs before the jump occurs. For even larger values of $\varepsilon$ the same initial condition results in oscillations that maintain an almost constant amplitude; see Figure 15(c) for $\varepsilon = 0.02$. Observe that, owing to the faster drift through the region near the Hopf bifurcation in the layer system, we now find only three SAOs before the trajectory jumps away.

It is interesting to compare the SAOs associated with a tourbillon with those occurring near a folded node or near a singular Hopf bifurcation. The first difference between these types of SAOs is that the period of the oscillations is $O(\varepsilon)$ (slow time) for the tourbillon, while it is $O(\sqrt{\varepsilon})$ for the other two cases. Second, the minimum amplitude and the number of SAOs for a tourbillon are governed by the singular perturbation parameter and the distance of the global return to the delayed Hopf bifurcation point. For the folded node, the eigenvalue ratio $\mu$ and the distance $\delta$ of the global return to the strong canard determine the minimum amplitude and number of the SAOs, while for the singular Hopf bifurcation these properties of the SAO are determined only by the distance of the global return to the stable manifold of the saddle-focus equilibrium. Finally, the termination of the SAOs for a tourbillon depends upon either a global mechanism or some defined threshold for the amplitude of SAOs. There is no distinguished termination mechanism associated with a folded node, but the intersections of the unstable manifold of the equilibrium and the repelling slow manifold typically limit the amplitude of SAOs near a singular Hopf bifurcation.

**3.5. Summary of Local Mechanisms for SAOs.** We now summarize the main results of this review section on the local mechanisms that give rise to MMOs. For systems with a single fast variable, the local mechanisms responsible for SAOs must

involve a mixture of the two time scales. We distinguish three regions near folded nodes and folded saddle-nodes that yield MMOs:

1. *Folded Nodes:* If the parameters satisfy suitable order conditions ($\nu = O(1)$) so that no equilibrium of the full system is near the folded node, then the theory of section 3.1 applies and SAOs are due to the *twisting of slow manifolds*.

2. *Singular Hopf:* As is shown in the section 3.2, the dynamics near a singular Hopf bifurcation ($\nu = O(\varepsilon)$) tends to be quite complicated. SAOs occur when the trajectory follows the *unstable manifold of a saddle-focus*.

3. *Transition Regime:* The folded-node and singular Hopf regimes are separated by a transition regime with intermediate values of $\nu = O(\sqrt{\varepsilon})$. Extensions of the folded-node theory have been developed in [144]; note that the parameter $\mu$ in [144] not only represents the eigenvalue ratio, but also describes the distance of the equilibrium to the folded node in a blown-up system. In this transition regime, it is possible for the SAOs to pass through the rotational sectors of the folded node *as well as* spiral along the unstable manifold of the saddle-focus equilibrium.

In systems with at least two fast variables the tourbillon provides a different local mechanism that generates SAOs. Here, the layer equations have complex eigenvalues and the SAOs are aligned with the fast directions of the system. Little systematic study of the tourbillon as a mechanism that generates MMOs has been carried out, and the theory remains fragmentary.

Finally, three-dimensional systems with three time scales can exhibit all of the mechanisms discussed in this section. In other words, a three-time-scale system may be considered as having two slow variables, in which case the folded-node and singular Hopf mechanisms may be found, or, alternatively, as having two fast variables, which allows for the possibility of a tourbillon.

The following sections are case studies that illustrate these different local mechanisms for MMOs:

- The *Koper model* in section 4 is a three-dimensional slow-fast system with a folded node and a supercritical singular Hopf bifurcation.
- The three-dimensional *reduced Hodgkin–Huxley model* in section 5 also features a folded node, but has a subcritical singular Hopf bifurcation.
- The four-dimensional *Olsen model of the peroxidase-oxidase reaction* in section 6 displays MMOs associated with a tourbillon.
- The *Showalter–Noyes–Bar-Eli model* in section 7 is a seven-dimensional system that exhibits MMOs. The global mechanism that organizes these MMOs is unknown, but we show here that their SAOs are due to a tourbillon.

**4. MMOs in the Koper Model of Chemical Reactors.** Our first case study is a system introduced by Koper [123]. We use it to illustrate how MMOs arise near a folded node and near a (supercritical) singular Hopf bifurcation in a specific model equation. The equations of the Koper model are

(4.1)
$$\begin{cases} \varepsilon_1 \, \dot{x} = k \, y - x^3 + 3 \, x - \lambda, \\ \quad \dot{y} = x - 2 \, y + z, \\ \quad \dot{z} = \varepsilon_2 \, (y - z), \end{cases}$$

where $\lambda$ and $k$ are parameters. Koper studied this three-dimensional idealized model of chemical reactions with MMOs. While this example is well known, we revisit its analysis and enhance it by using the recently developed theory outlined in the pre-

vious sections. When $\varepsilon_1$ and $\varepsilon_2$ are both small, system (4.1) has three time scales; when only $\varepsilon_1$ is small, it is a slow-fast system with two slow variables $y$ and $z$ and one fast variable $x$. We note that a two-dimensional variant of (4.1) was first studied by Boissonade and De Kepper [26] in their efforts to understand bistability and oscillations of chemical systems. The first analysis of MMOs in the three-dimensional extended model was carried out by Koper, who explained the MMOs by invoking the presence of a Shil'nikov homoclinic bifurcation.

As mentioned in section 3.2, the Koper model (4.1) is a rescaled subfamily of the cubic normal form (3.7) for the singular Hopf bifurcation. To see this, replace $(x, y, z)$ in system (4.1) by $(u, v, w)$ and consider the affine coordinate change

$$x = \frac{u - 1}{3}, \quad y = \frac{k\,v - \lambda + 2}{27}, \quad z = \frac{2\,v - w - 1}{3}.$$

Now also scale time by the factor $\frac{-k}{9}$, where we assume that $k < 0$. Then (4.1) becomes (3.7) with $\varepsilon = -k\,\varepsilon_1/81$, $a = 18/k$, $b = 81\,\varepsilon_2/k^2$, $c = -9\,(\varepsilon_2 + 2)/k$, and $\nu = (3\,\varepsilon_2\,\lambda - 6\,\varepsilon_2 - 3\,k\,\varepsilon_2)/k^2$. Note that the coefficients of the normal form satisfy

$$2\,b - a\,c + a^2 = 0,$$

which means that the Koper model (4.1) is only equivalent to a subfamily of the singular Hopf normal form (3.7). However, (4.1) still has a folded node and a singular Hopf bifurcation in certain parameter regimes.

Let us first analyze the parameter regimes where SAOs are organized by a folded node. To this end, we work with both system (4.1) and the equivalent system

(4.2)
$$\begin{cases} \varepsilon_1\,\dot{x} = y - x^3 + 3\,x, \\ \quad\dot{y} = k\,x - 2\,(y + \lambda) + z, \\ \quad\dot{z} = \varepsilon_2\,(\lambda + y - z), \end{cases}$$

which we refer to as the symmetric Koper model, because it has the symmetry

(4.3)
$$(x, y, z, \lambda, k, \tau) \to (-x, -y, -z, -\lambda, k, \tau).$$

System (4.2) is obtained by replacing $(x, y, z)$ in system (4.1) by $(u, v, w)$ and applying the coordinate change $x = u$, $y = k\,v - \lambda$, and $z = k\,w$. We focus our analysis on the case $\varepsilon_2 = 1$ and consider (4.2) as a system with two slow variables. Observe that the critical manifold of (4.2),

$$S = \{(x, y, z) \in \mathbb{R}^3 \mid y = x^3 - 3\,x =: c(x)\},$$

does not depend on $k$ and $\lambda$. This cubic-shaped critical manifold $S$ has two fold curves $F_\pm = \{(x, y, z) \in \mathbb{R}^3 \mid x = \pm 1, y = \mp 2\}$, which gives the decomposition

$$S = S^{a,-} \cup F_- \cup S^r \cup F_+ \cup S^{a,+},$$

where $S^{a,-} = S \cap \{x < -1\}$, $S^r = S \cap \{-1 < x < 1\}$, and $S^{a,+} = S \cap \{1 < x\}$ are normally hyperbolic. Note that $S^{a,\pm}$ are attracting and $S^r$ is repelling. To derive the desingularized slow flow on $S$ we consider the algebraic equation $0 = y - c(x)$, obtained by setting $\varepsilon_1 = 0$ in (4.2), and differentiate implicitly with respect to $\tau$. Then the time rescaling $\tau \mapsto \tau(3\,x^2 - 3)$ gives

(4.4)
$$\begin{cases} \dot{x} = k\,x - 2\,(c(x) + \lambda) + z, \\ \dot{z} = (3\,x^2 - 3)\,(\lambda + c(x) - z). \end{cases}$$
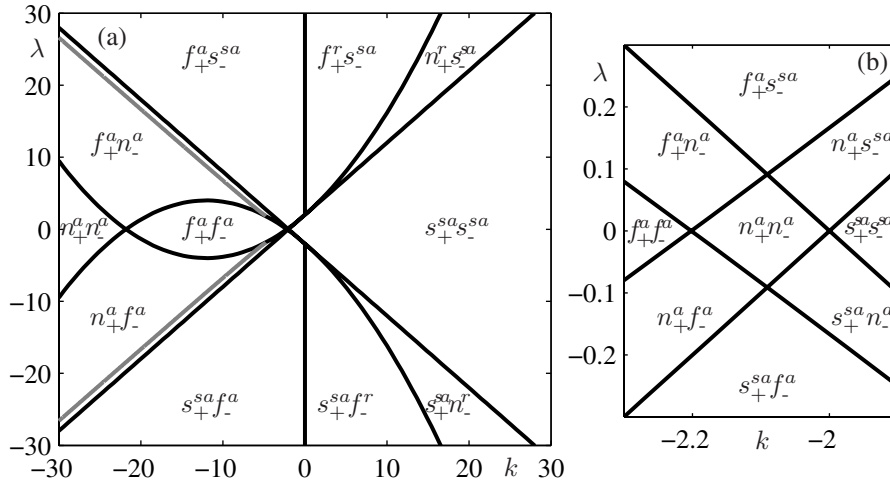
**Fig. 16**  *The "singular" bifurcation diagram in the $(k, \lambda)$-plane of the desingularized slow flow (4.4). Shown are the folded saddle-node of type II (straight lines), the transition from a folded node to a folded focus (parabolas), and the curve indicating where the candidate trajectory from the folded node returns with $\delta = 0$ (gray curve, obtained numerically), which is not shown in panel (b). Panel (a) gives a global view and panel (b) is an enlargement of the region near the right intersection point of the two parabolic curves. The types of folded equilibria in each parameter region are indicated as follows: $f =$ folded focus, $n =$ folded node, and $s =$ folded saddle. The subscripts indicate whether the equilibrium lies on $F_+$ or $F_-$. The superscripts $a$, $r$, and $sa$ stand for attractor, repeller, and saddle, respectively.*

The desingularization reverses the direction of time on the repelling part $S^r$ of $S$. We find folded singularities as equilibria of (4.4) that lie on the fold lines $F_\pm$. The only equilibrium on $F_+$ is $(x, z) = (1, 2\lambda - 4 - k)$, with $y = -2$, and the only one on $F_-$ is $(x, z) = (-1, 2\lambda + 4 + k)$, with $y = 2$. The associated Jacobian matrices are

$$(4.5) \qquad\qquad A_\pm = \begin{pmatrix} k & 1 \\ 6\,(2 + k \mp \lambda) & 0 \end{pmatrix}.$$

By classifying the folded singularities according to their type and stability, we obtain a "singular" bifurcation diagram; we then use results from section 3 to identify possible MMO regions. Figure 16 shows this singular bifurcation diagram in $(k, \lambda)$-space, where we use the notation $e_\pm^h$ to indicate the type $e$ and stability $h$ of the folded singularities; $e$ is $f$, $n$, or $s$ for focus, node, or saddle, and $h$ is $a$, $r$, or $sa$ for attractor, repeller, or saddle, respectively. The different parameter regions are divided by three types of curves. Folded saddle-nodes of type II occur when $\det(A_\pm) = 0 \Leftrightarrow \lambda = \pm(k+2)$. The eigenvalues change from real to complex conjugate along the parabolic curves $\operatorname{tr}(A_\pm)^2 - 4\det(A_\pm) = k^2 + 24\,(k \mp \lambda) + 48 = 0$. The vertical line $\operatorname{tr}(A_\pm) = k = 0$ is the locus where the real part of a complex eigenvalue changes sign. The enlargement in panel (b) resolves the region near $(k, \lambda) = (-2, 0)$.

MMOs are likely to exist in the regions where system (4.2) has a folded node, provided the global return mechanism brings orbits back into the associated funnel region. Recall from section 3.1 the construction of a candidate periodic orbit $\Gamma_c$ that consists of a segment on $S^a$ ending at the folded node, followed by a fast fiber of the layer problem and a global return mechanism. Figure 17(a1) illustrates this
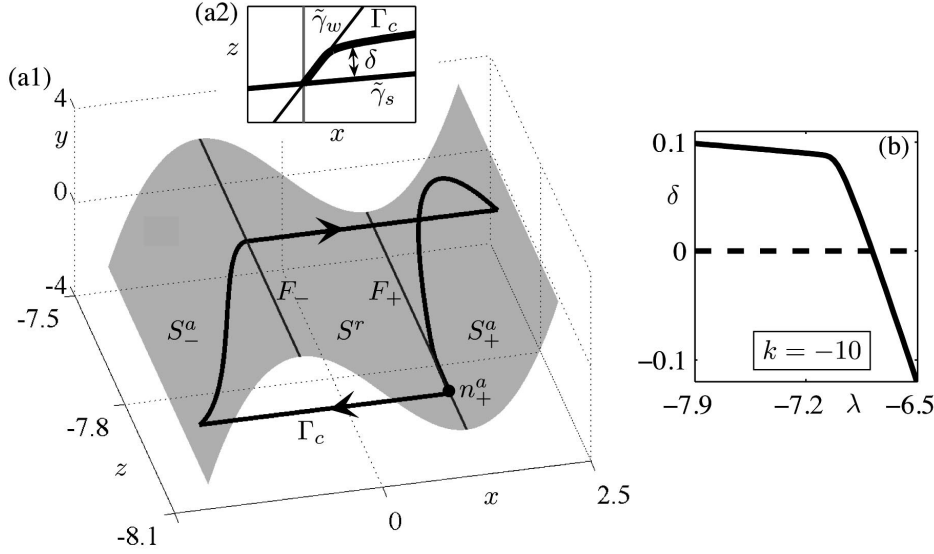
**Fig. 17**   *The candidate periodic orbit $\Gamma_c$ of the folded node $n_+^a$ of (4.2) with $(\varepsilon_1, \varepsilon_2, \lambda, k) = (0, 1, -7, -10)$ returns at a distance $\delta$ from the strong singular canard $\tilde{\gamma}_s$. Panel (a1) shows all of $\Gamma_c$ and panel (a2) an enlargement near $n_+^a$ to illustrate the definition of $\delta$. Panel (b) shows $\delta$ as a function of $\lambda$, with all other parameters fixed. The distance $\delta$ only has meaning for $\delta > 0$ and for values of $\lambda$ larger than its value at the folded saddle-node of type II at $\lambda = -8$.*

construction for a candidate periodic orbit passing through $n_+^a$, where we used $k = -10$ and $\lambda = -7$; this is a computational example of the sketch shown in Figure 8. Starting at $n_+^a$, the candidate $\Gamma_c$ jumps to $S^{a,-}$, which is followed by a slow segment until $\Gamma_c$ reaches $F_-$. After another jump $\Gamma_c$ returns inside the singular funnel, as shown in Figure 17(a2), and we measure the distance $\delta$ to the strong singular canard $\tilde{\gamma}_s$. This distance $\delta$ depends on the parameters; for example, $\delta$ varies as a function of $\lambda$ with $k = -10$ fixed in Figure 17(b). Note that $\delta < 0$ means that $\Gamma_c$ no longer returns to the singular funnel; as long as $\delta > 0$ the candidate $\Gamma_c$ gives rise to periodic MMOs as $\varepsilon_1 > 0$. Hence, the curve in the $(k, \lambda)$-plane along which $\delta = 0$ marks the start of the MMO regime. Figure 16(a) shows the locus of $\delta = 0$ as a gray curve; its symmetrical image corresponds to candidate periodic orbits for $n_-^a$. The two (symmetric) parameter regions bounded by the lines of folded saddle-nodes of type II, where $s_\pm^{sa}$ changes to $n_\pm^a$, and the curves where $\delta = 0$ are the regimes where MMOs are predicted to exist; note that the curves $\delta = 0$ run all the way up to the folded saddle-nodes of type II, which is not shown in Figure 16(b).

Koper identified a parameter region of "complex and mixed-mode oscillations" for $\varepsilon > 0$ by using continuation methods; see Figure 1 on page 75 of [123]. We can interpret his results as perturbations of the MMO regimes we identified in the singular bifurcation diagram in Figure 16(a). To this end we consider bifurcations of equilibria of (4.2) for $\varepsilon > 0$; this analysis was already carried out by Koper [123] for (4.1). The bifurcation diagram in the $(k, \lambda)$-plane is shown in Figure 18 for $\varepsilon_1 = 0.01$, with the saddle-node curves (green) labeled *SN* and the Hopf curves (blue) labeled *H*. Included are the curves of folded saddle-nodes of type II (dashed red) labeled *FSN II*; the curves *FSN II* already predict the "cross-shaped" bifurcation diagram for the full system for
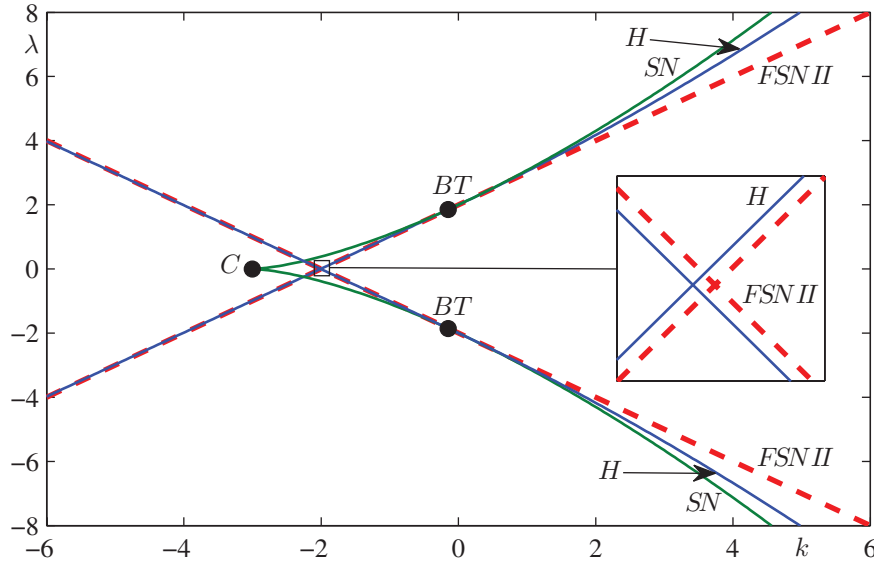
**Fig. 18**  *Bifurcation diagram for equilibria of the full system (4.2) with $\varepsilon_1 = 0.01$. Shown are saddle-node bifurcations (green, labeled SN) and Hopf bifurcations (blue, labeled H). The saddle-node bifurcation curve has a cusp point (labeled C) and meets the Hopf bifurcation curve in two Bogdanov–Takens points (labeled BT). The dashed curves are folded saddle-nodes of type II (red, labeled FSN II) that occur in the singular limit (4.4).*

$\varepsilon_1 > 0$ sufficiently small [26]. In fact, this bifurcation structure persists over a wide range of $\varepsilon_1$. We find the saddle-node and Hopf bifurcation curves as follows. The Jacobian matrix $A$ of (4.2) on the fast time scale has the characteristic polynomial $\sigma^3 + c_2\,\sigma^2 + c_1\,\sigma + c_0$ with coefficients

$$c_2 = 3\,(\varepsilon_1 + x^2 - 1), \quad c_1 = \varepsilon_1\,(\varepsilon_1 + 9\,x^2 - k - 9), \quad c_0 = \varepsilon_1^2\,(3\,x^2 - 3 - k),$$

where $x$ corresponds to an equilibrium, that is, $x^3 - (k+3)\,x + \lambda = 0$. Hence, a saddle-node bifurcation occurs along a curve given by

$$c_0 = -\det(A) = 0 \Leftrightarrow \lambda = \pm 2\,\left(1 + \frac{k}{3}\right)^{3/2},$$

which has a cusp point at $k = -3$ and does not depend on $\varepsilon_1$; the cusp point is labeled $C$ in Figure 18. The Hopf bifurcation is found for $c_0 - c_1\,c_2 = 0$, provided $c_1 > 0$. To first order in $\varepsilon_1$, we find

$$\lambda = \pm\left(2 + k - \frac{1}{3}\,k\,\varepsilon_1 + O(\varepsilon_1^2)\right),$$

which implies that the Hopf bifurcation curve $H$ lies $O(\varepsilon_1)$ close to the curves of folded saddle-nodes of type II, as expected. The saddle-node and Hopf bifurcation curves coincide at two Bogdanov–Takens points (labeled $BT$) for $k = -\frac{1}{2}\,\varepsilon_1$. The MMO regime for $\varepsilon_1 > 0$ lies in the region with $k < 0$ and it has a lower bound with respect to $\lambda$ along a curve that is close to $H$. We discuss this in more detail for fixed
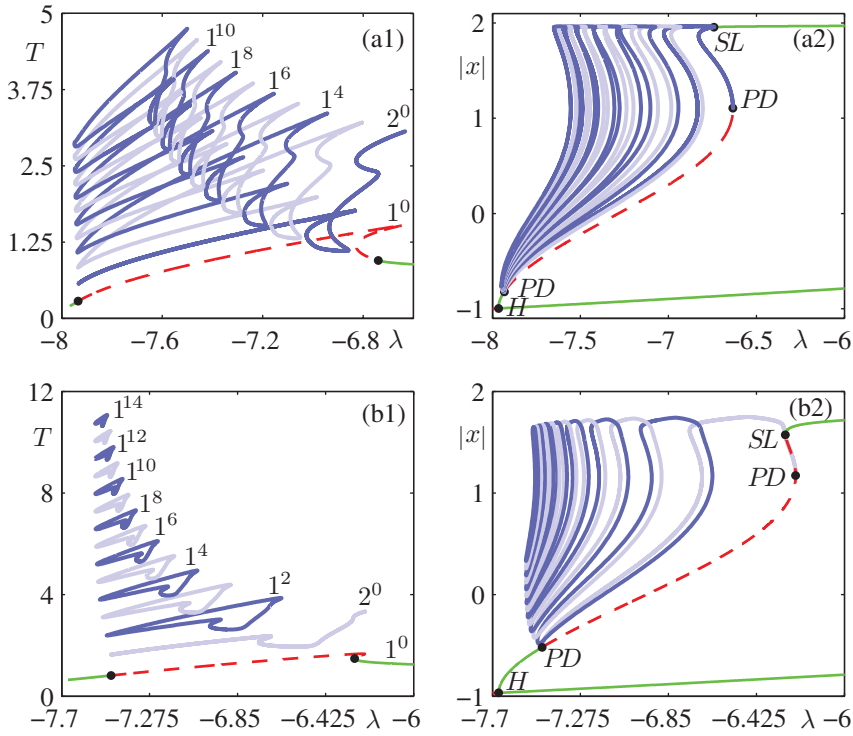
**Fig. 19** *Bifurcation diagram in $\lambda$ for the Koper model (4.1) with $(\varepsilon_2, k) = (1, -10)$. Panels (a1) and (a2) are for $\varepsilon_1 = 0.01$ and panels (b1) and (b2) are for $\varepsilon_1 = 0.1$ as used by Koper. Panels (a1) and (b1) plot the period $T$ and panels (a2) and (b2) the maxima of $|x|$ versus $\lambda$. A branch of periodic orbits (an "MMO" with signature $1^0$) emanates from the Hopf bifurcation $H$ and coexists with isolas of MMOs with different signatures.*

$k = -10$. Note that from now on we use the original equations (4.1), but this does not alter the bifurcation diagrams of the $(k, \lambda)$-plane in Figures 16 and 18.

Koper [123] computed a numerical bifurcation diagram for fixed $k = -10$ and $\varepsilon_1 = 0.1$ with $\lambda > 0$ as the free parameter; he found isolated closed curves of MMO periodic orbits. We computed more detailed bifurcation diagrams, using the same system (4.1) as Koper, where we concentrated on the (symmetrically related) region $\lambda < 0$ and used $\varepsilon_1 = 0.01$ as well as $\varepsilon_1 = 0.1$. The result is shown in Figure 19, where row (a) is for $\varepsilon_1 = 0.1$ and row (b) for $\varepsilon_1 = 0.01$. The vertical axis in panels (a1) and (b1) is the period $T$ of the periodic orbits, while in panels (a2) and (b2) it is the maximum absolute value of the $x$-coordinate. A family of stable periodic orbits emanates from the Hopf bifurcation $H$, but it quickly loses stability in a period-doubling bifurcation $PD$. We abuse notation and label this family $1^0$; the period-doubled family is labeled $2^0$, and note that it appears as a disconnected curve in the $(\lambda, T)$-projection because it has twice the period at the point $PD$. The $1^0$ orbit becomes stable again in a second period-doubling bifurcation, which is quickly followed by a fold (not labeled) that renders it unstable, until a second fold $SL$, after which relaxation oscillations are persistent. The MMOs reside on isolas that exist for the range of $\lambda$ roughly in between the two period-doubling bifurcations. We used alternatingly light- and dark-blue colors to highlight these families; we found MMOs with signatures $1^s$ with $s$ ranging from 2 to 14 as indicated in Figure 19.
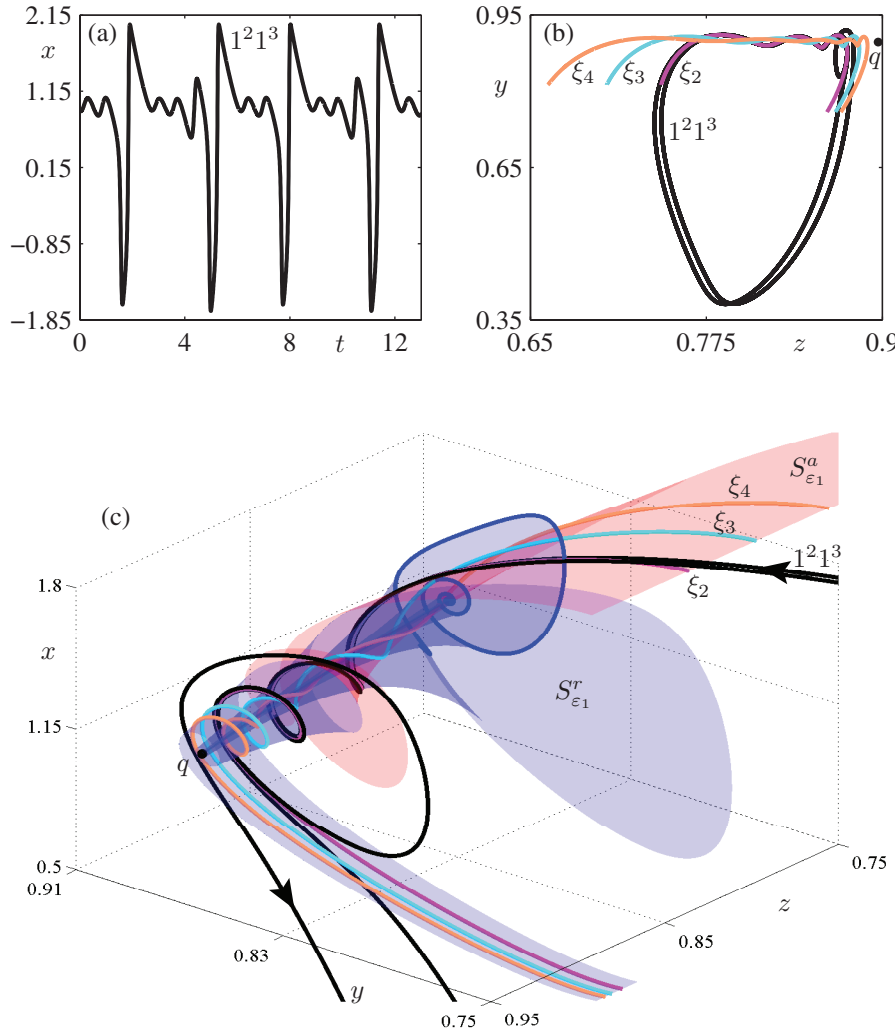
**Fig. 20** *An MMO periodic orbit with signature $1^2 1^3$ (black) generated by a folded-node singularity of (4.1) for $(\varepsilon_1, \varepsilon_2, \lambda, k) = (0.1, 1, -7, -10)$. Panel (a) shows a time series of the x-coordinate. Panel (b) depicts the projection of the periodic orbit onto the $(z, y)$-plane together with nearby canard orbits $\xi_2$, $\xi_3$, and $\xi_4$, and panel (c) shows these objects in phase space together with the attracting and repelling slow manifolds $S_{\varepsilon_1}^a$ (red) and $S_{\varepsilon_1}^r$ (blue), respectively.*

The MMOs on the isolas in Figure 19 are generated by the folded-node mechanism; we refer to section 5 for a more detailed discussion of MMOs on such isolas. Here, we focus on the fact that MMOs with more complicated signatures can be found as soon as the candidate periodic orbit returns close to a maximal canard. Figure 20 shows the stable MMO periodic orbit that exists for $\lambda = -7$; here, we used $\varepsilon_1 = 0.1$. Panel (a) shows a time series of the $x$-coordinate, which identifies the signature of this MMO as $1^2 1^3$; a projection onto the $(z, y)$-plane is shown in panel (b). We computed the attracting and repelling slow manifolds $S_{\varepsilon_1}^a$ and $S_{\varepsilon_1}^r$, respectively. They are shown

in Figure 20(c) along with three maximal secondary canard orbits $\xi_2$, $\xi_3$, and $\xi_4$ that are also drawn in panel (b). The figure shows how both LAOs are funneled into the folded-node region, practically on $S_{\varepsilon_1}^a$ and very close to $\xi_2$. Figure 20(b) illustrates that they are actually separated by $S_{\varepsilon_1}^r$ on either "side" of $\xi_2$, which means that the number of SAOs that follow for one of the LAOs is two, while for the other it is three, as dictated by $\xi_3$. Referring to Figure 7(a), a one-dimensional approximation of the return map will have branches corresponding to trajectories that make increasingly larger numbers of SAOs as they pass through the folded node, and the trajectory shown in Figure 20(c) has returns that alternate between the branches corresponding to two and three SAOs.

We observe that the last of the three SAOs has a distinctly larger amplitude, which Figure 20 suggests is due to this oscillation following a canard and then executing a jump back to $S_{\varepsilon_1}^a$. However, there is also an equilibrium $q$ nearby. For $k = -10$ a singular Hopf bifurcation occurs for $\lambda = \lambda_H \approx -7.67$. We found that the folded node in Figure 20 is at $(x, y, z) = (1, [\lambda - 2]/k, [2\lambda - 4 - k]/k) = (1, 0.9, 0.8)$ and the nearby equilibrium $q$ at $(x, y, z) = (x_q, x_q, x_q)$, where $x_q \approx 0.897$ is a root of $x^3 - (k + 3)\, x + \lambda$.

We find pronounced SAOs generated by a singular Hopf bifurcation if we decrease $\lambda$ closer to the value $\lambda_H$; note that we have to stay above the value of $\lambda$ for which there is a tangency between the unstable manifold $W^u(q)$ of $q$ and the repelling slow manifold $S_{\varepsilon_1}^r$; see also section 3.2. Figure 21 shows the MMO periodic orbit of (4.1) for $\lambda = -7.52$. The time series of the $x$-coordinate shows SAOs that are quite different from the SAOs in Figure 20(a). Figure 21(b) shows an enlarged bifurcation diagram in the $(k, \lambda)$-plane with the parameter location of the two MMOs for Figures 20 and 21 indicated by two black dots at $k = -10$. The Hopf curve (solid blue) and the curve of folded saddle-nodes of type II (dashed red) are labeled $H$ and *FSN II*, respectively. The MMO region is bounded by the curve $\delta = 0$ (dashed black) and the tangency between $W^u(q)$ and $S_{\varepsilon_1}^r$ (dashed cyan); in between the Hopf bifurcation and this tangency bifurcation the periodic orbits have small amplitudes and the transition to MMOs occurs $O(\epsilon)$ away from the Hopf curve. There are two dots in Figure 21(b): the labeled one lies well inside the MMO region and corresponds to the situation shown in Figure 20; the second (unlabeled) dot lies very close to the tangency curve and corresponds to the situation shown in the other panels of Figure 21. Figure 21(c) shows geometrically how the SAOs are organized. The red and blue surfaces are the attracting and repelling slow manifolds $S_{\varepsilon_1}^a$ and $S_{\varepsilon_1}^r$, respectively. During the epoch of SAOs, the MMO periodic orbit lies almost on $S_{\varepsilon_1}^a$ and it cannot pass through $S_{\varepsilon_1}^r$, which twists very tightly and forces a decrease in the amplitudes of the SAOs; this first part of the SAOs is still reminiscent of the passage through a folded node, which lies at $(1, [\lambda - 2]/k, [2\lambda - 4 - k]/k) = (1, 0.952, 0.904)$, and their amplitudes decrease with $\varepsilon_1$. Since $S_{\varepsilon_1}^r$ spirals around the one-dimensional stable manifold of $q$, the MMO periodic orbit comes very close to $q = (x_q, x_q, x_q)$, with $x_q \approx 0.951$. The SAOs that follow are organized by $W^u(q)$ and their amplitudes increase to relatively large values before the LAO.

In summary, if we fix $k$ in Figure 21(b) and increase $\lambda$, we observe the following typical sequence of events near a singular Hopf bifurcation of an equilibrium $q$. For small enough $\lambda$ there are no MMOs and the attractor is an equilibrium. This equilibrium crosses a fold of the critical manifold at *FSN II*, but it remains stable until a supercritical (singular) Hopf bifurcation at distance $O(\varepsilon_1)$ away gives rise to small oscillations. The transition to MMOs occurs after a tangency between $W^u(q)$ and $S_{\varepsilon_1}^r$; for $\lambda$-values just past this tangency the MMOs have many SAOs that all lie near $W^u(q)$. As $\lambda$ increases further, the MMOs exhibit SAOs organized by the folded node. Finally, a crossing of the curve $\delta = 0$ corresponds to a transition to relaxation oscillations.
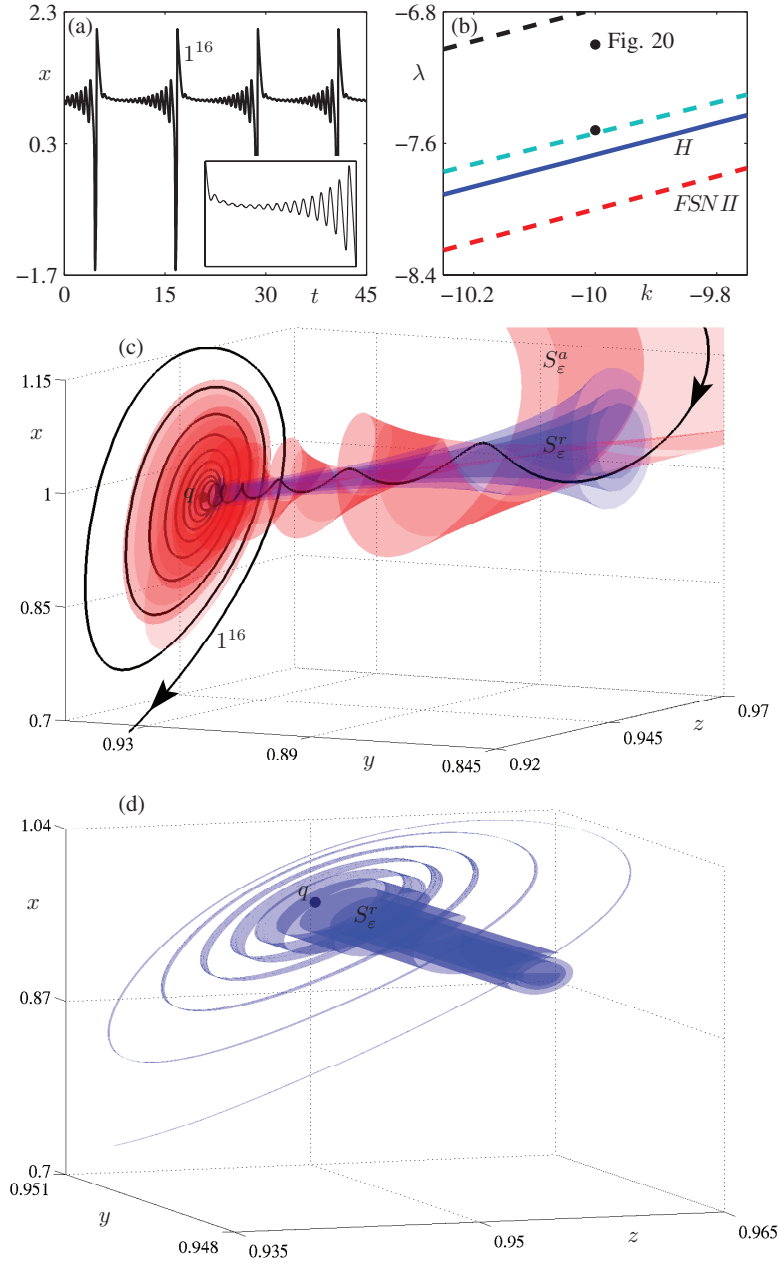
**Fig. 21**  *An MMO periodic orbit near a singular Hopf bifurcation for (4.1) with $(\varepsilon_1, \varepsilon_2, \lambda, k) = (0.1, 1, -7.52, -10)$. Panel (a) shows the time series of the $x$-coordinate. The bifurcation diagram in panel (b) illustrates how close the parameters are to a tangency bifurcation between $W^u(q)$ and $S_\varepsilon^r$ (dashed cyan); the Hopf $H$ (solid blue), folded saddle-node of type II FSN II (dashed red), and $\delta = 0$ (dashed black) curves are shown as well; see also Figure 16. The slow manifolds $S_\varepsilon^a$ and $S_\varepsilon^r$ shown in panel (c) guide the MMO toward the equilibrium $q \approx (0.951, 0.951, 0.951)$, after which $W^u(q)$ organizes the SAOs. The high compression and twisting of $S_\varepsilon^r$ near $W^u(q)$ is highlighted in panel (d).*
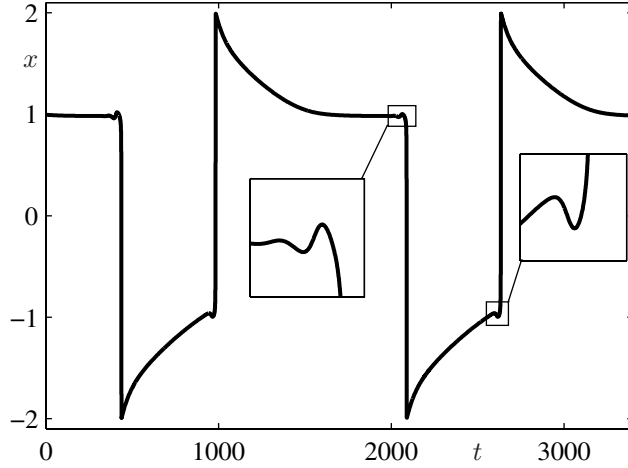
**Fig. 22** *An MMO periodic orbit of* (4.1) *for* $(\varepsilon_1, \varepsilon_2, \lambda, k) = (0.01, 1, -0.063, -2.1)$ *that exhibits SAOs near the maximum as well as the minimum of the LAO.*

To end this case study, we report the existence of a different type of MMO not found by Koper; it is shown in Figure 22. The MMO has SAOs near both the maximum and the minimum of the LAO. Hence, this MMO passes near folded nodes $n_{\pm}^a$ on both fold curves. The parameter region where this occurs is quite small, so that it is difficult to locate such an MMO using simulation; it is the region in Figure 16 near $k = -2$ that can only be seen in the enlargement in panel (b). We found the MMO periodic orbit in Figure 22 by selecting parameters $k = -2.1$ and $\lambda = -0.063$ in this region and choosing $\varepsilon_1 = 0.01$ rather small; a more detailed study of the range of parameters for which there exist such MMOs with two SAO epochs remains future work.

**5. MMOs in a Reduced Hodgkin–Huxley System.** As the next case study we consider a three-dimensional reduced version of the famous Hodgkin–Huxley equations [105] that describe the generation of action potentials in the squid giant axon; see [118, 198] for the derivation and also [45], where the same example was used. The reduced model only describes the dynamics for voltage $(V)$, the activation of the potassium channels $(n)$, and the inactivation of the sodium channels $(h)$; the activation of the sodium channels $(m)$ is very fast and it reaches its equilibrium state $m = m_\infty(V)$ (almost) instantaneously, which can be justified mathematically by a center-manifold reduction [198]. The evolution of the gates $n$ and $h$ is considered slow, while the evolution of the voltage $V$ is considered fast. To justify this time-scale separation, we nondimensionalize the Hodgkin–Huxley equations by introducing a dimensionless voltage variable $v = V/k_v$ and a dimensionless time $\tau = t/k_t$, where $k_v = 100$ mV is a reference voltage scale and $k_t = 1$ ms is a fast reference time scale; this gives

(5.1)
$$\begin{cases} \varepsilon \dot{v} = f(v, h, n) := \bar{I} - m_\infty^3(v)\, h\, (v - \bar{E}_{\mathrm{Na}}) \\ \qquad\qquad\qquad - \bar{g}_k\, n^4\, (v - \bar{E}_{\mathrm{K}}) - \bar{g}_l\, (v - \bar{E}_{\mathrm{L}}), \\ \dot{h} = g_1(v, h) \; := \dfrac{k_t}{\tau_h} \dfrac{(h_\infty(v) - h)}{t_h(v)}, \\ \dot{n} = g_2(v, n) \; := \dfrac{k_t}{\tau_n} \dfrac{(n_\infty(v) - n)}{t_n(v)}, \end{cases}$$

**Table I**  *Original parameter values of the Hodgkin–Huxley equations* (5.1).

| $g_{\mathrm{Na}}$ | $g_k$ | $g_l$ | $E_{\mathrm{Na}}$ | $E_{\mathrm{K}}$ | $E_{\mathrm{L}}$ | $\tau_h$ | $\tau_n$ | $C$ |
|---|---|---|---|---|---|---|---|---|
| 120.0 | 36.0 | 0.3 | 50.0 | $-77.0$ | $-54.4$ | 1.0 | 1.0 | 1.0 |

with dimensionless parameters $\bar{E}_x = E_x/k_v$, $\bar{g}_x = g_x/g_{\mathrm{Na}}$, with $x \in \{m,\ n,\ h\}$, $\bar{I} = I/(k_v g_{\mathrm{Na}})$, and $\varepsilon = C/(k_t g_{\mathrm{Na}}) =: \tau_v/k_t$. The original Hodgkin–Huxley parameter values are given in Table 1. Thus, $\varepsilon = \frac{1}{120} \approx 0.01 \ll 1$ and system (5.1) represents a singularly perturbed system with $v$ as a fast variable and $(n, h)$ as slow variables. The functions $x_\infty(v)$ and $t_x(v)$, with $x \in \{m,\ n,\ h\}$, describe the (dimensionless) steady-state values and time constants of the gating variables, respectively; they are given by

$$x_\infty(v) = \frac{\alpha_x(v)}{\alpha_x(v) + \beta_x(v)} \quad \text{and} \quad t_x(v) = \frac{1}{\alpha_x(v) + \beta_x(v)},$$

with

$$\alpha_m(v) = \frac{(k_v v + 40)/10}{1 - \exp(-(k_v v + 40)/10)}, \qquad \beta_m(v) = 4\exp(-(k_v v + 65)/18),$$

$$\alpha_h(v) = 0.07\exp(-(k_v v + 65)/20), \qquad \beta_h(v) = \frac{1}{1 + \exp(-(k_v v + 35)/10)},$$

$$\alpha_n(v) = \frac{(k_v v + 55)/100}{1 - \exp(-(k_v v + 55)/10)}, \qquad \beta_n(v) = 0.125\exp(-(k_v v + 65)/80).$$

The original Hodgkin–Huxley equations with scaling parameters $\tau_h = \tau_n = \tau_m = 1$ show no MMOs [105], but if $\tau_h > \tau_{h,e} > 1$ or $\tau_n > \tau_{n,e} > 1$ are beyond certain threshold values, then MMOs are observed [45, 198, 199]. Here, we focus on a specific case with $\tau_h = 6.0$, $\tau_n = 1.0$, and $C = 1.2$ (so that $\varepsilon = 0.01$). We use the applied current $I$ (in units of $\mu$A/cm$^2$) of the original Hodgkin–Huxley equations, that is, the rescaled $\bar{I}$ in (5.1), as the only free parameter. Furthermore, in order to facilitate comparison with other studies, we represent output in terms of the nonrescaled voltage $V = 100\,v$, which is in units of mV.

From a mathematical point of view, the MMOs are generated due to the presence of a (subcritical) singular Hopf bifurcation at $I = I_H \approx 8.359$ and a folded node in the singular limit $\varepsilon = 0$. The critical manifold of (5.1) is defined by

$$n^4(v, h) = \frac{\bar{I} - m_\infty(v)^3\, h\, (v - \bar{E}_{\mathrm{Na}}) - \bar{g}_L\, (v - \bar{E}_l)}{\bar{g}_k\, (v - \bar{E}_k)},$$

which is a cubic-shaped surface $S = S^{a,-} \cup F_- \cup S^r \cup F_+ \cup S^{a,+}$ for physiologically relevant values of $I$. The outer sheets $S^{a,\pm}$ are stable, the middle sheet $S^r$ is unstable, and $F_\pm$ denote fold curves [198]. The desingularized reduced system on this manifold is given by

$$\begin{cases} \dot{v} = \quad \left(\frac{\partial}{\partial h} f\right) g_1 \ + \left(\frac{\partial}{\partial n} f\right) g_2, \\ \dot{h} = -\left(\frac{\partial}{\partial v} f\right) g_1. \end{cases}$$

A phase-plane analysis of the desingularized reduced flow in the physiologically relevant range shows that there exists a folded-node singularity on $F_-$ for $I > I_{FSN} \approx 4.83$. Furthermore, it can be shown that the global return mechanism projects into the funnel region for $I < I_r \approx 15.6$; see [198, 199]. Hence, the folded-node theory predicts the existence of stable MMOs for a range of $I$-values that converges to $I_{FSN} < I < I_r$ in the singular limit as $\varepsilon \to 0$.
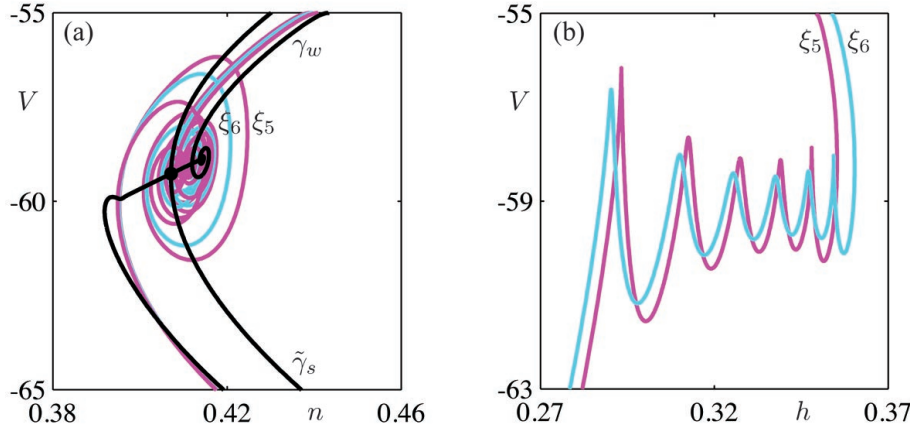
**Fig. 23** *Maximal secondary canard orbits $\xi_5$ and $\xi_6$ of the three-dimensional reduced Hodgkin–Huxley equations (5.1) with $\tau_h = 6.0$, $\tau_n = 1.0$, $C = 1.2$, and $I = 12$. Panel (a) shows the two canard orbits in projection onto the $(n, V)$-plane; also shown are the strong singular canard $\tilde{\gamma}_s$ and the weak primary canard $\gamma_w$. The projection of $\xi_5$ and $\xi_6$ onto the $(h, V)$-plane in panel (b) shows that they make five and six oscillations, respectively.*

Figure 23(a) shows the folded-node singularity for $I = 12$, where it lies approximately at $(v, h, n) = (-0.593, 0.298, 0.407)$, in projection onto the $(n, V)$-plane. The two black curves are the strong singular canard $\tilde{\gamma}_s$ and the primary weak canard $\gamma_w$ that pass through the folded node. The other two curves are maximal secondary canards $\xi_5$ and $\xi_6$ that were found as intersections of extended slow manifolds computed near the folded node; see also section 8 and [45, Figure 6]. Their projections onto the $(h, V)$-plane, which illustrate the oscillating nature of $\xi_5$ and $\xi_6$, are shown in Figure 23(b). Notice that the final oscillations of the primary weak canard $\gamma_w$ in Figure 23(a) show the distinct characteristics of saddle-focus-induced SAOs. Indeed, a saddle-focus equilibrium $q \approx (-0.589, 0.379, 0.414)$ exists relatively close to the folded node, due to the singular Hopf bifurcation at $I_H \approx 8.359$. Decreasing $I$ from $I = 12$ toward $I = I_H$ causes $q$ to move closer to the folded node and the mix of folded-node-induced SAOs and saddle-focus-induced SAOs will be more pronounced; compare with Figure 21(c).

The equilibrium $q$ for $I = 12$ persists when $I$ is varied. A partial bifurcation diagram is shown in Figure 24(a), where we plot the maximum of $V$ versus $I$. Similar to the analysis in [45], a unique equilibrium exists for all $I$ and it is stable for $I < I_H$ and, approximately, $I > 270.772$. The (singular) Hopf bifurcation (labeled $H$) at $I_H$ gives rise to a family of saddle-type periodic orbits. This family of periodic orbits undergoes three fold bifurcations ($SL$) at $I \approx 6.839$, $I \approx 27.417$, and $I = I_{SL} \approx 14.860$, after which both nontrivial Floquet multipliers are less than 1 in modulus and the associated stable periodic orbits correspond to what is known in the field as tonic spiking. Figure 24(a) shows that the first $SL$ is quickly followed by a period-doubling bifurcation ($PD$) at $I \approx 7.651$, where one of the Floquet multipliers, which are both unstable after this first $SL$, passes through $-1$. Hence, the periodic orbits after $PD$ are nonorientable and of saddle type. Note that a second $PD$ (not shown in Figure 24(a)) must take place before the second $SL$.

MMOs exist as isolated families of periodic orbits for a range of $I$; Figure 24(a) shows eleven of these isolas colored in alternating light and dark blue. All periodic
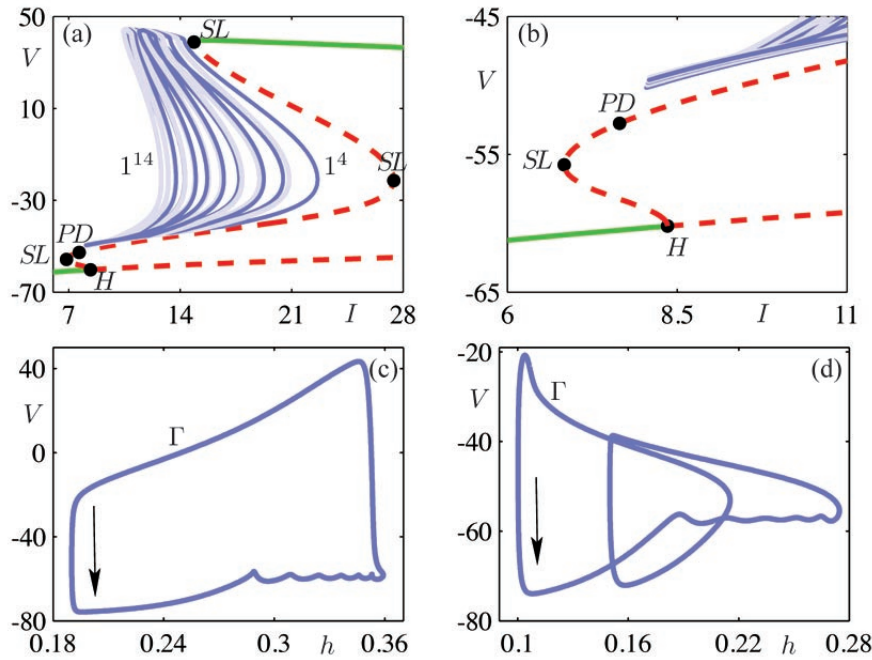
**Fig. 24** *MMO periodic orbits of the three-dimensional reduced Hodgkin–Huxley equations* (5.1) *with* $\tau_h = 6.0$, $\tau_n = 1.0$, *and* $C = 1.2$. *Panel* (a) *shows a bifurcation diagram where the maximal V-value is plotted versus the applied current I. Isolas of MMO periodic orbits exist over a range of I bounded by a period-doubling bifurcation* PD *and a saddle-node of limit cycle bifurcation* SL. *The isolas are colored in alternating light and dark blue. Panel* (b) *shows an enlargement near the Hopf bifurcation. All isolas shown have a fold bifurcation for* $I_{SL} \approx 8.087$. *The periodic orbit* $\Gamma$ *shown in panel* (c) *is the stable MMO for* $I = 12$; *panel* (d) *shows* $\Gamma$ *when it has a maximal V-value of* $-20$ mV.

orbits on a single isola have the same number of oscillations. Each isola contains a short plateau with large maximal $V$ near $V = 40$ mV where the associated MMOs are stable and have signatures $1^s$. For our specific choice $\varepsilon = 0.01$, we found that the stable MMO interval appears to be bounded by $I_H$ on the left and by $I_{SL}$ on the right, that is, $8.359 < I < 14.860$. Recall that the theory based on the singular limit as $\varepsilon \to 0$ predicts the existence of stable MMO periodic orbits with signatures $1^s$ for $4.83 \approx I_{FSN} < I < I_r \approx 15.6$; the match is surprisingly good, even though $\varepsilon$ is relatively large. As $I \downarrow I_H$, the number $s$ in the stable $1^s$ MMO signatures approaches infinity, since a homoclinic orbit through the Hopf singularity is formed; see also [45]. Furthermore, there exist stable MMO signatures with more complicated signatures $1^{s_1} 1^{s_2} \cdots$; see [199]. The MMO periodic orbits go through several bifurcations along the isolas (mostly period-doubling and/or saddle-node of limit cycle bifurcations); compare also Figure 19 for the Koper model in section 4. The maximal $V$-value indicates the amplitude of the largest of the oscillations of the respective MMO periodic orbit. Note the folded structure of the isolas for $V = V_{F_+} \approx -20$ mV, which is approximately the repolarization threshold value for action potentials. This value also corresponds to the $V$-value of the upper fold curve $F_+$, at which a trajectory jumps back. For MMOs on a plateau, the LAOs correspond to a full action potential, while the $s$ SAOs that follow are subthreshold oscillations.

Figure 24(b) shows an enlargement of how the isolas of MMO periodic orbits accumulate near the Hopf bifurcation, which is the region where theory predicts a signature $1^s$, that is, an MMO with one large excursion and $s$ SAOs. This is organized by how the global return mechanism projects onto the critical manifold $S$ as $I$ varies. If the return projects onto a secondary canard, then part of the periodic orbit follows the secondary canards onto the unstable branch $S_{r,\varepsilon}$ of the slow manifold. However, only canard periodic orbits that reach the region of the upper fold curve $F_+$ are maximal secondary canards. Hence, the corresponding family of secondary canards can be split into two groups: we call the secondary canards with maximum $V < V_{F_+}$ *jump-back* canards and those with maximum $V > V_{F_+}$ *jump-away* canards. This is an important distinction in this application, because while the jump-away canards will create action potentials, the jump-back canards will not.

We illustrate the canards along one of the isolas shown in Figures 24(a) and (b). The stable MMO periodic orbit $\Gamma$ that exists on the plateau for $I = 12$ is shown in Figure 24(c); its signature is $1^6$ and it lies on the isola that corresponds to periodic orbits with a total of seven oscillations. Note that the large excursion of $\Gamma$ is above threshold. The six SAOs of $\Gamma$ are due to the fact that the global return lands on the rotational sector bounded by the maximal secondary canards $\xi_5$ and $\xi_6$ for $I = 12$ (not shown); compare Figure 23(b). When the periodic orbit $\Gamma$ is continued in the direction of increasing $I$, the maximal $V$-value decreases and the LAO changes from an action potential to a subthreshold oscillation. Figure 24(d) shows $\Gamma$ (which is now unstable) when its maximal $V$-value is approximately $-20$ mV. Observe that $\Gamma$ still has a total of seven oscillations, but now two of them have a fast segment. These fast segments are jump-back canards. More precisely, the periodic orbit $\Gamma$ consists of a segment of a jump-back canard of the $\xi_6$ canard family that connects to a segment of a jump-back canard of the strong canard family, which in turn connects to the former segment, hence, closing the loop. One could classify $\Gamma$ in Figure 24(d) as an MMO with signature $2^5$, because only five of its oscillations have really small amplitude due to the passage near the folded node, while there are two clearly distinguishable larger oscillations with fast segments due to jump-back canards. However, none of these larger canard oscillations of $\Gamma$ results in a full action potential, meaning that all oscillations are classified as SAOs in this application context.

Figure 25 illustrates the characteristics of the periodic orbits along the lower parts of the isolas in Figure 24(a), where they are very close to the branch of saddle periodic orbits bifurcating from the Hopf bifurcation. More specifically, Figure 25(a) shows a "waterfall diagram" representation of the time series of 90 periodic orbits along the lower part, for $I \leq 12$, of the isola along which one finds a total of ten oscillations. This part of the branch is shown in Figure 25(b). The fold point for this isola is at $I = I_{SL} \approx 8.087$, and the associated periodic orbit is drawn in boldface in Figure 25(a). The periodic orbits on the part of the branch for $I_{SL} \leq I \leq I_H$ are highlighted in blue. The periodic orbits along this part of the isola are quite different from the MMOs one finds near the plateaux of the isolas; namely, they consist of a mix of SAOs and jump-back canards, ten in total. Figure 25(c) shows the projection of the periodic orbit at the fold onto the $(n, V)$-plane; also shown is the coexisting small periodic orbit that lies on the branch emanating from the Hopf bifurcation. This figure suggests that the periodic orbit at the fold is approaching a homoclinic cycle of the small periodic orbit.

**6. MMOs in Olsen's Four-Dimensional Model of the PO Reaction.** Many applications do not lead to models that have a clear split into slow and fast time scales.
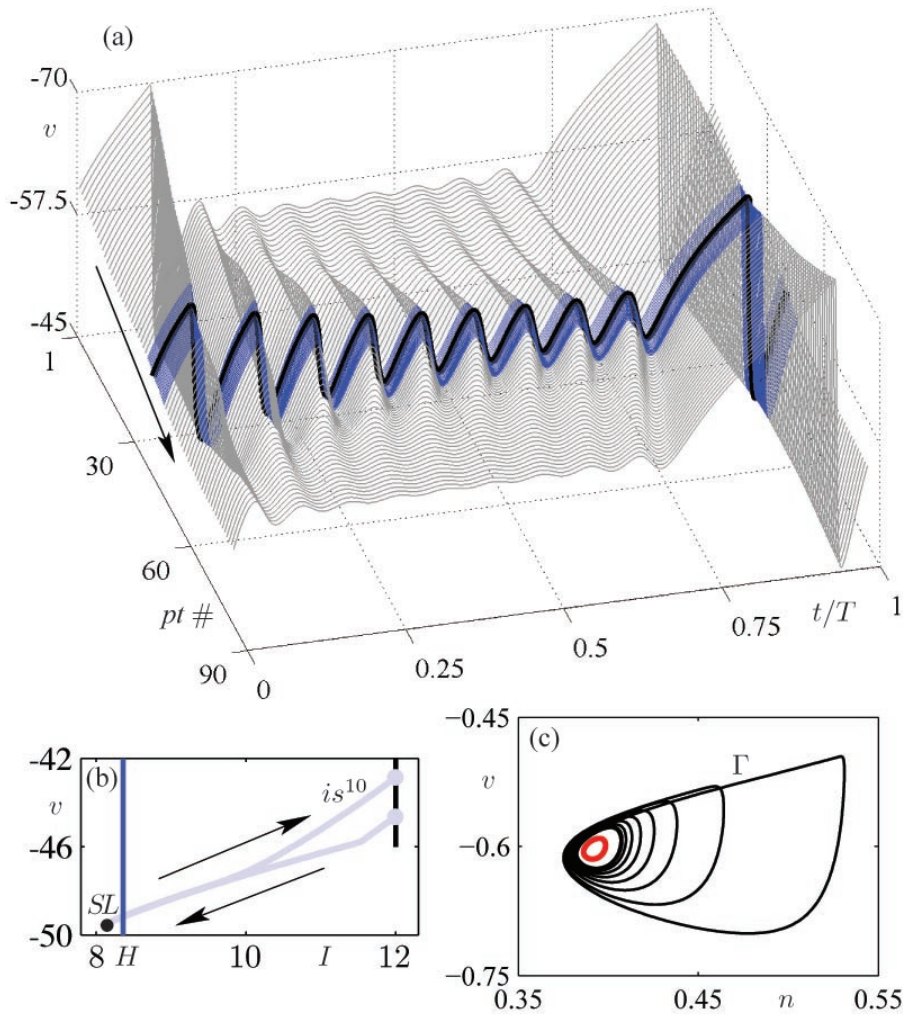
**Fig. 25** *Continuation of a family of periodic orbits that consist of ten oscillations. The continuation starts and ends at $I = 12$ with a fold at $I \approx 8.087$. Panel (a) shows a three-dimensional "waterfall diagram" visualization of the time series of $V$ for 90 computed periodic orbits along this part of the isola; the boldface periodic orbit lies at the fold point. The orbits in blue correspond to the part of isola in between the fold point and the $I$-value that corresponds to the Hopf bifurcation, that is, $I_H \approx 8.359$. Panel (b) shows the maximal $V$-value along the branch in the $(I, V)$-plane, where the arrows indicate the direction of the continuation. Panel (c) shows the periodic orbit at the fold together with a coexisting small periodic orbit in projection onto the $(n, v)$-plane.*

Often some assumptions to that extent can be made, but most variables will be slow in certain regions of phase space and fast in others. The following case study illustrates how the geometrical ideas from slow-fast systems can be used in such a context. We study a four-dimensional model of the peroxidase-oxidase (PO) biochemical reaction that was introduced by Olsen and collaborators [37, 173]; see also [44], where this same example was used. The Olsen model describes dynamics of the concentrations of two substrates ($O_2$ and $NADH$) and two free radicals, denoted $A$, $B$, $X$, and $Y$,

**Table 2**   *Parameter values used in the four-dimensional Olsen model* (6.1).

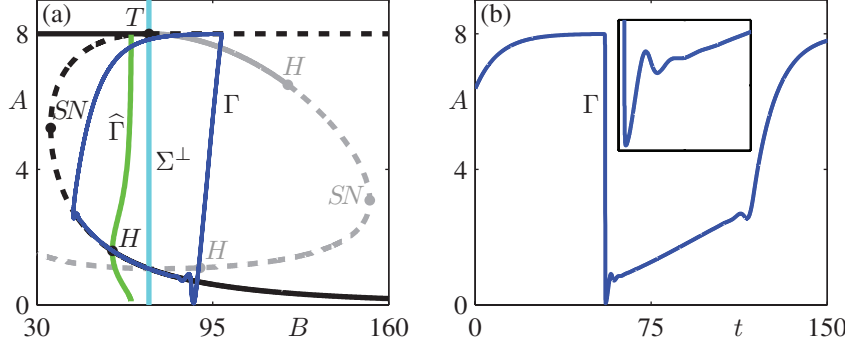| $k_1$ | $k_2$ | $k_3$ | $k_4$ | $k_5$ | $k_6$ | $k_7$ | $k_{-7}$ | $k_8$ | $\alpha$ |
|-------|-------|-------|-------|-------|-------|-------|----------|-------|----------|
| 0.28  | 250   | 0.035 | 20    | 5.35  | 0     | 0.8   | 0.1      | 0.825 | 1        |



**Fig. 26**   *The stable MMO periodic orbit $\Gamma$ of the Olsen model* (6.1) *with parameters as in Table 2. Panel* (a) *shows $\Gamma$ (blue) projected onto the $(A, B)$-plane and superimposed on the bifurcation diagram of* (6.1) *with $\alpha = 0$; solid (dashed) black and gray curves are stable (unstable) equilibria, where the gray color indicates that $X$ or $Y$ are negative, and $SN$, $H$, and $T$ are saddle-node, Hopf, and transcritical bifurcations, respectively. The family $\widehat{\Gamma}$ of periodic orbits that emanates from $H$ is represented by its maxima and minima in $A$ (green curve); the line $\Sigma^\perp$ (cyan) indicates where the $(A, B)$-plane changes from attracting to repelling. Panel* (b) *shows the time series of the variable $A$ along $\Gamma$. The inset panel shows a blow-up of the region where SAOs undergo a slow decay.*

respectively; it is given by the differential equations

$$
(6.1) \quad
\begin{cases}
A' = -k_3 ABY + k_7 - k_{-7}A, \\
B' = \alpha(-k_3 ABY - k_1 BX + k_8), \\
X' = k_1 BX - 2k_2 X^2 + 3k_3 ABY - k_4 X + k_6, \\
Y' = -k_3 ABY + 2k_2 X^2 - k_5 Y.
\end{cases}
$$

Note that $\alpha$ is an artificial time-scale parameter that we introduced for the purpose of this case study; $\alpha = 1$ in [37, 173]. The other parameters are reaction rates and we chose their values as given in Table 2, such that the periodic orbits that exist for these parameter values are representative for the Olsen model (6.1). We focus our study on a stable MMO periodic orbit, denoted $\Gamma$; its time series of the variable $A$ is shown in Figure 26(b). We observe that $\Gamma$ has signature $1^s$, and we estimate that $s$ is about 15. Below, we show that the SAOs of this example occur during passage through a dynamic Hopf bifurcation, and we analyze the global return mechanism of this trajectory.

**6.1. Bifurcations of the Fast Subsystem.** There is no clear split between the different time scales in the Olsen model (6.1), but it is known that $B$ evolves on a slower time scale than the other variables [154]. Hence, it makes sense to consider the fast subsystem obtained by setting $\alpha = 0$, that is, $B' = 0$ and $B$ acts as a parameter in (6.1). The bifurcation diagram is shown in projection onto the $(A, B)$-plane in Figure 26(a), which is invariant because $k_6 = 0$; see Table 2. There are two branches

of equilibria that intersect at a transcritical bifurcation $T$ for $B = k_4/k_1 \approx 71.426$; solid lines indicate stable and dashed lines unstable equilibria. The equilibria that are colored black in Figure 26(a) are physically relevant because they have nonnegative values of $X$ and $Y$; for gray equilibria, on the other hand, $X$ or $Y$ is negative. One branch is the black horizontal line at $A = 8$; it lies in the $(A, B)$-plane (where $X = Y = 0$), which is invariant since $k_6 = 0$. Equilibria along this branch are stable for $B < k_4/k_1$. A second branch intersects the horizontal branch and the $(A, B)$-plane at the point $T$; only the black part of this second branch with positive $X$ and $Y$ is physically relevant; it consists near $T$ of saddles with one unstable and two stable real eigenvalues. Two further bifurcations along this physically relevant branch change the stability of the equilibria; there is a saddle-node bifurcation $SN$ at $B = B_{SN} \approx 35.144$ and a subcritical Hopf bifurcation $H$ at $B = B_H \approx 57.949$. The emanating branch of saddle periodic orbits (green) is labeled $\widehat{\Gamma}$, for which only minimal and maximal values of $A$ are shown. The hyperplane $\Sigma^{\perp} = \{(A, B, X, Y) \,|\, B = k_4/k_1\}$ marks where the linear contraction normal to the $(A, B)$-plane is zero; note that $T \in \Sigma^{\perp}$. Overlaid on this bifurcation diagram is the MMO periodic orbit $\Gamma$ of (6.1) (with $\alpha = 1$), and we can now see how $\Gamma$ is composed of a segment of SAOs, generated by passage through a dynamic Hopf bifurcation, and a global return: starting from the minimum of $\Gamma$, the trajectory spirals in and out of a vortex structure due to the presence of the family of equilibria of the fast subsystem with a pair of complex conjugate eigenvalues that cross the imaginary axis. The presence of the Hopf bifurcation in the fast subsystem explains the observed slow decay and increase in amplitude of the SAOs of the attractor $\Gamma$ of the full system. The reinjection back to a neighborhood of the attracting branch is mediated by an increase in $A$, which triggers a slow increase in $B$, as the trajectory closely follows the invariant $(A, B)$-plane toward the curve of stable equilibria with $A = 8$. As soon as $B > k_4/k_1$, that is, the trajectory crosses $\Sigma^{\perp}$, the $(A, B)$-plane is unstable and the trajectory begins to move away from it. Finally, the sharp decay in $A$ appears to be a fast segment that brings the trajectory back to the entrance of the dynamic Hopf bifurcation; compare also with the time series of the $A$-variable along $\Gamma$ in Figure 26(b). The rapid decrease in amplitude of the SAOs is an indication that $\Gamma$ is in an intermediate regime between the tourbillon and delayed Hopf bifurcations, but we label it as a tourbillon; see the discussion in section 3.4.

**6.2. Slow Manifolds of the Olsen Model.** The SAOs of $\Gamma$ in Figure 26 terminate abruptly via a mechanism that can be visualized by computing slow manifolds. The shape of these manifolds and the geometry of their interactions in the fast subsystem allow us to unravel the organization of MMOs in the Olsen model (6.1). Consider the curve of saddle equilibria for $B < k_4/k_1$ in Figure 26(a) between the points $SN$ and $T$. Each equilibrium has one positive and two negative eigenvalues and the family of associated two-dimensional stable manifolds acts as a limiting (three-dimensional) repelling slow manifold that organizes the termination of the SAOs. Since this termination still takes place extremely close to the invariant $(A, B)$-plane, we may assume that $X$ is a fast variable in this region. Therefore, we may reduce the dimension by way of a quasi-steady-state assumption (QSSA) [74], where we assume that $X$ has reached its steady-state value

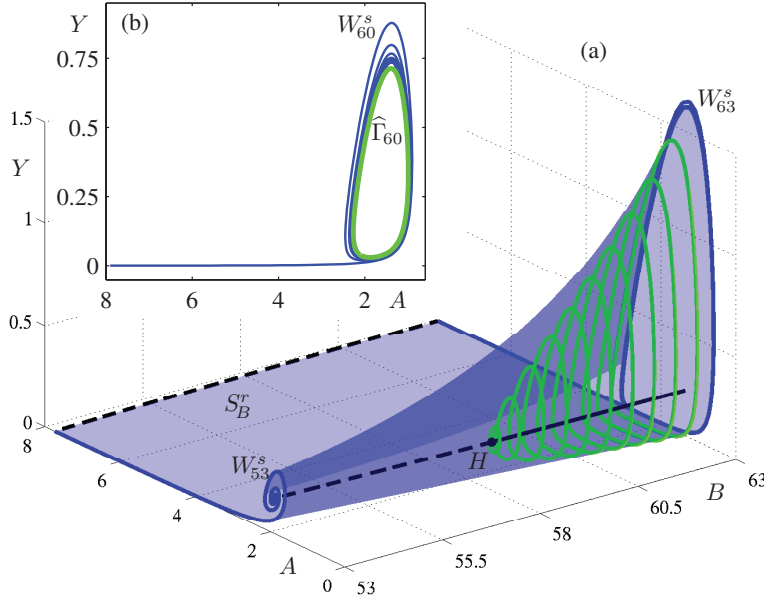(6.2) $$X = \frac{k_1 B - k_4 + \sqrt{(k_1 B - k_4)^2 + 8k_2(3k_3 ABY + k_6)}}{4k_2}.$$

**Fig. 27** *The repelling slow manifold $S_B^r$ (blue) of the fast subsystem of the Olsen model (6.1) ($\alpha = 0$), where $X$ was eliminated via the QSSA (6.2). The manifold $S_B^r$ was computed as the family of one-dimensional stable manifolds $W_B^s$ (one side only) of saddle equilibria (dashed black curve) for $53 \leq B \leq 63$. The branch of equilibria (dashed/solid black curve) in the vicinity of the Hopf bifurcation point (dot) is also shown, along with several unstable periodic orbits (green curves) born at this Hopf bifurcation; the periodic orbits are almost the same as those in Figure 26 for the fast subsystem. Panel (b) shows $W_{60}^s$ and the corresponding unstable periodic orbit $\widehat{\Gamma}_{60}$ for $B = 60$ in the $(A,Y)$-plane. Note that the viewpoint in both panels was chosen such that $A$ increases toward the left; this is also the case in subsequent three-dimensional figures.*

Using the QSSA, we approximate the fast subsystem (6.1) with $\alpha = 0$ as a $B$-dependent family of two-dimensional vector fields in the $(A,Y)$-plane, and the repelling slow manifold is now approximated by a family $S_B^r$ of one-dimensional stable manifolds. Note that the QSSA (6.2) preserves the equilibria of the fast subsystem, and their stability properties change only in the sense that essentially one contracting direction (for $B < k_4/k_1$) is removed. The equilibria on the branch bounded by $SN$ and $T$ are still saddles, but now with only one stable eigenvalue. The equilibria on the branch on the other side of $SN$ are repelling for the planar system if $B$ lies in between $B_{SN}$ and $B_H$, and attracting past $B_H$. We computed $S_B^r$ with AUTO [52] by defining a suitable two-point boundary value problem (BVP); see section 8.2. Figure 27 illustrates how $S_B^r$ rolls up (in backward time) around the lower equilibrium branch for $B_{SN} \leq B \leq B_H$ and around the family of unstable periodic orbits for $B \geq B_H$ until the homoclinic bifurcation for $B \approx 66.480 < k_4/k_1$; to emphasize the $B$-dependent nature, we show this planar dynamics for the fixed value $B = 60$ in panel (b).

The repelling slow manifold $S_B^r$ is only an approximation and it is not an invariant object for the full system (6.1). However, it provides an indication of how an MMO trajectory is trapped by an actual repelling slow manifold as it passes through the
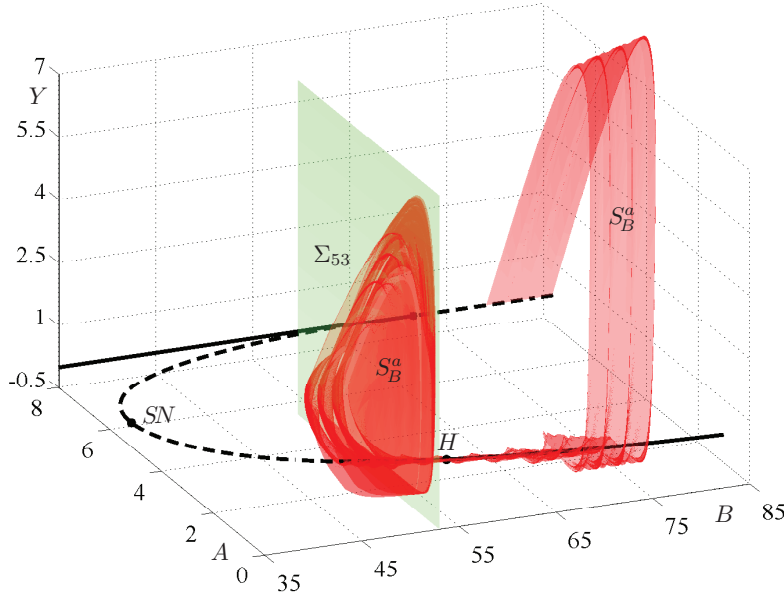
**Fig. 28**  *The attracting slow manifold $S_B^a$ (red) of the full Olsen model (6.1) ($\alpha = 1$), computed from near the equilibria for $A = 8$ and $B > k_4/k_1$ up to the section $\Sigma_{53} = \{B = 53\}$. The black solid/dashed curves are the physically relevant equilibria of the fast subsystem ($\alpha = 0$).*

tourbillon and indicates how the trajectory flows toward the curve of saddle equilibria. By combining this approximation of a repelling slow manifold with an approximation $S_B^a$ of the attracting slow manifold that guides trajectories back to the entrance of the tourbillon, we can visualize the mechanism that organizes the SAOs.

To find $S_B^a$, we consider the curve $L$ of saddle equilibria with $A = 8$ and $B > k_4/k_1$ (past $T$); see Figure 26(a). These equilibria have one-dimensional unstable manifolds in $(A, X, Y)$-space, that is, in the full fast subsystem without the QSSA (6.2). The $B$-dependent family $W^u(L)$ of unstable manifolds is a two-dimensional surface that makes a large excursion before spiraling toward the attracting equilibrium branch that lies just above the invariant $(A, B)$-plane. We define the attracting slow manifold $S_B^a$ in this setting as the equivalent of $W^u(L)$ when $B$ is not fixed but allowed to vary. In particular, with this definition $S_B^a$ enters a neighborhood of $H$ and interacts with the repelling slow manifold $S_B^r$ that only exists for $B < k_4/k_1$. We compute the two-dimensional manifold $S_B^a$ with AUTO [52] by using a BVP setup as in section 8; specifically, we require that one endpoint of the computed orbit segments lies along a line $L^a$ very close to the curve $L$ of equilibria and in the linear approximation to $W^u(L)$; see [44] for more details on how this computation can be performed. Figure 28 illustrates how $S_B^a$ provides a global return mechanism from near $L_a$ via a large excursion and then guides trajectories through the tourbillon.

Figure 29 illustrates how the interaction of $S_B^a$ and $S_B^r$ determines the behavior in the tourbillon regime. The two surfaces are shown in $(B, A, Y)$-space in panel (a). Recall that $S_B^a$ is a two-dimensional surface in $(B, A, X, Y)$-space, and shown is its projection. The manifold $S_B^r$, on the other hand, was computed by assuming the
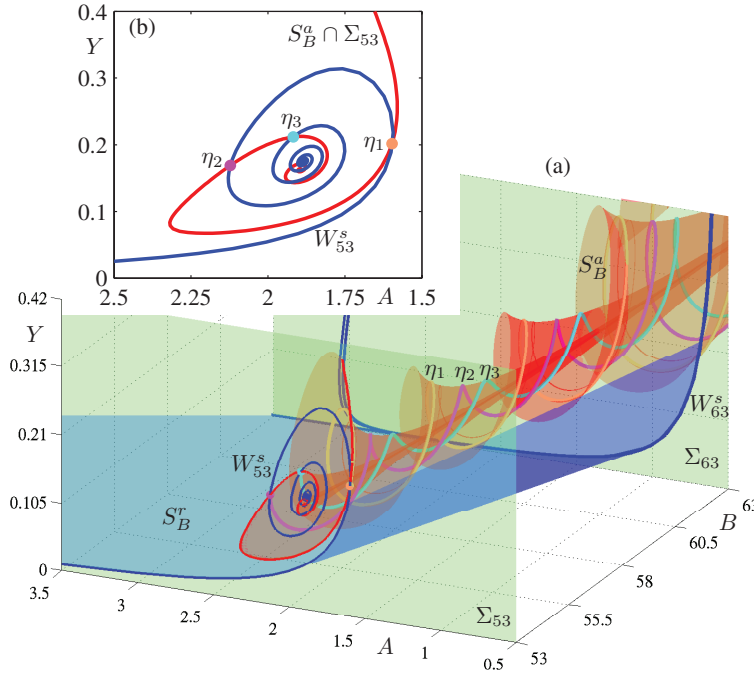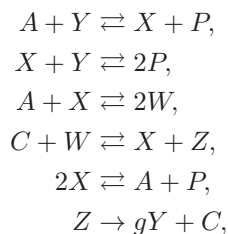
**Fig. 29**  *Approximations of the attracting and repelling slow manifolds of the Olsen model (6.1). Panel (a) shows the surfaces $S_B^a$ (blue) and $S_B^r$ (red) projected into $(A, B, Y)$-space between the sections $\Sigma_{53}$ and $\Sigma_{63}$ (green planes). Also shown are three orbits $\eta_1$ in orange, $\eta_2$ in magenta, and $\eta_3$ in cyan; they lie in the intersection of $S_B^a$ and $S_B^r$. Intersections of $S_B^a$ and $S_B^r$ with $\Sigma_{53}$ are shown in panel (b); the intersections of $\eta_1$, $\eta_2$, and $\eta_3$ with $\Sigma_{53}$ are labeled.*

QSSA (6.2), which is due to an additional strongly attracting direction. Hence, $S_B^r$ is a two-dimensional surface in $(B, A, Y)$-space that corresponds to a three-dimensional surface in $(B, A, X, Y)$-space. Therefore, the intersections of $S_B^a$ and $S_B^r$ with the plane $\Sigma_{53} = \{B = 53\}$ are isolated points, and they are shown in Figure 29(b); note that $S_B^r \cap \Sigma_{53} = W_{53}^s$, while the computation of $S_B^a \cap \Sigma_{53}$ is more involved. The intersection points of these two curves define trajectories that resemble canard orbits near a folded node, because they spiral in the tourbillon region, making an increasing number of turns. The first three intersection points are labeled in Figure 29(b) and their corresponding trajectories $\eta_1$, $\eta_2$, and $\eta_3$ are shown in Figure 29(a). These trajectories $\eta_1$, $\eta_2$, and $\eta_3$ are contained in $S_B^a$, but only their intersection points with $\Sigma_{53}$ lie on $S_B^r$. Indeed, $S_B^r$ is not an actual invariant manifold of (6.1) and only serves as an approximation of the repelling slow manifold. Nevertheless, $S_B^a$ and $S_B^r$ give a qualitative illustration of the nature of SAOs generated by slow passage through the tourbillon. In particular, the intersection curves of $S_B^a$ and $S_B^r$ with $\Sigma_{53}$ provide an approximate location of the sectors of oscillations in this region of phase space.

## 7. The Showalter–Noyes–Bar-Eli Model of MMOs in the BZ Reaction.

The Showalter–Noyes–Bar-Eli model [207] is one of many kinetic models that have been proposed for the Belousov-Zhabotinsky (BZ) reaction. It is a seven-dimensional vector

field derived from a system of reactions

$$A + Y \rightleftarrows X + P,$$
$$X + Y \rightleftarrows 2P,$$
$$A + X \rightleftarrows 2W,$$
$$C + W \rightleftarrows X + Z,$$
$$2X \rightleftarrows A + P,$$
$$Z \rightarrow gY + C,$$

that satisfy the law of mass action, resulting in the equations

$$(7.1) \begin{cases} A' = k_0(A_0 - A) - k_1 AY + k_{-1}PX - k_3 AX + k_{-3}W^2 + k_5 X^2 - k_{-5}AP, \\ C' = k_0(C_0 - C) - k_4 CW + k_{-4}XZ + k_6 Z, \\ P' = -k_0 P + k_1 AY + 2k_2 XY - 2k_{-2}P^2 + k_5 X^2 - k_{-5}AP - k_{-1}PX, \\ W' = -k_0 W + 2k_3 AX - 2k_{-3}W^2 - k_4 CW + k_{-4}XZ, \\ X' = -k_0 X + k_1 AY - k_{-1}PX - k_2 XY + k_{-2}P^2 - k_3 AX + k_{-3}W^2 \\ \qquad + k_4 CW - k_{-4}XZ - 2k_5 X^2 + 2k_{-5}AP, \\ Y' = k_0(Y_0 - Y) - k_1 AY + k_{-1}PX - k_2 XY + k_{-2}P^2 + gk_6 Z, \\ Z' = -k_0 Z + k_4 CW - k_{-4}XZ - k_6 Z, \end{cases}$$

where we use the same letter to identify a chemical species and its concentration. Note that $C' + Z' = k_0(C_0 - C - Z)$, so the hyperplane $C + Z = C_0$ is invariant and attracting. We reduce (7.1) to a six-dimensional vector field on this hyperplane by setting $C = C_0 - Z$ and eliminating the equation for $C'$. The model is "realistic" in the sense that each variable is associated with a definite chemical species. The reaction rates are based upon experimental measurements. As is typical with chemical reactions, the concentrations of intermediate species differ from each other by many orders of magnitude. Nevertheless, some intermediate species that have very low concentrations are still dynamically important. The variable $Y$ represents concentration of bromide, which is often measured in experiments to monitor the state of the system. The variable $A$ in the model represents the concentration of bromate. This chemical has much larger concentrations than the other species, but the chemically relevant quantity is its variation, which is of order comparable to the variations of other concentrations. See Showalter, Noyes, and Bar-Eli [207] for more details about the chemistry. In previous studies of this model, Barkley [16] was unable to clearly identify a dynamical explanation of the MMOs it exhibits.

We study this system for a single set of parameters where Showalter, Noyes, and Bar-Eli observed an MMO, specifically,

$$(7.2) \begin{array}{llll} k_1 = 0.084 & (\text{Ms})^{-1}, & k_{-1} = 1 \times 10^4 & (\text{Ms})^{-1}, \\ k_2 = 4 \times 10^8 & (\text{Ms})^{-1}, & k_{-2} = 5 \times 10^{-5} & (\text{Ms})^{-1}, \\ k_3 = 2 \times 10^3 & (\text{Ms})^{-1}, & k_{-3} = 2 \times 10^7 & (\text{Ms})^{-1}, \\ k_4 = 1.3 \times 10^5 & (\text{Ms})^{-1}, & k_{-4} = 2.4 \times 10^7 & (\text{Ms})^{-1}, \\ k_5 = 4.0 \times 10^7 & (\text{Ms})^{-1}, & k_{-5} = 4.0 \times 10^{-11} & (\text{Ms})^{-1}, \\ k_6 = 0.65 & (\text{Ms})^{-1}, & k_0 = 7.97 \times 10^{-3} & \text{s}^{-1}, \\ A_0 = 0.14 & \text{M}, & C_0 = 1.25 \times 10^{-4} & \text{M}, \\ Y_0 = 1.51 \times 10^{-6} & \text{M}, & g = 0.462. \end{array}$$
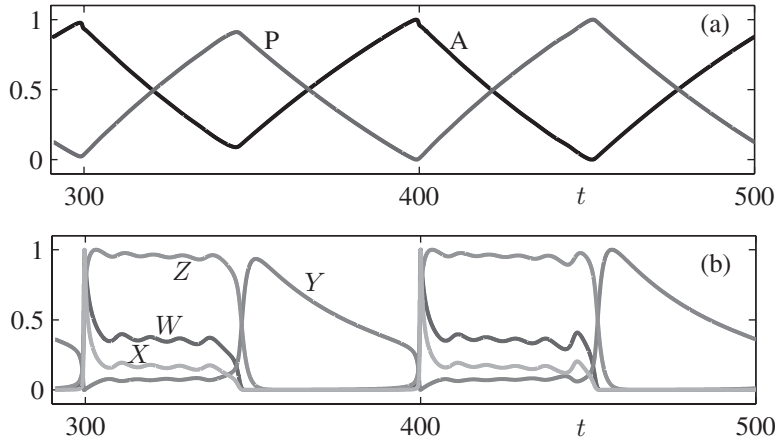
**Fig. 30**  *Time series of an MMO periodic orbit for* (7.1), *with parameters given in* (7.2). *The time series of each variable is scaled to the interval* $[0,1]$ *and the trajectory is plotted over one period. Panel* (a) *shows the slow variables A (black) and P (gray), and panel* (b) *the fast variables W (black), X (gray), Y (black), and Z (gray).*

**Table 3**  *Minimum and maximum ranges of variation of each coordinate in Figure* 30.

| $A$ | $P$ | $W$ | $X$ | $Y$ | $Z$ |
|---|---|---|---|---|---|
| $1.39856 \times 10^{-1}$ | $1.83 \times 10^{-4}$ | $1.45 \times 10^{-9}$ | $4.2 \times 10^{-11}$ | $2.39 \times 10^{-8}$ | $3.89 \times 10^{-8}$ |
| $1.39907 \times 10^{-1}$ | $2.80 \times 10^{-4}$ | $1.38 \times 10^{-6}$ | $1.5 \times 10^{-7}$ | $2.28 \times 10^{-6}$ | $6.41 \times 10^{-6}$ |

Note that the system (7.1) and the parameters in (7.2) have dimensional units; throughout, concentrations are measured in molar (M) and time in seconds (s).

Figure 30 shows time series of the MMO periodic orbit of (7.1) with parameters given by (7.2), plotted over one period $T \approx 209\,\mathrm{s}$. In the time series, each variable is scaled by an affine transformation so that it varies on the interval $[0,1]$. To relate back to the dynamics of (7.2) the minimum and maximum values of each variable prior to rescaling are listed in Table 3. Figure 30 displays the characteristics of an MMO. There are small oscillations that occur while the relative concentration of $Y$ is small and the relative concentration of $Z$ is large. Note from Table 3 that these concentrations are varying by over two orders of magnitude. The periodic orbit makes two circuits and has signature $1^4 1^5$.

There is no explicit slow-fast structure in (7.1). We infer that $(A, P)$ vary slowly relative to $(W, X, Y, Z)$ in an ad-hoc manner from Figure 30 by making two observations. First, the variables $(A, P)$ show a monotone decrease and increase during the times that the variables $(W, X, Y, Z)$ undergo small oscillations. Second, $(A, P)$ do not undergo rapid changes at the beginning or end of the small oscillations as $(W, X, Y, Z)$ do. Therefore, to investigate the mechanisms producing the SAOs in this MMO, we identify the system as a slow-fast system with slow variables $(A, P)$ and fast variables $(W, X, Y, Z)$ as far as the MMO dynamics is concerned. Figure 31(a) projects the MMO periodic orbit $\Gamma$ onto the $(P, Y, Z)$-space. Notice the region of SAOs, which is
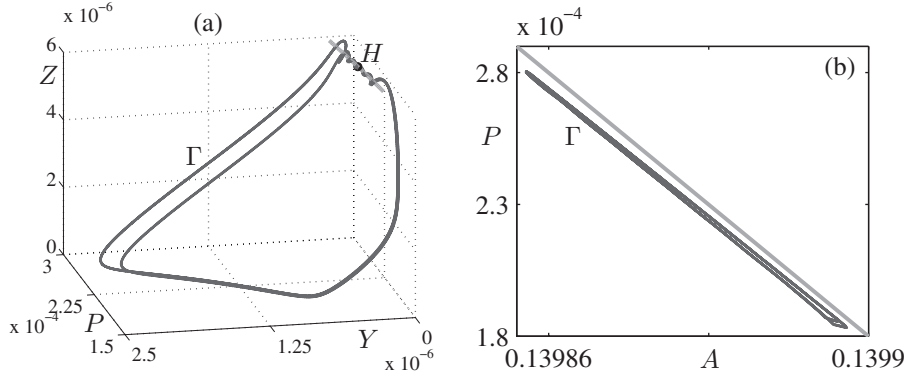
**Fig. 31**  *Panel* (a) *shows the trajectory projected onto the space spanned by the coordinates* $(P, Y, Z)$. *A curve along the critical manifold is plotted as a gray line, and the black dot marks the location of a Hopf bifurcation in the fast subsystem. In panel* (b) *the MMO is projected onto the* $(A, P)$-*plane. The gray line is defined by* $2A + P = 2A_0$ *and the ranges of* $A$ *and* $P$ *are* $[0.13985, 0.13991]$ *and* $[0.00018, 0.0003]$.
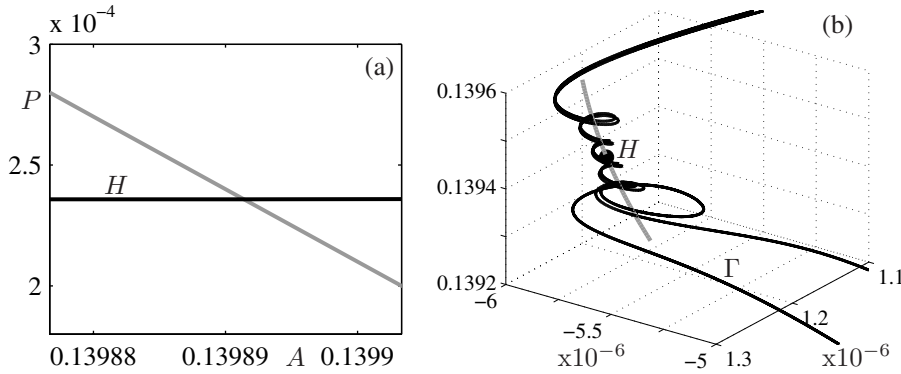


**Fig. 32**  *Panel* (a) *shows the curve of Hopf bifurcations (black line) and the line defined by* $2A + P = 2A_0$ *(gray) in the* $(A, P)$-*plane. Panel* (b) *shows the SAOs projected onto the three-dimensional space spanned by the center manifold of the Hopf bifurcation and the direction of the line* $\{2A + P = 2A_0\}$ *in the* $(A, P)$-*plane. The MMO periodic orbit* $\Gamma$ *visits this region twice and each time spirals around the center manifold of the Hopf bifurcation (gray); the Hopf bifurcation point of the layer system itself is the black dot.*

visited twice. Panel (b) shows $\Gamma$ projected onto the $(A, P)$-plane of slow variables. We observe from this projection that $\Gamma$ lies close to the hyperplane $2A + P = 2A_0$ (gray line), which means that the change of $A$ and $P$ along the MMO periodic orbit is of the same order.

Figure 31(a) suggests that the SAOs of the MMO periodic orbit $\Gamma$ are due to a tourbillon. To ascertain this, we compute the critical manifold near the vicinity of the SAOs with continuation methods using the program MatCont [46]. Figure 32(a) shows the curve of Hopf bifurcations in the fast subsystem in the $(A, P)$-plane of the slow variables together with the curve $2A + P = 2A_0$. The small portion of the Hopf

curve plotted in Figure 32(a) is almost horizontal, so the two curves cross transversally. MatCont also calculates the first Lyapunov coefficient of the Hopf bifurcations along this part of the branch, showing that they are all subcritical. To demonstrate further that the tourbillon associated with the Hopf bifurcation is indeed the basis for SAOs, we project $\Gamma$ onto the three-dimensional space spanned by the two-dimensional center manifold of the Hopf bifurcation in the space of fast variables and the direction defined by $2A + P = 2A_0$. The projection of the center manifold is plotted as a gray curve and the Hopf point of the layer equation is the black dot. The two parts of $\Gamma$ that correspond to SAOs surround the center manifold and have minimal amplitudes close to the Hopf point. This is clear evidence that the MMO found in (7.1) features SAOs that are generated by the tourbillon mechanism of a dynamic Hopf bifurcation, similar to the one observed for the Olsen model in section 6. This example illustrates how the methods described in this paper can be applied effectively to a system of dimension higher than just three or four.

**8. Numerical Methods for Slow-Fast Systems.** This section discusses numerical methods that we used to compute the two-dimensional slow manifolds shown in many of the figures, as well as stable and unstable manifolds of equilibrium points. The slow manifold computations use numerical integration and boundary value methods to compute *orbit segments* that lie along the slow manifolds. An orbit segment is simply a finite piece of a trajectory of the vector field; as such, it has two endpoints and an associated integration time. In the context of computing slow manifolds, each such orbit segment is chosen to have one endpoint on the critical manifold away from its folds, where the critical manifold is a good approximation of the slow manifold one wishes to compute. Indeed, Fenichel's theorem implies that the distance between the critical manifold and the slow manifold is $O(\varepsilon)$, and that trajectories flow from the critical manifold to an attracting or repelling slow manifold at an exponential rate in the appropriate time direction; see Theorem 2.1. Consequently, the computed orbit segments are expected to be as close to the slow manifold as the order of the numerical method allows, except for short $O(\varepsilon)$ segments at one end where there is a fast transition from the critical manifold to the slow manifold in question. For stable or unstable manifolds of equilibria, orbit segments are chosen to lie in the linear eigenspace associated with the stable or unstable eigenvalues, respectively. The computational error associated with this approximation also decays quickly as one moves away from the endpoint; see [43, 131] for analysis of these approximation errors.

A simple and effective method for computing invariant manifolds as families of orbit segments is to use initial value solvers as the basic algorithm with initial conditions chosen on a mesh of points transverse to the flow in the invariant manifold; we call this the "sweeping" method. Despite its simplicity, this sweeping method fails to produce satisfactory results in some cases. In particular, strong convergence or divergence of trajectories toward one another makes the choice of the initial mesh problematic and can produce very nonuniform "coverage" of the desired manifold; see [61, 62]. In multiple-time-scale systems, the fast exponential instability of Fenichel manifolds that are not attracting makes initial value solvers incapable of tracking these manifolds by forward integration. These issues prompt the use of boundary value methods combined with continuation as an alternate strategy for computing invariant manifolds [132, 133]. We have used both strategies in this paper. This section presents more details of the techniques used to compute attracting and repelling slow manifolds of systems with one fast and two slow variables, as well as the continuation of canard orbits when a parameter is varied.

**8.1. Sweeping Invariant Manifolds.** The Fenichel manifolds of systems with a single fast variable are either attracting or repelling. As a result, forward trajectories with initial conditions on the critical manifold will converge quickly to an attracting Fenichel manifold and backward trajectories with initial conditions on the critical manifold will converge quickly to a repelling Fenichel manifold. Thus, one way to compute two-dimensional attracting and repelling Fenichel manifolds of a three-dimensional flow is to apply an initial value solver in the appropriate time direction to a mesh of initial conditions along a curve of the critical manifold transverse to the slow flow. We used this sweeping method to compute $S_\varepsilon^r$ in Figure 11; see also [163] for an early use of this method to compute two-dimensional invariant manifolds and Wechselberger [237] and Guckenheimer and Haiduc [88] for an example involving folded nodes.

When incorporated into a continuation framework, the sweeping method can also be used if the critical manifold is not known in closed form and the mesh of initial conditions cannot be selected beforehand. Continuation methods [51] provide well-established algorithms that augment equation solvers like Newton's method with strategies for choosing new starting points when solving underdetermined systems of equations. More precisely, suppose $F : \mathbb{R}^{m+n} \to \mathbb{R}^m$ is a smooth function given by $m$ equations of $m + n$ variables. The implicit function theorem states that the zeros of $F$ form a smooth $n$-dimensional manifold $M$ near points where the matrix $DF$ of partial derivatives has full rank $m$. Moreover, the theorem gives a formula for the tangent space of $M$. Most continuation methods treat the case $n = 1$, where the set of solutions is a curve; see [104] for the case $n > 1$. In general, the methods are based on a predictor-corrector procedure: given a point on $M$, tangent (or higher-order) information is used to choose a new seed for the solver to find a new point on $M$. The sweeping method described above selects the continuation step size based on equal increments of a specific coordinate or direction, but more sophisticated step size adaptations can be used as well.

We also used a sweeping method to compute the global unstable manifold $W^u(p)$ in Figure 11. The mesh of initial conditions was taken to lie along a ray in the tangent space of $W^u(p)$, with endpoints of the mesh at successive intersections of a trajectory of the linearized system with this ray. The sweeping method works well here, because the selected orbit segments provide adequate "coverage" of $W^u(p)$.

**8.2. Continuation of Orbit Segments with Boundary Value Solvers.** The core algorithms of AUTO [52] are a BVP solver and the numerical continuation of solutions of implicitly defined equations. The BVP solver of AUTO uses a collocation scheme, where solution segments are represented by piecewise polynomials (of a user-specified degree, usually between 3 and 5) that are defined on the mesh intervals of a user-specified mesh. Solving the ODEs at the collocation points gives a large system of equations for the coefficients of the polynomials that is solved by Newton's method. AUTO uses what is known as *pseudo-arclength* continuation to follow or continue solutions of such equations in a chosen parameter, where the step size is adapted automatically; see [51] for details. The combination of a BVP solver and numerical continuation allows us to find and then continue one-parameter families of orbit segments that form (parts of) invariant manifolds of interest. The sweeping method described in the previous section can also be implemented in AUTO [52], so that the initial value problems are solved by collocation. The techniques described in this section impose boundary conditions on both endpoints of the orbit segments, which makes the method more versatile and suitable in a wider context; see also [132]. We describe here how to formulate two-point BVPs in order to compute slow manifolds and associated canard orbits.

We consider two-point BVPs of the scaled form

(8.1)
$$\begin{cases} \dot{\mathbf{u}} = T\mathbf{g}(\mathbf{u}, \lambda), \\ \mathbf{u}(0) \in L, \\ \mathbf{u}(1) \in \Sigma, \end{cases}$$

where $\mathbf{g} : \mathbb{R}^n \times \mathbb{R}^p \to \mathbb{R}^n$ is sufficiently smooth, $T \in \mathbb{R}$, $\lambda \in \mathbb{R}^p$ are parameters, and $L$ and $\Sigma$ are submanifolds of $\mathbb{R}^n$. The parameter $T$ rescales time so that the orbit segments always correspond to trajectories in the time interval $[0, 1]$. Hence, the boundary conditions at the two endpoints always apply to $\mathbf{u}(0)$ and $\mathbf{u}(1)$, and $T$ is the associated (unscaled) total integration time. In order to have a well-posed problem with isolated solutions, the number of boundary conditions should equal the number of equations ($n$, because $\dot{\mathbf{u}} \in \mathbb{R}^n$) plus the number of free parameters (at most $p + 1$ for the parameter $\lambda$ and the total integration time $T$). We are interested in one-parameter families of solutions of (8.1), which means that we allow one fewer boundary condition (or one additional free parameter). Note that the total integration time $T$ is typically unknown and may be viewed as the extra free parameter.

Let us first consider the computation of two-dimensional attracting and repelling slow manifolds $S_\varepsilon^a$ and $S_\varepsilon^r$. To simplify the explanation, we assume that we have a three-dimensional slow-fast system with two slow variables and a folded node. In this context, the parameter $\lambda$ remains fixed, and we obtain a one-parameter family of orbit segments (with unknown total integration times $T$) by imposing a total of three boundary conditions. This means that the dimensions of $L$ and $\Sigma$ in (8.1) sum up to $n = 3$. Our approach is to choose $L$ as a curve (e.g., a straight line) on the critical manifold, which requires two boundary conditions, and $\Sigma$ as a surface (e.g., a plane), which requires one boundary condition, such that the associated one-parameter family of orbit segments covers the desired portion of the slow manifold. For example, in order for $S_\varepsilon^a$ to come into the folded-node region, we let $L$ be a curve on the attracting sheet of the critical manifold transverse to the slow flow and $\Sigma$ be a surface orthogonal to the fold curve $F$ at the folded node. The same approach works for $S_\varepsilon^r$, where we choose $L$ on the repelling sheet of the critical manifold; note that $T < 0$ for such a family of orbit segments. We remark that these choices can also be used with the sweeping method and an initial value solver that detects a "stopping condition" defined by the level set of a function. The slow manifolds can be extended by choosing cross-sections $\Sigma$ orthogonal to $F$ at points that lie beyond the folded node. Figures 6, 20, and 29 give examples of such visualizations; see also [42, 43, 45].

As with all continuation, an important issue is to find a first solution. When continuing solutions of a BVP, explicit solutions may be known from which such a first solution may be constructed; see [43] for an example. However, in general no explicit solution is known and a first solution must be found in a different way. We use a homotopy method to generate an initial orbit segment; the main idea is to continue intermediate orbit segments via two auxiliary BVPs—the first to obtain an orbit segment from a point on the fold curve $F$ to the section, and the second to move the endpoint on $F$ along the critical manifold to a suitable distance from $F$; see [42] for details.

We now illustrate this method with the Koper model (4.1), which was also used for the case study in section 4. We use the parameters $(\varepsilon_1, \varepsilon_2, \lambda, k) = (0.1, 1, 7, -10)$; note that $\lambda > 0$ as in [123], which is symmetrically related to the case with $\lambda = -7$ considered in section 4. As shown in section 4, there is a folded node in this model, which organizes the SAOs in some of the observed MMOs; in original coordinates it

is at

$$(8.2) \qquad \mathbf{p}_{\text{fn}} = \left(-1, \frac{2+\lambda}{k}, \frac{2\lambda+4+k}{k}\right) = (-1, -0.9, -0.8).$$

We compute $S_{\varepsilon_1}^a$ and $S_{\varepsilon_1}^r$ as solutions to the BVPs given by (8.1), where $\mathbf{g}$ is defined by the right-hand side of (4.1). As boundary conditions, we use the same section $\Sigma$ for both $S_{\varepsilon_1}^a$ and $S_{\varepsilon_1}^r$ with respective lines $L = L^a$ and $L = L^r$ as follows:

$$(8.3) \qquad \qquad \Sigma_{\text{fn}} := \{(x, y, z) \in \mathbb{R}^3 \mid z = -0.8\},$$
$$(8.4) \qquad \qquad L^a := S \cap \{x = -1.5\},$$
$$(8.5) \qquad \qquad L^r := S \cap \{x = -0.2\}.$$

Figure 33 shows the result of the computations. We find a first orbit segment on $S_{\varepsilon_1}^a$ using two homotopy steps; this is illustrated in Figure 33(a). Starting from the trivial solution $\mathbf{u} = \{\mathbf{p}_{\text{fn}} \mid 0 \le t \le 1\}$, with total integration time $T = 0$, we continue the family of orbit segments that solves (4.1) subject to $\mathbf{u}(1) \in \Sigma_{\text{fn}}$ and $\mathbf{u}(0) \in F$. We stop the computation, detected by a user-defined function in AUTO, as soon as

$$\mathbf{u}(0) \in \widetilde{\Sigma}^a := \{(x, y, z) \in \mathbb{R}^3 \mid z = -0.76\}.$$

The orbit segment with its endpoint on $F$ in Figure 33(a) is this last computed solution of the family. The second step of the homotopy moves $\mathbf{u}(0) \in S$ away from $F$ (approximately) parallel to $\Sigma$, that is, we next continue the family of orbit segments that solves (4.1) subject to $\mathbf{u}(1) \in \Sigma_{\text{fn}}$ and $\mathbf{u}(0) \in \widetilde{L}^a = S \cap \widetilde{\Sigma}^a$. The continuation stops when $L^a$ is reached, which is again detected by a user-defined function in AUTO. A selection of orbit segments in this family are shown in Figure 33(a) (red curves); only the last orbit segment $\mathbf{u}^a$ (lowest, dark red) lies on $S_{\varepsilon_1}^a$ to good approximation; this is the one from which the manifold computation is started. A similar computation was done to obtain a first orbit segment on $S_{\varepsilon_1}^r$, where we use the intermediate section $\widetilde{\Sigma}^r := \{z = -0.87\}$; this is illustrated in Figure 33(b), where the orbit segment $\mathbf{u}^r$ (cyan) serves as a first solution on $S_{\varepsilon_1}^r$.

Once the first orbit segments $\mathbf{u}^a$ and $\mathbf{u}^r$ have been found we start the continuation of (8.1) with (8.3) and (8.4) for the attracting slow manifold $S_{\varepsilon_1}^a$ and with (8.3) and (8.5) for the repelling slow manifold $S_{\varepsilon_1}^r$. The result is presented in Figure 33(c), and the intersection curves of $S_{\varepsilon_1}^a$ and $S_{\varepsilon_1}^r$ with $\Sigma_{\text{fn}}$ are shown in Figure 33(d). The transverse intersection points of $S_{\varepsilon_1}^a \cap \Sigma_{\text{fn}}$ and $S_{\varepsilon_1}^r \cap \Sigma_{\text{fn}}$ in panel (d) correspond to secondary canard orbits; the three-dimensional view in panel (c) shows three of these, labeled $\xi_1$, $\xi_2$, and $\xi_3$.

**8.3. Finding and Following Canard Orbits.** Maximal canards near a folded node are transverse intersection curves of the two-dimensional attracting and repelling slow manifolds $S_{\varepsilon}^a$ and $S_{\varepsilon}^r$. We briefly discuss here how to detect the canard orbits and subsequently continue them in a system parameter; see also [42, 43, 45]. To represent a maximal canard we must compute $S_{\varepsilon}^a$ and $S_{\varepsilon}^r$ using a common cross-section $\Sigma$ of the fold curve at or near the folded node. The common cross-section allows us to obtain a representation of the canard orbit as the concatenation $\mathbf{u}^c$ of an orbit segment $\mathbf{u}^a \subset S_{\varepsilon}^a$ (with associated total integration time $T^a$) with an orbit segment $\mathbf{u}^r \subset S_{\varepsilon}^r$ (with associated total integration time $T^r$), where $\mathbf{u}^a$ and $\mathbf{u}^r$ are chosen such that $\mathbf{u}^a \cap \Sigma = \mathbf{u}^r \cap \Sigma$. The concatenated orbit $\mathbf{u}^c$ located with this method can be continued in a system parameter without the need to recompute the slow manifolds
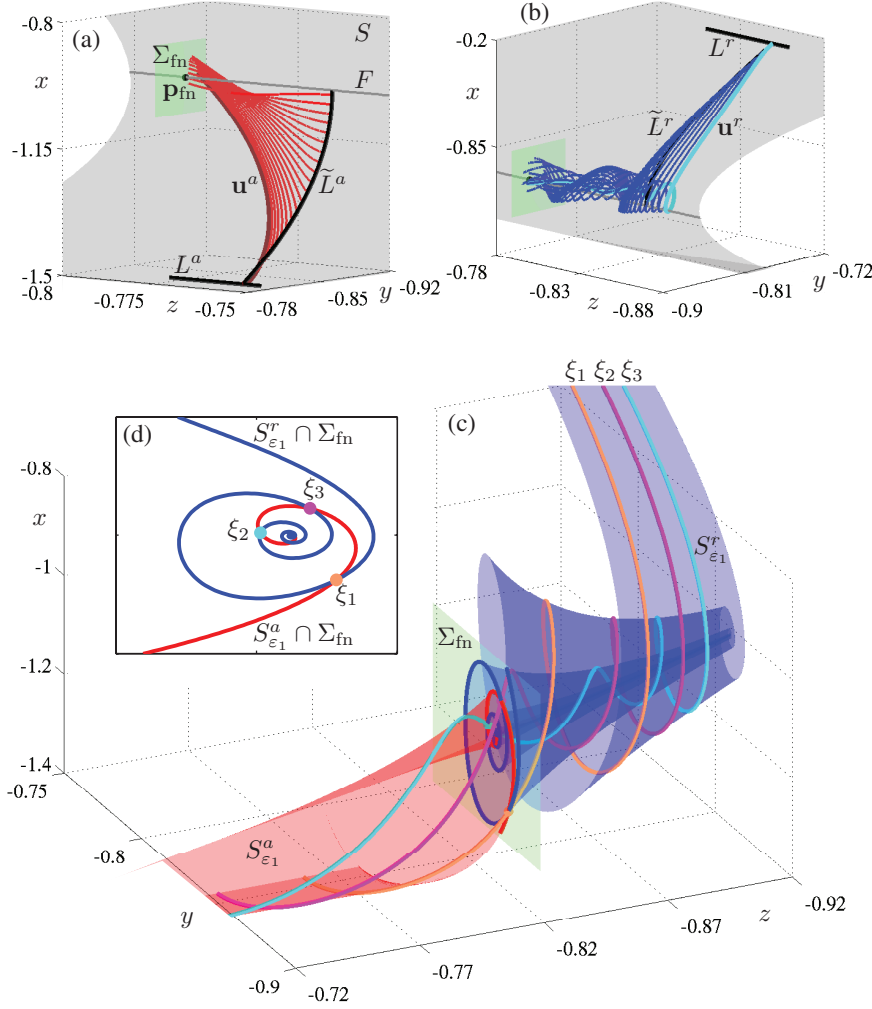
**Fig. 33** *Computation of the slow manifolds $S_{\varepsilon_1}^a$ and $S_{\varepsilon_1}^r$ of the Koper model (4.1) with $(\varepsilon_1, \varepsilon_2, \lambda, k) = (0.1, 1, 7, -10)$. Panel (a) shows a homotopy family of red orbit segments that connect the section $\Sigma_{\mathrm{fn}}$ with the critical manifold $S$ (gray). The first (uppermost) curve in the family was computed by a separate homotopy that found an orbit segment ending along $F$ at some suitable distance from $\mathbf{p}_{\mathrm{fn}}$. The second homotopy step swept out the family of red curves, terminating with the last (lowest, darker red) orbit segment whose endpoint lies on the curve $L^a$. Panel (b) shows a similar homotopy family of orbit segments (blue) connecting $\Sigma_{\mathrm{fn}}$ with the repelling sheet of the critical manifold. The final (rightmost, cyan) orbit segment starts at $L^r$. Panel (c) shows $S_{\varepsilon_1}^a$ and $S_{\varepsilon_1}^r$ together with three secondary canards $\xi_1$, $\xi_2$, and $\xi_3$. Panel (d) shows the intersection curves of $S_{\varepsilon_1}^a$ and $S_{\varepsilon}^r$ in $\Sigma_{\mathrm{fn}}$ that are used to detect canard orbits.*

at each step. Recall that AUTO always scales BVPs to the time interval $[0, 1]$, so we rescale time on $\mathbf{u}^c$ appropriately and set $T = T^a + T^r$ in (8.1). We can then start the continuation (in a system parameter) subject to the boundary conditions

$$(8.6) \qquad\qquad\qquad \mathbf{u}^c(0) \in L^a,$$

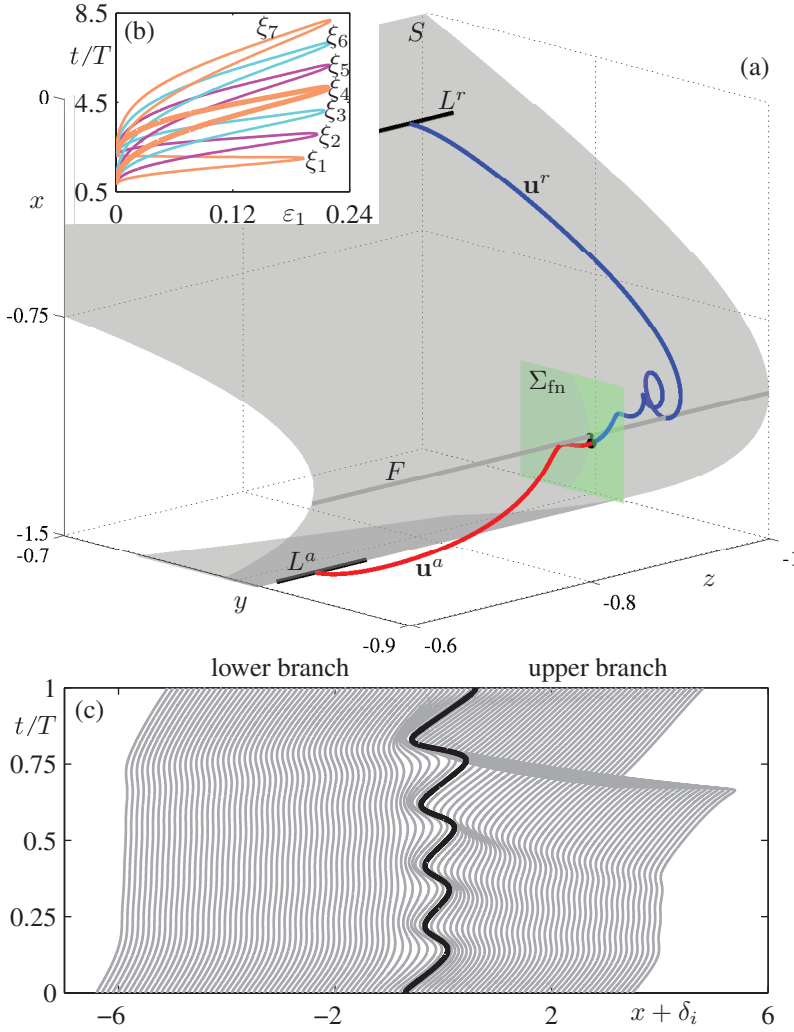$$(8.7) \qquad\qquad\qquad \mathbf{u}^c(1) \in L^r,$$

**Fig. 34** *Continuation of secondary canards of the Koper model* (4.1) *with* $(\varepsilon_2, \lambda, k) = (1, 7, -10)$ *starting from* $\varepsilon_1 = 0.1$. *Panel* (a) *shows the canard orbit* $\xi_4$ *represented by the concatenation* $\mathbf{u}^c$ *of two orbit segments* $\mathbf{u}^a$ *and* $\mathbf{u}^r$ *that match up in* $\Sigma_{\mathrm{fn}}$. *Panel* (b) *shows the continuation of the canard orbits* $\xi_1$–$\xi_7$ *in* $\varepsilon_1$, *plotted as total integration time* $T$ *versus* $\varepsilon_1$. *Panel* (c) *shows a two-dimensional "waterfall diagram" of the time profiles of the fast variable* $x$ *(subject to an offset* $\delta_i$*) of computed orbit segments along the branch* $\xi_4$. *The bold black curve in panel* (c) *is the canard orbit* $\xi_4$ *at the fold point of the (boldfaced) branch in panel* (b).

which determine $\mathbf{u}^c$ as an isolated solution. In fact, such a continuation typically starts already provided that $\mathbf{u}^a \cap \Sigma \approx \mathbf{u}^r \cap \Sigma$; any small gap in $\Sigma$ is forced to close by the first Newton step. These two boundary conditions (8.6) and (8.7) force the orbit segment $\mathbf{u}^c$ to stay very close to the attracting sheet of the critical manifold $S$ until near the fold curve $F$, and then stay close to the repelling sheet of $S$ up to $L^r$.

   Figure 34 illustrates canard continuation with the Koper model (4.1), where we used $\varepsilon_1$ as the second free parameter (together with $T$) and kept $(\varepsilon_2, \lambda, k) = (1, 7, -10)$

fixed. Figure 34(a) shows the two orbit segments $\mathbf{u}^a$ and $\mathbf{u}^r$ with (almost) equal end-points in the section $\Sigma = \Sigma_{\text{fn}}$; they have been detected as a good approximation of the maximal secondary canard orbit $\xi_4$, which is then represented by the concatenated orbit $\mathbf{u}^c$. We continued $\xi_4$, along with six other maximal secondary canards, for increasing and decreasing $\varepsilon_1$; see also Figure 33. Figure 34(b) shows these seven branches, labeled $\xi_1$–$\xi_7$; here, the vertical axis shows the total integration time $T$ because it clearly distinguishes the branches. When $\xi_1$–$\xi_7$ are continued in the direction of increasing $\varepsilon_1$, a fold in $\varepsilon_1$ is detected for each branch; we have already seen this in section 5 and it has also been observed in other systems [45]. Figure 34(c) is a "waterfall diagram" that shows how the maximal secondary canard orbit $\xi_4$ evolves along the branch as $\varepsilon_1$ is varied; specifically, the time profiles of the fast variable $x$ of consecutively computed orbit segments along the branch $\xi_4$ are plotted with a suitable offset $\delta_i$. The orbit segment that corresponds to the fold of $\xi_4$ is highlighted in bold black. Observe that the orbit segments to the left of the fold have four SAOs, whereas past the fold there are only three SAOs followed by a fast segment. Hence the canard orbits past the fold are no longer maximal canards; see also section 5.

**9. Discussion.** We have described several mechanisms in slow-fast systems that produce MMOs, namely, the twisting of slow invariant manifolds near a folded node, oscillations that follow the two-dimensional unstable manifold of a saddle-focus equilibrium near a singular Hopf bifurcation, and the tourbillon mechanism of a dynamic Hopf bifurcation. Geometric singular perturbation theory (GSPT) provides tools to identify the geometry associated with each mechanism, to quantify the MMO signatures, and to describe associated bifurcations. Analysis of the folded-node case is more complete than that of the other cases. Recent work on singular Hopf bifurcation [87] and the transition from singular Hopf to folded nodes [144] provides substantial detail on the second case, but much remains to be discovered about the unfolding of a singular Hopf bifurcation that is relevant to MMOs. Historically, the dynamic Hopf bifurcation was discovered first, and detailed analysis exists for the case of a delayed Hopf bifurcation of the layer equations [169]. Together, these mechanisms constitute a partial framework for classifying MMOs in multiple-time-scale systems that can be further extended. Perhaps the most surprising aspect of the theory we have described is that oscillations can appear from the interaction of fast and slow time scales even when neither of these time scales individually displays oscillations.

We have used four case studies to illustrate theoretical concepts, and they serve as a testbed for the development of numerical methods. The MMOs in the Koper model and the three-dimensional reduction of the Hodgkin–Huxley equations have SAOs that occur on intermediate time scales due to folded nodes and singular Hopf bifurcations. In the folded-node mechanism, three parameters play key roles in determining the geometry of the small oscillations: the ratio $\varepsilon$ of time scales, the eigenvalue ratio $\mu$ of the folded node in the desingularized reduced system, and the distance $\delta$ of global return trajectories from certain invariant manifolds. Intersections of invariant manifolds are prerequisite to global returns that produce MMOs in these examples, and tangencies between these manifolds constitute a new type of bifurcation that is found on the boundaries of parameter regions yielding MMOs. We found fast oscillations of the layer equations in the Olsen and Showalter–Noyes–Bar-Eli models of chemical reactions. Both models exhibit MMOs due to a tourbillon mechanism of a dynamic Hopf bifurcation. These two case studies also illustrate how the theory applies in higher dimensions and how numerical tools can be extended to investigate and identify the mechanisms for generating MMOs in higher-dimensional systems.

One of our goals for this paper is to facilitate fitting dynamical models to data. In the case of MMOs, this task has been less successful than with many other nonlinear dynamical phenomena. On the one hand, MMOs are a complex phenomenon, and on the other hand, numerical studies of models have yielded puzzling and sometimes paradoxical results. The theory that has been developed thus far deals best with circumstances where the SAOs have amplitudes that are far too small to be observed even in numerical simulations, but model studies frequently show MMOs with SAOs that are readily visible. Thus, numerical methods that identify the geometric objects highlighted by the theory are essential for bringing theory, models, and empirical data together. We have reviewed recent advances in computing two-dimensional invariant manifolds and their intersections that are especially important in three-dimensional models. Extension of these methods to higher dimensions is one of the challenges for further advances in this subject.

In the next section we provide a brief review of the MMO literature that includes many references to experimental studies, followed by a short discussion of other mechanisms for MMOs in ODEs and beyond. We conclude this survey with a discussion of some outstanding issues that demand further research.

**9.1. MMO Literature Review.** This section provides an overview, in the form of three tables, of references where examples of MMOs have been studied experimentally or in model systems. We do not claim that this overview is complete; rather, these tables are intended as an entry point into the extensive literature on the subject. Table 4 lists experimental work on MMOs. The majority of these experiments have been carried out for chemical reactions. As suggested in [8], we have subdivided the large

**Table 4** *References for experimental investigations of MMOs.*

| System / Reaction | References |
|---|---|
| Belousov–Zhabotinsky (BZ) reaction | |
|       - Virginia | [85, 106, 107, 108, 204] |
|       - Texas | [157, 158, 159, 196, 197] |
|       - Bordeaux | [8, 9, 185, 195, 231] |
|       - Other groups | [110, 156, 186, 187, 208] |
| Briggs–Rauscher (BR) reaction | [28, 75, 172, 234] |
| peroxidase-oxidase (PO) reaction | [78, 100, 101, 102, 103, 109, 174, 209] |
| HPTCu reaction | [15, 138, 177, 178, 230] |
| Bray–Liebhafsky (BL) reaction | [75, 150, 233] |
| copper and phosphoric acid | [6, 202] |
| indium/thiocyanate (IT) reaction | [126, 127] |
| BSFA-system | [129] |
| p-CuInSe$_2$/H$_2$O$_2$-system | [168, 184] |
| spin-wave experiment | [5] |
| rhythm neural network (PreBötC) | [40] |
| stellate cells | [47, 48, 63] |
| pituitary cells | [228, 232] |
| combustion oscillations | [84] |
| dusty plasmas | [161] |
| semiconductor lasers | [7, 83, 229] |
| CO oxidation | [59, 60, 137] |

**Table 5** *References for realistic mathematical models that exhibit MMOs.*

| Mathematical Model | Dimension | References |
|---|---|---|
| Belousov–Zhabotinsky (BZ) reaction | | |
|       - Field–Koros–Noyes (FKN) | 11 | [72] |
|       - FKN-extended (GTF-model) | 26 | [98] |
|       - Showalter–Noyes–Bar-Eli | 7 | [16, 36, 155, 190, 207] |
|       - (minimal) Oregonator | 3 | [73, 181, 205, 221, 223] |
|       - Model K ("Kyoto") | 3 | [219, 224] |
|       - IUator ("Indiana University") | 4 | [203, 224] |
|       - Geiseler–Föllner Oregonator | 3 | [79, 224] |
|       - FKN-modified | 7 | [188] |
|       - Zhabotinsky–Korzuhkin | 3 | [245] |
| BR-reaction | | |
|       - De Kepper, Epstein; Furrow, Noyes | 11 | [39, 171, 172, 222, 234] |
|       - Kim, Lee, Shin | 8 | [121, 122] |
|       - Vukojević, Sørensen, Hynne | 13 | [234] |
| PO-reaction | | |
|       - Olsen / DOP models | 4 | [4, 37, 44, 151, 153, 154, 174, 210] |
|       - BFSO model, Urbanalator | 10 | [29, 30, 102, 152, 175, 200] |
|       - Yokota–Yamazaki (YY) model | 8 | [67, 201, 243] |
|       - FAB model | 7 | [66, 201] |
|       - Model A, Model C | 9, 10 | [2, 3] |
|       - Model C-HSR | 12 | [109] |
| Plenge model (hydrogen oxidation) | 4 | [11] |
| IT-reaction | 3 | [124, 125, 126, 128] |
| BSFA-system | 4 | [129] |
| p-CuInSe$_2$/H$_2$O$_2$-system | 2, 4 | [168, 184] |
| self-replicating dimer | 3 | [180, 183] |
| autocatalytic SU3 unit | 3 | [220] |
| Hodgkin–Huxley (HH) | 4 | [54, 198, 199] |
| self-coupled HH | 3 | [55] |
| CO oxidation | 3 | [60, 137] |
| self-coupled FitzHugh–Nagumo (FHN) | 3 | [42, 237] |
| FHN, traveling frame | 3 | [91, 93] |
| combustion oscillations | 3 | [77, 84] |
| stellate cells | | |
|       - Acker, Kopell, White (AKW) | 7 | [1, 193, 239] |
|       - reduction of AKW | 3 | [112, 194, 239] |
| pituitary cells | 3, 4 | [170, 211, 215, 232] |
| dopamine neurons | 4 | [140, 160] |
| autocatalator | 3 | [94, 162, 163, 182] |
| LP neuron | 14 | [89] |
| Erisir model | 5 | [64, 65] |
| semiconductor lasers | 3 | [7, 53, 134, 136, 179] |

number of references on the BZ reaction into research groups. Table 5 lists references to mathematical models that were derived or proposed for a particular application that features MMOs; several papers from Table 4 also contain a theoretical model and are, hence, listed again in Table 5. Finally, Table 6 lists several abstract models that are designed to be among the simplest systems that yield MMOs with specified characteristics; the first five rows of the table represent frameworks of folded nodes, folded saddle-nodes, and singular Hopf bifurcation that are presented in this paper.

**Table 6** *References for abstract models exhibiting MMOs.*

| Abstract Model | Dimension | References |
|---|---|---|
| Boissonade and De Kepper; Koper | 2, 3 | [26, 38, 123] |
| Boissonade and De Kepper; Strizhak | 2, 3 | [26, 82, 120] |
| Kawczynski and Strizhak | 3 | [116, 117, 186, 187] |
| folded node toy model | 3 | [31] |
| 3-scale: Krupa, Popović, Kopell | 3 | [139, 140] |
| Hopf-hysteresis normal form | 3 | [16, 188] |
| two coupled oscillators | 4 | [212] |
| Rössler; Gaspard and Nicolis | 3 | [16, 76] |
| Barkley | 4 | [16] |

Chemical reactions feature strongly in Tables 4–6. There have been substantial efforts to develop models, from the law of mass action, that reproduce experimental observations. We remark that detailed models that attempt to capture the full chemistry of a reaction are typically very stiff and contain large numbers of parameters; as a result, it is often difficult to fit the models to experimental data. We hope that the theory and numerical methods reviewed in this paper lead to better fits of models to data. Note that recent interest in MMOs in neuroscience is also reflected in the three tables.

**9.2. Other MMO Mechanisms in ODEs.** Historically, MMOs have also been studied in the context of bifurcations of systems with a single time scale. More specifically, homoclinic or heteroclinic cycles involving one or several invariant objects provide a mechanism for MMOs that does not require an explicit slow-fast structure. The best-known case is that of a homoclinic orbit to a saddle-focus in $\mathbb{R}^3$. A theorem by Shil′nikov [90, 148, 206] proves that (depending on a condition on the eigenvalues of the saddle-focus) there exists one or an infinite number of periodic orbits in a tubular neighborhood of the homoclinic orbit; see also [81]. Each such periodic orbit near this global bifurcation involves one or several large excursions along the homoclinic orbit, as well as small oscillations when the trajectory spirals away from, or back toward, the saddle-focus. This type of oscillation near Shil′nikov bifurcations can be found readily in laser systems: one or several large pulses of the laser power are followed by small damped oscillations near the saddle-focus; see, for example, [7, 53, 83, 134, 136, 179, 229, 241]. The small oscillations are at a characteristic frequency and are due to a periodic exchange of energy between the optical field and the carrier reservoir (electron-hole pairs in the case of a semiconductor laser). Similarly, more complicated heteroclinic cycles may give rise to large excursions followed by small oscillations. A concrete example is a heteroclinic cycle between a saddle equilibrium and a saddle periodic orbit, as can be found, for example, near a saddle-node Hopf bifurcation with global reinjection. Near this global bifurcation one can find large attracting periodic orbits that visit a neighborhood of the equilibrium and also have an arbitrary number of smaller loops around the saddle-periodic orbit; see [130, 135].

While such global bifurcations are generic and require no special properties of the system, they often appear in slow-fast systems, and proving their existence is greatly simplified in this context [164, 213]. A notable example was introduced by Rössler [191, 192] and later illustrated by a model due to Gaspard and Nicolis [76]. Figure 35(a) shows the geometry of this model; it has a classical S-shaped critical manifold $S$ with two fold lines and there exists a stable MMO periodic orbit $\Gamma$ that
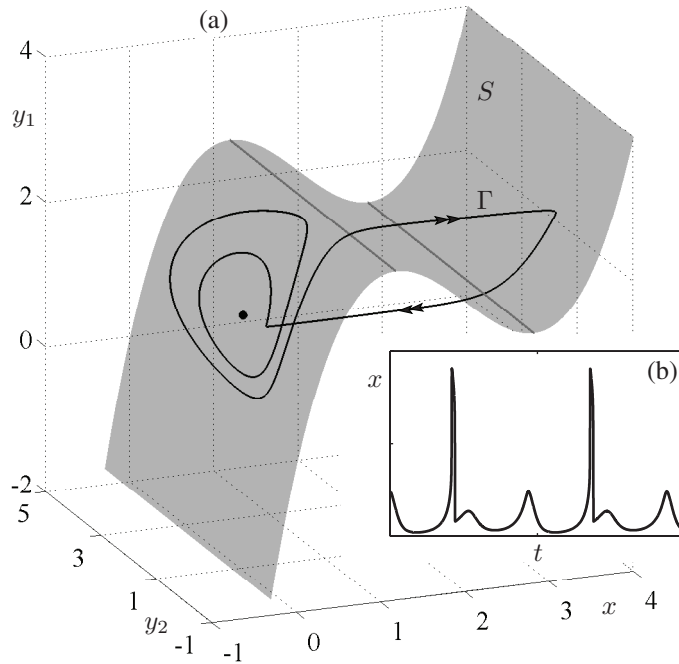
**Fig. 35**   *An MMO periodic orbit $\Gamma$ in the Gaspard–Nicolis–Rössler model [76]. Panel (a) shows $\Gamma$ relative to the S-shaped critical manifold; this illustrates that the SAOs are taking place entirely on the slow manifold. Panel (b) shows the time series of the x-coordinate of $\Gamma$.*

contains two fast segments. Figure 35(b) shows the corresponding time series of one of the coordinates of $\Gamma$ and illustrates that $\Gamma$ has signature $1^2$. The LAOs of $\Gamma$ are formed by the usual relaxation-oscillation mechanism. The phase portrait in Figure 35(a) is near (the simple case of) a Shil′nikov bifurcation; the SAOs occur because, after one fast transition, $\Gamma$ is in the vicinity of a saddle-focus equilibrium, which is an unstable focus of the slow flow. Note that the time series also show that the SAOs happen on the slow time scale. Barkley [16] observed that this mechanism does not account for MMOs in the BZ reaction because there the SAOs also have a fast component. Moreover, this particular mechanism does not seem to occur in other models as commonly as the slow-fast mechanisms presented in section 3. Intuitively this is expected since the global return mechanism has to be special (namely, near a Shil′nikov bifurcation) to provide returns to a small neighborhood of a slow-flow focus. Nevertheless, the Rössler mechanism is of interest historically as one of the first proposed geometric mechanisms for MMOs. It is also another nice example that illustrates the geometric approach of exploiting the slow-fast nature of a system to understand MMOs.

   Subcritical Hopf bifurcation in a system with a single time scale has also been observed to give rise to MMOs. The appearance of these MMOs resembles those associated with Shil′nikov bifurcation. Guckenheimer and Willms [95] analyze this phenomenon, which we briefly sketch here. Consider a three-dimensional system in which an equilibrium $q$ makes the transition from a sink to a saddle-focus via a subcritical Hopf bifurcation. When $q$ is a saddle-focus, it has a real eigenvalue of magnitude $O(1)$ and a pair of complex eigenvalues whose real parts are small and

positive. Trajectories that come close to the stable manifold of $q$ will flow close to $q$ and then slowly spiral away with oscillations of increasing magnitude, similar to those observed near a singular Hopf bifurcation; see Figure 21. MMOs will occur if these spiraling trajectories make a global return to the vicinity of $q$. Global returns for portions of the unstable manifold of $q$ are robust and may exist already at the Hopf bifurcation where the center manifold of $q$ is weakly unstable. In this case, the returns are likely to come close enough to $q$ that they will give rise to long epochs of small, slowly growing oscillations. See Guckenheimer and Willms [95] for a three-dimensional example and Guckenheimer et al. [89] for a high-dimensional example occurring in a neural model. We remark that, although this mechanism for creating MMOs applies to a single-time system, the Hopf bifurcation naturally introduces a slow time scale in the system associated with the real parts of the unstable complex eigenvalues.

The MMOs that we have discussed in this survey have SAOs generated by a local mechanism near a special point of the limiting system. However, SAOs and associated MMOs may also arise in other ways in slow-fast systems. An example of this is that of MMOs with two well-defined separate oscillations that occur when the layer equations have two families of periodic orbits, one large and one small, and fast jumps between them. This scenario is analogous to the phenomenon of bursting, which is common in neural systems. In bursting, oscillations alternate with quiescent epochs (associated with a slow drift along a stable equilibrium of the layer equations) instead of there being oscillations of different amplitudes. Since the seminal work of Rinzel [189], bursting has been viewed as a multiple-time-scale phenomenon. In this context, bursts occur when the layer equations of a model have both equilibria and limit-cycle attractors and the full system makes fast jumps between these features in both directions. Izhikevich [111] compiled an extensive classification of bursting patterns based upon the bifurcations of the layer equations that initiate and terminate the oscillations in a burst. A similar table could be constructed for MMOs, but it would be even larger. Golubitsky, Josiç, and Kaper [80] use a different classification of bursting patterns based on singularity theory, which is more in the spirit of this survey. Section 6 gives a brief taste of the analysis of global mechanisms for transitions between large and small oscillations in MMOs.

**9.3. MMOs Beyond ODEs.** This survey only considers MMOs that arise in slow-fast ODEs, but they have also been found in dynamical systems that are described by stochastic differential equations (SDEs), delay differential equations (DDEs), and partial differential equations (PDEs). The analysis of MMOs in these more involved settings is much less developed than that for ODEs. To give a flavor, we now describe briefly a few recent examples in which a slow-fast structure is an important aspect of the MMOs that have been identified.

**9.3.1. Stochastic MMOs.** Muratov and Vanden-Eijnden [166] study the Van der Pol oscillator with small (additive) noise; they use $\lambda$ as the bifurcation parameter and consider the case $0 < \varepsilon \ll 1$. Their analysis shows an intricate interplay between the noise and the singular perturbation parameter $\epsilon$ and how this depends on $\lambda$. For example, it can be shown that even if the deterministic limit without noise has just a stable fixed point for suitable $\lambda$, the SDE can exhibit relaxation-type oscillations; also, MMOs that are composed of "small canard orbits" and relaxation LAOs can occur. Borowski and Kuske [146] consider a similar stochastic slow-fast equation of FitzHugh–Nagumo type and find MMOs due to noise as well; see also [147]. Closely related is the work by Berglund and Gentz [24, 25], who study spike generation in slow-fast neural models with noise in the framework of SDEs. The common ingredient

in these examples is excitability: while small noise only leads to small irregular oscillations, a sufficiently large noise perturbation can kick the system beyond a threshold that results in a large excursion. There is a noise level when the system is most coherent or regular and, hence, shows well-defined but irregular MMOs. Excitability as a mechanism to generate large pulses as the result of external and/or internal noise has also been observed and studied in several laser systems [56, 134].

Another possible mechanism for noise-induced MMOs was investigated by Yu, Kuske, and Li [244], who consider a system of coupled-oscillator SDEs. If the deterministic limit is at least bistable, then noise can provide a mechanism for sample paths to alternate between the basins of attraction of deterministically stable invariant sets. The simplest way to visualize this idea is to consider two stable limit cycles for an ODE, one with a small and the other with a large amplitude. If the basins of attraction are suitably located, noise can induce repeated transitions between tubular neighborhoods of each cycle. Hence, a typical sample path will then be an irregular MMO.

**9.3.2. MMOs in DDEs.** One can ask what happens when one adds delay terms to a slow-fast system. Sriram and Gopinathan [208] consider the BZ reaction with delay in an experiment. They compare the results with a version of the classical three-dimensional Oregonator model [73, 205] with delay and claim that the delay induces MMOs [208]. This prompts the question of whether DDEs have slow-fast phenomena, such as canards, similar to their ODE counterparts. In principle, this should be expected at least for the case of a finite number of fixed delays, for which the DDE does not feature a continuous spectrum [96]. Indeed a positive answer was recently obtained by Campbell, Stone, and Erneux [32] for a two-dimensional DDE model of high-speed machining. In their system a small delay induces perturbation from a degenerate Hopf bifurcation, which results in a canard explosion as discussed in section 2.2; see also [34] for details of the underlying theory for slow-fast DDEs with small delay.

**9.3.3. MMOs in PDEs.** Given a time-dependent PDE on a domain in $\mathbb{R}^n$, one can look for MMOs in space, time, or a mixture of space and time. Nagumo's equation [167], which models the evolution of an activator $v(x,t)$ and a slow inhibitor $u(x,t)$, is an example that has been studied extensively as an idealized model for propagation of action potentials. Traveling-wave profiles are found via the ansatz $v(x,t) = v(x+\sigma t) = v(\tau)$ and $w(x,t) = w(x+\sigma t) = w(\tau)$ as homoclinic solutions of a three-dimensional ODE with two fast variables and one slow variable [92]; here, $\sigma$ is the wave speed. It has been shown that MMOs exist as solutions of this reduced ODE [93]. More generally, work on evolution equations given by PDEs suggests that oscillatory patterns with alternating amplitudes [35] and slow-fast structures [17] exist in many common models. Hence, the study of this type of MMO for PDEs will benefit from multiple-time-scale methods.

**9.4. MMOs: Bringing Together Theory and Data.** We end with a few additional remarks about outstanding issues concerning MMOs in the context of multiple-time-scale ODE models. We regard the central goal of research on MMOs as comprehensive analysis of empirical data: this opinion shapes our view of the priorities for further research on the subject. The MMO literature reviewed above has only a modest amount of empirical data, but that is sufficient to raise concern about whether we have yet discovered models that capture the essence of the MMOs observed in experiments. We have discussed the amplitudes of SAOs and the sizes of parameter regimes yielding MMOs in this review but have not explored the implications of our

findings for empirical data. We do suggest that these characteristics be used in fitting models to data.

The study of MMOs has its origins in investigations of oscillations in chemical reactions, especially during the 1970s and 1980s. There was interest then in determining whether aperiodic dynamics in these systems are the result of deterministic chaos or noise. With a focus on the BZ reaction, quantitative models for systems with complex dynamics were developed. Nonetheless, these attempts to produce accurate kinetic models for the reactions were only partially successful. The models had multiple time scales, making it difficult to interpret their dynamics in the light of theory existing at that time. The advances that have been made in GSPT since then suggest that a renewed study of these models could make significant progress on problems that were abandoned rather than solved a generation ago. New technologies may also enable experiments that measure the dynamics of these reactions with greater precision than was possible in the 1980s. Then, and now, one of the motivations for studying these reactions is to develop methods for studying the dynamics of biological systems.

The focus of this survey has been on local mechanisms that generate SAOs via the passage near special points that can be found generically in multiple-time-scale system. MMOs arise in the presence of a return mechanism that allows trajectories to pass through the region of SAOs over and over again. We considered here only return mechanisms that bring the trajectory immediately back to the SAO region after one large excursion, which corresponds to a single LAO. However, MMOs may have more general signatures with several LAOs in between epochs of SAOs. There has been little study to date of mechanisms that produce such MMOs with $L > 1$. For some three-dimensional systems with two slow variables and one fast variable with an S-shaped critical manifold, the global returns from a region surrounding SAOs back to itself are very regular and can be approximated by nearly one-dimensional linear maps. This scenario is not expected to produce many complicated signatures with $L > 1$. A similar effect has also been analyzed for a system with three time scales [139, 140], where the only signatures that are found are $2^1$, $2^2$, and $L^1$. These results are also supported by numerical evidence in several other three-dimensional models [123, 126, 182, 198, 199] and in an experiment [6].

More complicated MMO signatures with $L > 1$ have rarely been analyzed in any detail in the current literature. They seem to occur most frequently in higher-dimensional chemical reactions such as the BZ reaction [159, 157, 158, 106], the Briggs–Rauscher reaction [122], and the PO reaction [154, 151]; see also section 7. We discussed one possibility of obtaining $L > 1$ LAOs as part of an MMO: that there are several large oscillations in the fast subsystem before an MMO trajectory reenters the SAO region. As was discussed in section 3.3, this requires there to be two-dimensional fast dynamics in at least some part of phase space. We remark that in systems with two or more fast variables, the presence of MMOs with $L > 1$ is analogous to the oscillations found in bursting systems [111]. Analysis of the mechanisms associated with the initiation and termination of LAOs that follow a family of periodic orbits in the layer equations of slow-fast systems with MMOs has hardly been attempted. For bursting, Terman and Lee [217] is a representative study. More generally, for MMOs in systems with at least two slow and two fast variables, one would expect to find quite a number of different global return mechanisms that may give rise to several LAOs between epochs of SAOs.

Investigations of slow-fast systems with more than two slow variables have just begun. Wechselberger [238] extends the theory of canards to such systems and Harvey et al. [99] use these results to study models of intracellular calcium dynamics.

Much of the analysis of MMOs in models has been based upon numerical studies of bifurcation sequences and the interpretation of these sequences in terms of the iterations of one-dimensional maps. Theoretically, the properties of return maps for the examples of this paper could be decomposed into a composition of two maps, the first describing flow through the small region producing SAOs and the second describing the global returns of trajectories emerging from this region. These maps are quite complicated and deserve further study. They may have discontinuities and gaps where trajectories tend to small attractors in the region with SAOs, and the fate of trajectories following canards is often difficult to compute. More analysis of bifurcation and chaos in one-dimensional approximations of the return maps may help further to characterize the mechanisms underlying MMOs observed in empirical data. An important system in which to complete such an analysis is the Koper model and its extension as a modified normal form for singular Hopf bifurcation with a global return.

One of the highlights of dynamical systems theory has been its success in identifying simple models that capture the essence of behaviors that are found in large classes of systems. Nonetheless, our ability to analyze models as complex as realistic models for chemical reaction kinetics or spiking neurons is limited by the efficacy of our numerical methods. We have demonstrated here how advanced numerical methods for slow-fast systems can be brought to bear for the study of systems of dimension up to four. However, further development of methods to analyze the dynamics of high-dimensional, multiple-time-scale systems is definitely needed. It would be helpful to have better methods to enable a systematic model reduction in regimes with low-dimensional attractors. The analysis of MMOs in more general situations would also be facilitated by numerical methods for computing invariant manifolds and the fast-slow decomposition of trajectories in higher-dimensional systems. In particular, such numerical techniques will be crucial for the study of new types of return mechanisms and, hence, MMOs with more complicated signatures of LAOs and SAOs.

## REFERENCES

[1] C. D. Acker, N. Kopell, and J. A. White, *Synchronization of strongly coupled excitatory neurons: Relating network behaviour to biophysics*, J. Comput. Neurosci., 15 (2003), pp. 71–90.

[2] B. D. Aguda and B. L. Clarke, *Bistability in chemical reaction networks: Theory and application to the peroxidase-oxidase reaction*, J. Chem. Phys., 87 (1987), pp. 3461–3470.

[3] B. D. Aguda and R. Larter, *Periodic-chaotic sequences in a detailed mechanism of the peroxidase-oxidase reaction*, J. Amer. Chem. Soc., 113 (1991), pp. 7913–7916.

[4] B. D. Aguda, R. Larter, and B. L. Clarke, *Dynamic elements of mixed-mode oscillations and chaos in a peroxidase-oxidase network*, J. Chem. Phys., 90 (1989), pp. 4168–4175.

[5] F. M. de Aguiar, S. Rosenblatt, A. Azevedo, and S. M. Rezende, *Observation of mixed-mode oscillations in spin-wave experiments*, J. Appl. Phys., 85 (1999), pp. 5086–5087.

[6] F. N. Albahadily, J. Ringland, and M. Schell, *Mixed-mode oscillations in an electrochemical system. I. A Farey sequence which does not occur on a torus*, J. Chem. Phys., 90 (1989), pp. 813–821.

[7] K. Al-Naimee, F. Marino, M. Ciszak, R. Meucci, and F. T. Arecchi, *Chaotic spiking and incomplete homoclinic scenarios in semiconductor lasers with optoelectric feedback*, New J. Phys., 11 (2009), 073022.

[8] F. Argoul, A. Arneodo, P. Richetti, and J. C. Roux, *From quasiperiodicity to chaos in the Belousov-Zhabotinskii reaction.* I. *Experiment*, J. Chem. Phys., 86 (1987), pp. 3325–3338.

[9] F. Argoul and J. C. Roux, *Quasiperiodicity in chemistry: An experimental path in the neighbourhood of a codimension-two bifurcation*, Phys. Lett. A, 108 (1985), pp. 426–430.

[10] V. I. Arnol′d, ed., *Encyclopedia of Mathematical Sciences: Dynamical Systems* V, Springer-Verlag, Berlin, New York, 1994.

[11] N. Baba and K. Krischer, *Mixed-mode oscillations and cluster patterns in an electrochemical relaxation oscillator under galvanostatic control*, Chaos, 18 (2008), 015103.

[12] S. M. Baer and T. Erneux, *Singular Hopf bifurcation to relaxation oscillations*, SIAM J. Appl. Math., 46 (1986), pp. 721–739.

[13] S. M. Baer and T. Erneux, *Singular Hopf bifurcation to relaxation oscillations* II, SIAM J. Appl. Math., 52 (1992), pp. 1651–1664.

[14] S. M. Baer, T. Erneux, and J. Rinzel, *The slow passage through a Hopf bifurcation: Delay, memory effects, and resonance*, SIAM J. Appl. Math., 49 (1989), pp. 55–71.

[15] D. Bakes, L. Schreiberova, I. Schreiber, and M. J. B. Hauser, *Mixed-mode oscillations in a homogeneous PH-oscillatory chemical reaction system*, Chaos, 18 (2008), 015102.

[16] D. Barkley, *Slow manifolds and mixed-mode oscillations in the Belousov-Zhabotinskii reaction*, J. Chem. Phys., 89 (1988), pp. 5547–5559.

[17] D. Barkley, *Linear stability analysis of rotating spiral waves in excitable media*, Phys. Rev. Lett., 68 (1992), pp. 2090–2093.

[18] B. P. Belousov, *A periodically acting reaction and its mechanism*, in Collection of Short Papers on Radiation Medicine for 1958, Med. Publ., Moscow, 1959, pp. 145–147.

[19] É. Benoît, *Systems lents-rapides dans $\mathbb{R}^3$ et leurs canards*, in Proceedings of the Third Schnepfenried Geometry Conference, Vol. 2, Soc. Math. France, 1982, pp. 159–191.

[20] É. Benoît, *Enlacements de canards*, C.R. Acad. Sci. Paris, 300 (1985), pp. 225–230.

[21] É. Benoît, *Canards et enlacements*, Inst. Hautes Études Sci. Publ. Math., 72 (1990), pp. 63–91.

[22] É. Benoît, J.-L. Callot, F. Diener, and M. Diener, *Chasse au canards*, Collect. Math., 31 (1981), pp. 37–119.

[23] É. Benoît and C. Lobry, *Les canards de $\mathbb{R}^3$*, C.R. Acad. Sci. Paris, 294 (1982), pp. 483–488.

[24] N. Berglund and B. Gentz, *Noise-Induced Phenomena in Slow-Fast Dynamical Systems: A Sample-Paths Approach*, Springer-Verlag, Berlin, New York, 2005.

[25] N. Berglund and B. Gentz, *Stochastic dynamic bifurcations and excitability*, in Stochastic Methods in Neuroscience, C. Laing and G. Lord, eds., Oxford University Press, Oxford, 2008, pp. 65–93.

[26] J. Boissonade and P. De Kepper, *Transitions from bistability to limit cycle oscillations. Theoretical analysis and experimental evidence in an open chemical system*, J. Phys. Chem., 84 (1980), pp. 501–506.

[27] B. Braaksma, *Singular Hopf bifurcation in systems with fast and slow variables*, J. Nonlinear Sci., 8 (1998), pp. 457–490.

[28] T. S. Briggs and W. C. Rauscher, *An oscillating iodine clock*, J. Chem. Educ., 50 (1973), p. 496.

[29] T. V. Bronnikova, V. R. Fed'kina, W. M. Schaffer, and L. F. Olsen, *Period-doubling bifurcations and chaos in a detailed model of the peroxidase-oxidase reaction*, J. Phys. Chem., 99 (1995), pp. 9309–9312.

[30] T. V. Bronnikova, W. M. Schaffer, and L. F. Olsen, *Nonlinear dynamics of the peroxidase-oxidase reaction.* I. *Bistability and bursting oscillations at low enzyme concentrations*, J. Phys. Chem. B, 105 (2001), pp. 310–321.

[31] M. Brøns, M. Krupa, and M. Wechselberger, *Mixed mode oscillations due to the generalized canard phenomenon*, Fields Inst. Commun., 49 (2006), pp. 39–63.

[32] S. A. Campbell, E. Stone, and T. Erneux, *Delay induced canards in a model of high speed machining*, Dyn. Syst., 24 (2009), pp. 373–392.

[33] J. Carr, *Applications of Centre Manifold Theory*, Springer-Verlag, Berlin, New York, 1981.

[34] C. Chicone, *Inertial and slow manifolds for delay differential equations*, J. Differential Equations, 190 (2003), pp. 364–406.

[35] P. Coullet, *Localized patterns and fronts in nonequilibrium systems*, Internat. J. Bifur. Chaos Appl. Sci. Engrg., 12 (2002), pp. 2445–2457.

[36] M. F. Crowley and R. J. Field, *Electrically coupled Belousov-Zhabotinsky oscillators: A potential chaos generator*, in Nonlinear Phenomena in Chemical Dynamics, C. Vidal and A. Pacault, eds., Springer-Verlag, Berlin, New York, 1981, pp. 147–153.

[37] H. Degn, L. F. Olsen, and J. W. Perram, *Bistability, oscillation, and chaos in an enzyme reaction*, Ann. New York Acad. Sci., 316 (1979), pp. 623–637.

[38] P. De Kepper and J. Boissonade, *From bistability to sustained oscillations in homogeneous chemical systems in flow reactor mode*, in Oscillations and Traveling Waves in Chemical Systems, R. J. Field and M. Burger, eds., Wiley-Interscience, New York, 1985, pp. 223–256.

[39] P. De Kepper and I. R. Epstein, *A mechanistic study of oscillations and bistability in the Briggs-Rauscher reaction*, J. A. Chem. Soc., 104 (1982), pp. 49–55.

[40] C. A. del Negro, C. G. Wilson, R. J. Butera, H. Rigatto, and J. C. Smith, *Periodicity, mixed-mode oscillations, and quasiperiodicity in a rhythm-generating neural network*, Biophys. J., 82 (2002), pp. 206–214.

[41] W. de Melo and S. van Strien, *One-Dimensional Dynamics*, Springer-Verlag, Berlin, New York, 1993.

[42] M. Desroches, B. Krauskopf, and H. M. Osinga, *Mixed-mode oscillations and slow manifolds in the self-coupled FitzHugh-Nagumo system*, Chaos, 18 (2008), 015107.

[43] M. Desroches, B. Krauskopf, and H. M. Osinga, *The geometry of slow manifolds near a folded node*, SIAM J. Appl. Dyn. Syst., 7 (2008), pp. 1131–1162.

[44] M. Desroches, B. Krauskopf, and H. M. Osinga, *The geometry of mixed-mode oscillations in the Olsen model for the perioxidase-oxidase reaction*, Discrete Contin. Dyn. Syst. Ser. S, 2 (2009), pp. 807–827.

[45] M. Desroches, B. Krauskopf, and H. M. Osinga, *Numerical continuation of canard orbits in slow-fast dynamical systems*, Nonlinearity, 23 (2010), pp. 739–765.

[46] A. Dhooge, W. Govaerts, and Yu. A. Kuznetsov, *MatCont: A MATLAB package for numerical bifurcation analysis of ODEs*, ACM Trans. Math. Software, 29 (2003), pp. 141–164. Available online from http://sourceforge.net/projects/matcont.

[47] C. T. Dickson, J. Magistretti, M. H. Shalinsky, E. Fransen, M. E. Hasselmo, and A. Alonso, *Properties and role of $I_h$ in the pacing of subthreshold oscillations in entorhinal cortex layer* II *neurons*, J. Neurophysiol., 83 (2000), pp. 2562–2579.

[48] C. T. Dickson, J. Magistretti, M. H. Shalinsky, B. Hamam, and A. Alonso, *Oscillatory activity in entorhinal neurons and circuits: Mechanisms and function*, Ann. New York Acad. Sci., 911 (2006), pp. 127–150.

[49] F. Diener and M. Diener, *Nonstandard Analysis in Practice*, Springer-Verlag, Berlin, New York, 1995.

[50] M. Diener, *The canard unchained or how fast/slow dynamical systems bifurcate*, Math. Intelligencer, 6 (1984), pp. 38–48.

[51] E. J. Doedel, *Lecture notes on numerical analysis of nonlinear equations*, in Numerical Continuation Methods for Dynamical Systems: Path Following and Boundary Value Problems, B. Krauskopf, H. M. Osinga, and J. Galán-Vioque, eds., Springer-Verlag, Berlin, New York, 2007, pp. 117–154.

[52] E. J. Doedel, R. C. Paffenroth, A. C. Champneys, T. F. Fairgrieve, Yu. A. Kuznetsov, B. E. Oldeman, B. Sandstede, and X. J. Wang, *AUTO-07p: Continuation and Bifurcation Software for Ordinary Differential Equations*, http://cmvl.cs.concordia.ca/auto/.

[53] E. J. Doedel, B. E. Oldeman, and C. L. Pando L., *Bifurcation structures in a model of a $CO_2$ laser with a fast saturable absorber*, Internat. J. Bifur. Chaos Appl. Sci. Engrg., 21 (2011), pp. 305–322.

[54] S. Doi, J. Inoue, and S. Kumagai, *Chaotic spiking in the Hodgkin–Huxley nerve model with slow inactivation in the sodium current*, J. Integr. Neurosci., 3 (2004), pp. 207–225.

[55] J. Drover, J. Rubin, J. Su, and B. Ermentrout, *Analysis of a canard mechanism by which excitatory synaptic coupling can synchronize neurons at low firing frequencies*, SIAM J. Appl. Math., 65 (2004), pp. 69–92.

[56] J. L. A. Dubbeldam, B. Krauskopf, and D. Lenstra, *Excitability and coherence resonance in lasers with saturable absorber*, Phys. Rev. E, 60 (1999), pp. 6580–6588.

[57] F. Dumortier and R. Roussarie, *Canard cycles and center manifolds*, Mem. Amer. Math. Soc., 577 (1996).

[58] W. Eckhaus, *Relaxation oscillations including a standard chase on French ducks*, in Asymptotic Analysis II, Lecture Notes in Math. 985, Springer-Verlag, Berlin, 1983, pp. 449–494.

[59] M. Eiswirth and G. Ertl, *Kinetic oscillations in the catalytic CO oxidation on a Pt*(110) *surface*, Surf. Sci., 177 (1986), pp. 90–100.

[60] M. Eiswirth, K. Krischer, and G. Ertl, *Nonlinear dynamics in the CO-oxidation on Pt single crystal surfaces*, Appl. Phys. A, 51 (1990), pp. 79–90.

[61] J. P. England, B. Krauskopf, and H. M. Osinga, *Computing one-dimensional global manifold of Poincaré maps by continuation*, SIAM J. Appl. Dyn. Syst., 4 (2005), pp. 1008–1041.

[62] J. P. England, B. Krauskopf, and H. M. Osinga, *Computing two-dimensional global invariant manifolds in slow-fast systems*, Internat. J. Bifur. Chaos Appl. Sci. Engrg., 17 (2007), pp. 805–822.

[63] I. ERCHOVA AND D. J. MCGONIGLE, *Rhythms of the brain: An examination of mixed mode oscillation approaches to the analysis of neurophysiological data*, Chaos, 18 (2008), 015115.

[64] A. ERISIR, D. LAU, B. RUDY, AND C. S. LEONARD, *Function of specific $K^+$ channels in sustained high-frequency firing of fast-spiking interneurons*, J. Neurophysiol., 82 (1999), pp. 2476–2489.

[65] B. ERMENTROUT AND M. WECHSELBERGER, *Canards, clusters and synchronization in a weakly coupled interneuron model*, SIAM J. Appl. Dyn. Syst., 8 (2009), pp. 253–278.

[66] V. R. FED′KINA, F. I. ATAULLAKHANOV, AND T. V. BRONNIKOVA, *Computer simulations of sustained oscillations in the peroxidase-oxidase reaction*, Biophys. Chem., 19 (1984), pp. 259–264.

[67] V. R. FED′KINA, F. I. ATAULLAKHANOV, AND T. V. BRONNIKOVA, *Stimulated regimens in the peroxidase-oxidase reaction*, Theoret. Exp. Chem., 24 (1988), pp. 172–178.

[68] N. FENICHEL, *Persistence and smoothness of invariant manifolds for flows*, Indiana Univ. Math. J., 21 (1971), pp. 193–225.

[69] N. FENICHEL, *Asymptotic stability with rate conditions*, Indiana Univ. Math. J., 23 (1974), pp. 1109–1137.

[70] N. FENICHEL, *Asymptotic stability with rate conditions* II, Indiana Univ. Math. J., 26 (1977), pp. 81–93.

[71] N. FENICHEL, *Geometric singular perturbation theory for ordinary differential equations*, J. Differential Equations, 31 (1979), pp. 53–98.

[72] R. J. FIELD, E. KÖRÖS, AND R. M. NOYES, *Oscillations in chemical systems* II. *Thorough analysis of temporal oscillations in the $Ce$-$BrO_3$-malonic acid system*, J. Amer. Chem. Soc., 94 (1972), pp. 8649–8664.

[73] R. J. FIELD AND R. M. NOYES, *Oscillations in chemical systems* IV. *Limit cycle behavior in a model of a real chemical reaction*, J. Chem. Phys., 60 (1974), pp. 1877–1884.

[74] S. J. FRASER, *The steady state and equilibrium approximations: A geometrical picture*, J. Chem. Phys., 88 (1988), pp. 4732–4738.

[75] S. D. FURROW, *Chemical oscillators based on iodate ion and hydrogen peroxide*, in Oscillations and Traveling Waves in Chemical Systems, R. J. Field and M. Burger, eds., Wiley-Interscience, New York, 1985, pp. 171–192.

[76] P. GASPARD AND G. NICOLIS, *What can we learn from homoclinic orbits in chaotic dynamics?*, J. Statist. Phys., 31 (1983), pp. 499–518.

[77] P. GASPARD AND X.-J. WANG, *Homoclinic orbits and mixed-mode oscillations in far-from-equilibrium systems*, J. Statist. Phys., 48 (1987), pp. 151–199.

[78] T. GEEST, C. G. STEINMETZ, R. LARTER, AND L. F. OLSEN, *Period-doubling bifurcations and chaos in an enzyme reaction*, J. Phys. Chem., 96 (1992), pp. 5678–5680.

[79] W. GEISELER AND H. H. FÖLLNER, *Three steady state situation in an open chemical reaction system.* I, Biophys. Chem., 6 (1977), pp. 107–115.

[80] M. GOLUBITSKY, K. JOSIĆ, AND T. J. KAPER, *An unfolding theory approach to bursting in fast-slow systems*, in Analysis of Dynamical Systems: Festschrift dedicated to Floris Takens on the occasion of his 60th birthday, H. W. Broer, B. Krauskopf, and G. Vegter, eds., Institute of Physics Publ., Bristol, 2001, pp. 277–308.

[81] S. V. GONCHENKO, D. V. TURAEV, P. GASPARD, AND G. NICOLIS, *Complexity in the bifurcation structure of homoclinic loops to a saddle-focus*, Nonlinearity, 10 (1997), pp. 409–423.

[82] A. GORYACHEV, P. STRIZHAK, AND R. KAPRAL, *Slow manifold structure and the emergence of mixed-mode oscillations*, J. Chem. Phys., 107 (1997), pp. 2881–2889.

[83] D. GOULDING, S. P. HEGARTY, O. RASSKAZOV, S. MELNIK, M. HARTNETT, G. GREENE, J. G. MCINERNEY, D. RACHINSKII, AND G. HUYET, *Excitability in a quantum dot semiconductor laser with optical injection*, Phys. Rev. Lett., 98 (2007), 153903.

[84] P. GRAY, J. F. GRIFFITHS, S. M. HASKO, AND P.-G. LIGNOLA, *Oscillatory ignitions and cool flames accompanying the non-isothermal oxidation of acetaldehyde in a well stirred, flow reactor*, Proc. R. Soc. Lond., 374 (1981), pp. 313–339.

[85] K. R. GRAZIANI, J. L. HUDSON, AND R. A. SCHMITZ, *The Belousov-Zhabotinskii reaction in a continuous flow reactor*, Chem. Engrg. J., 12 (1976), pp. 9–21.

[86] J. GUCKENHEIMER, *Return maps of folded nodes and folded saddle-nodes*, Chaos, 18 (2008), 015108.

[87] J. GUCKENHEIMER, *Singular Hopf bifurcation in systems with two slow variables*, SIAM J. Appl. Dyn. Syst., 7 (2008), pp. 1355–1377.

[88] J. GUCKENHEIMER AND R. HAIDUC, *Canards at folded nodes*, Moscow Math. J., 25 (2005), pp. 91–103.

[89] J. GUCKENHEIMER, R. HARRIS-WARRICK, J. PECK, AND A. R. WILLMS, *Bifurcation, bursting, and spike frequency adaptation*, J. Comput. Neurosci., 4 (1997), pp. 257–277.

[90]  J. GUCKENHEIMER AND P. HOLMES, *Nonlinear Oscillations, Dynamical Systems, and Bifurcations of Vector Fields*, Springer-Verlag, Berlin, New York, 1983.

[91]  J. GUCKENHEIMER AND C. KUEHN, *Computing slow manifolds of saddle type*, SIAM J. Appl. Dyn. Syst., 8 (2009), pp. 854–879.

[92]  J. GUCKENHEIMER AND C. KUEHN, *Homoclinic orbits of the FitzHugh-Nagumo equation: The singular limit*, Discrete Contin. Dyn. Syst. Ser. S, 2 (2009), pp. 851–872.

[93]  J. GUCKENHEIMER AND C. KUEHN, *Homoclinic orbits of the FitzHugh–Nagumo equation: Bifurcations in the full system*, SIAM J. Appl. Dyn. Syst., 9 (2010), pp. 138–153.

[94]  J. GUCKENHEIMER AND C. SCHEPER, *A geometric model for mixed-mode oscillations in a chemical system*, SIAM J. Appl. Dyn. Syst., 10 (2011), pp. 92–128.

[95]  J. GUCKENHEIMER AND A. WILLMS, *Asymptotic analysis of subcritical Hopf-homoclinic bifurcation*, Phys. D, 139 (2000), pp. 195–216.

[96]  J. HALE AND S. M. VERDUYN LUNEL, *Introduction to Functional Differential Equations*, Springer-Verlag, Berlin, New York, 1993.

[97]  M. W. HIRSCH, C. C. PUGH, AND M. SHUB, *Invariant Manifolds*, Springer-Verlag, Berlin, New York, 1977.

[98]  L. GYÖRGI, T. TURÁNYI, AND R. J. FIELD, *Mechanistic details of the oscillatory Belousov-Zhabotinskii reaction*, J. Phys. Chem., 94 (1990), pp. 7162–7170.

[99]  E. HARVEY, V. KIRK, H. M. OSINGA, J. SNEYD, AND M. WECHSELBERGER, *Understanding anomalous delays in a model of intracellular calcium dynamics*, Chaos, 20 (2010), 045104.

[100] T. HAUCK AND F. W. SCHNEIDER, *Mixed-mode and quasiperiodic oscillations in the peroxidase-oxidase reaction*, J. Phys. Chem., 97 (1993), pp. 391–397.

[101] T. HAUCK AND F. W. SCHNEIDER, *Chaos in a Farey sequence through period doubling in the peroxidase-oxidase reaction*, J. Phys. Chem., 98 (1994), pp. 2072–2077.

[102] M. J. B. HAUSER AND L. F. OLSEN, *Mixed-mode oscillations and homoclinic chaos in an enzyme reaction*, J. Chem. Soc. Faraday Trans., 92 (1996), pp. 2857–2863.

[103] M. J. B. HAUSER, L. F. OLSEN, T. V. BRONNIKOVA, AND W. M. SCHAFFER, *Routes to chaos in the peroxdiase-oxidase reaction: Period-doubling and period-adding*, J. Phys. Chem. B, 101 (1997), pp. 5075–5083.

[104] M. HENDERSON, *Multiple parameter continuation: Computing implicitly defined k-manifolds*, Internat. J. Bifur. Chaos Appl. Sci. Engrg., 12 (2002), pp. 451–476.

[105] A. L. HODGKIN AND A. F. HUXLEY, *A quantitative description of membrane current and its application to conduction and excitation in nerve*, J. Physiology, 117 (1952), pp. 500–544.

[106] J. L. HUDSON, M. HART, AND D. MARINKO, *An experimental study of multiple peak periodic and nonperiodic oscillations in the Belousov-Zhabotinskii reaction*, J. Chem. Phys., 71 (1979), pp. 1601–1606.

[107] J. L. HUDSON, J. MANKIN, J. MCCULLOUGH, AND P. LAMBA, *Experiment on chaos in a continuous stirred reactor*, in Nonlinear Phenomena in Chemical Dynamics, C. Vidal and A. Pacault, eds., Springer-Verlag, Berlin, New York, 1981, pp. 44–48.

[108] J. L. HUDSON AND J. C. MANKIN, *Chaos in the Belousov-Zhabotinskii reaction*, J. Chem. Phys., 74 (1981), pp. 6171–6177.

[109] Y.-F. HUNG, I. SCHREIBER, AND J. ROSS, *New reaction mechanism for the oscillatory peroxidase-oxidase reaction and comparison with experiments*, J. Phys. Chem., 99 (1995), pp. 1980–1987.

[110] P. IBISON AND K. SCOTT, *Detailed bifurcation structure and new mixed-mode oscillations of the Belousov-Zhabotinskii reaction in a stirred flow reactor*, J. Chem. Soc. Faraday Trans., 86 (1990), pp. 3695–3700.

[111] E. IZHIKEVICH, *Neural excitability, spiking, and bursting*, Internat. J. Bifur. Chaos Appl. Sci. Engrg., 10 (2000), pp. 1171–1266.

[112] J. JALICS, M. KRUPA, AND H. G. ROTSTEIN, *Mixed-mode oscillations in a three time-scale system of ODEs motivated by a neuronal model*, Dyn. Syst., 25 (2010), pp. 445–482

[113] C. K. R. T. JONES, *Geometric singular perturbation theory*, in Dynamical Systems (Montecatini Terme, 1994), Springer-Verlag, Berlin, New York, 1995, pp. 44–118.

[114] T. J. KAPER, *An introduction to geometric methods and dynamical systems theory for singular perturbation problems. Analyzing multiscale phenomena using singular perturbation methods*, Proc. Sympos. Appl. Math., 56 (1999), pp. 85–131.

[115] T. J. KAPER AND C. K. R. T. JONES, *A primer on the exchange lemma for fast-slow systems*, in Multiple-Time-Scale Dynamical Systems (Minneapolis, MN, 1997), IMA Vol. Math. Appl. 122, Springer, New York, 2001, pp. 65–88.

[116] A. L. KAWCZYNSKI, V. O. KHAVRUS, AND P. E. STRIZHAK, *Complex mixed-mode periodic and chaotic oscillations in a simple three-variable model of nonlinear system*, Chaos, 10 (2000), pp. 299–310.

[117] A. L. KAWCZYNSKI AND P. E. STRIZHAK, *Period adding and broken Farey tree sequences of bifurcations for mixed-mode oscillations and chaos in the simplest three-variable nonlinear system*, J. Chem. Phys., 112 (2000), pp. 6122–6130.

[118] J. KEENER AND J. SNEYD, *Mathematical Physiology*, Interdiscip. Appl. Math. 8, Springer-Verlag, Berlin, New York, 1998.

[119] J. KEVORKIAN AND J. D. COLE, *Multiple Scale and Singular Perturbation Methods*, Springer-Verlag, Berlin, New York, 1996.

[120] V. O. KHAVRUS, H. FARKAS, AND P. E. STRIZHAK, *Conditions for mixed-mode oscillations and deterministic chaos in nonlinear chemical systems*, Theoret. Exp. Chem., 38 (2002), pp. 301–307.

[121] K.-R. KIM, D. J. LEE, AND K. J. SHIN, *A simplified model for the Briggs-Rauscher reaction mechanism*, J. Chem. Phys., 117 (2002), pp. 2710–2717.

[122] K.-R. KIM, K. J. SHIN, AND D. J. LEE, *Complex oscillations in a simple model for the Briggs-Rauscher reaction*, J. Chem. Phys., 121 (2004), pp. 2664–2672.

[123] M. T. M. KOPER, *Bifurcations of mixed-mode oscillations in a three-variable autonomous Van der Pol-Duffing model with a cross-shaped phase diagram*, Phys. D, 80 (1995), pp. 72–94.

[124] M. T. M. KOPER AND P. GASPARD, *Mixed-mode and chaotic oscillations in a simple model of an electrochemical oscillator*, J. Chem. Phys., 95 (1991), pp. 4945–4947.

[125] M. T. M. KOPER AND P. GASPARD, *The modeling of mixed-mode and chaotic oscillations in electrochemical systems*, J. Chem. Phys., 96 (1992), pp. 7797–7813.

[126] M. T. M. KOPER, P. GASPARD, AND J. H. SLUYTERS, *Mixed-mode oscillations and incomplete homoclinic scenarios to a saddle-focus in the indium/thiocyanate electrochemical oscillator*, J. Chem. Phys., 97 (1992), pp. 8250–8260.

[127] M. T. M. KOPER AND J. H. SLUYTERS, *Electrochemical oscillators: An experimental study of the indium/thiocyanate oscillator*, J. Electroanal. Chem., 303 (1991), pp. 65–72.

[128] M. T. M. KOPER AND J. H. SLUYTERS, *Electrochemical oscillators: Their description through a mathematical model*, J. Electroanal. Chem., 303 (1991), pp. 73–94.

[129] K. KOVACS, M. LEDA, V. K. VANAG, AND I. R. EPSTEIN, *Small-amplitude and mixed-mode oscillations in the bromate-sulfite-ferrocyanide-aluminium* (III) *system*, J. Phys. Chem., 113 (2009), pp. 146–156.

[130] B. KRAUSKOPF AND B. E. OLDEMAN, *Bifurcations of global reinjection orbits near a saddle-node Hopf bifurcation*, Nonlinearity, 19 (2006), pp. 2149–2167.

[131] B. KRAUSKOPF AND H. M. OSINGA, *Computing geodesic level sets on global (un)stable manifolds of vector fields*, SIAM J. Appl. Dyn. Syst., 2 (2003), pp. 546–569.

[132] B. KRAUSKOPF AND H. M. OSINGA, *Computing invariant manifolds via the continuation of orbit segments*, in Numerical Continuation Methods for Dynamical Systems: Path Following and Boundary Value Problems, B. Krauskopf, H. M. Osinga, and J. Galán-Vioque, eds., Springer-Verlag, Berlin, New York, 2007, pp. 117–154.

[133] B. KRAUSKOPF, H. M. OSINGA, E. DOEDEL, M. HENDERSON, J. GUCKENHEIMER, A. VLADI-MIRSKY, M. DELLNITZ, AND O. JUNGE, *A survey of methods for computing (un)stable manifolds of vector fields*, Internat. J. Bifur. Chaos Appl. Sci. Engrg., 15 (2005), pp. 763–792.

[134] B. KRAUSKOPF, K. R. SCHNEIDER, J. SIEBER, S. M. WIECZOREK, AND M. WOLFRUM, *Excitability and self-pulsations near homoclinic bifurcations in semiconductor laser systems*, Optics Communications, 215 (2003), pp. 367–379.

[135] B. KRAUSKOPF AND T. RIESS, *A Lin's method approach to finding and continuing heteroclinic connections involving periodic orbits*, Nonlinearity, 21 (2008), pp. 1655–1690.

[136] B. KRAUSKOPF AND S. M. WIECZOREK, *Accumulating regions of winding periodic orbits in optically driven lasers*, Phys. D, 173 (2002), pp. 97–113.

[137] K. KRISCHER, M. EISWIRTH, AND G. ERTL, *Oscillatory CO oxidation on Pt*(110): *Modeling of temporal self-organization*, J. Chem. Phys., 96 (1992), pp. 9161–9172.

[138] K. KRISCHER, M. LUEBKE, M. EISWIRTH, W. WOLF, J. L. HUDSON, AND G. ERTL, *A hierarchy of transitions to mixed mode oscillations in an electrochemical system*, Phys. D, 62 (1993), pp. 123–133.

[139] M. KRUPA, N. POPOVIĆ, AND N. KOPELL, *Mixed-mode oscillations in three time-scale systems: A prototypical example*, SIAM J. Appl. Dyn. Syst., 7 (2008), pp. 361–420.

[140] M. KRUPA, N. POPOVIĆ, N. KOPELL, AND H. G. ROTSTEIN, *Mixed-mode oscillations in a three time-scale model for the dopaminergic neuron*, Chaos, 18 (2008), 015106.

[141] M. KRUPA AND P. SZMOLYAN, *Extending geometric singular perturbation theory to nonhyperbolic points—fold and canard points in two dimensions*, SIAM J. Math. Anal., 33 (2001), pp. 286–314.

[142] M. KRUPA AND P. SZMOLYAN, *Extending slow manifolds near transcritical and pitchfork singularities*, Nonlinearity, 14 (2001), pp. 1473–1491.

[143] M. Krupa and P. Szmolyan, *Relaxation oscillation and canard explosion*, J. Differential Equations, 174 (2001), pp. 312–368.

[144] M. Krupa and M. Wechselberger, *Local analysis near a folded saddle-node singularity*, J. Differential Equations, 248 (2010), pp. 2841–2888.

[145] C. Kuehn, *From first Lyapunov coefficients to maximal canards*, Internat. J. Bifur. Chaos Appl. Sci. Engrg., 20 (2010), pp. 1467–1475.

[146] R. Kuske and R. Borowski, *Survival of subthreshold oscillations: The interplay of noise, bifurcation structure, and return mechanism*, Discrete Contin. Dyn. Syst. Ser. S, 2 (2009), pp. 873–895.

[147] R. Kuske, R. Borowski, Y.-X. Li, and J. L. Cabrera, *Characterizing mixed mode oscillations shaped by noise and bifurcation structure*, Chaos, 20 (2010), 043117.

[148] Yu. A. Kuznetsov, *Elements of Applied Bifurcation Theory*, 3rd ed., Springer-Verlag, Berlin, New York, 2004.

[149] P. A. Lagerstrom, *Matched Asymptotic Expansions: Ideas and Techniques*, Springer-Verlag, Berlin, New York, 1988.

[150] B. Láňová and J. Vřešťál, *Study of the Bray-Liebhafsky reaction by on-line mass spectrometry*, J. Phys. Chem. A, 106 (2002), pp. 1228–1232.

[151] R. Larter, C. L. Bush, T. R. Lonis, and B. D. Aguda, *Multiple steady states, complex oscillations, and the devil's staircase in the peroxidase-oxidase reaction*, J. Chem. Phys., 87 (1987), pp. 5765–5771.

[152] R. Larter and S. Hemkin, *Further refinements of the peroxidase-oxidase oscillator mechanism: Mixed-mode oscillations and chaos*, J. Phys. Chem., 100 (1996), pp. 18924–18930.

[153] R. Larter and C. G. Steinmetz, *Chaos via mixed-mode oscillations*, Phil. Trans. R. Soc. Lond. A, 337 (1991), pp. 291–298.

[154] R. Larter, C. G. Steinmetz, and B. Aguda, *Fast-slow variable analysis of the transition to mixed-mode oscillations and chaos in the peroxidase reaction*, J. Chem. Phys., 89 (1988), pp. 6506–6514.

[155] D. Lindberg, J. S. Turner, and D. Barkley, *Chaos in the Showalter-Noyes-Bar-Eli model of the Belousov-Zhabotinskii reaction*, J. Chem. Phys., 92 (1990), pp. 3238–3239.

[156] J. Masełko, *Experimental studies of complicated oscillations. The system $Mn^{2+}$-malonic acid-$KBrO_3$-$H_2SO_4$*, Chem. Phys., 51 (1980), pp. 473–480.

[157] J. Masełko and H. L. Swinney, *A complex transition sequence in the Belousov-Zhabotinskii reaction*, Phys. Scripta, T9 (1985), pp. 35–39.

[158] J. Masełko and H. L. Swinney, *A Farey triangle in the Belousov-Zhabotinskii reaction*, Phys. Lett. A, 119 (1986), pp. 403–406.

[159] J. Masełko and H. L. Swinney, *Complex periodic oscillation and Farey arithmetic in the Belousov-Zhabotinskii reaction*, J. Chem. Phys., 85 (1986), pp. 6430–6441.

[160] G. S. Medvedev and J. E. Cisternas, *Multimodal regimes in a compartmental model of the dopamine neuron*, Phys. D, 194 (2004), pp. 333–356.

[161] M. Mikikian, M. Cavarroc, L. Couedel, Y. Tessier, and L. Boufendi, *Mixed-mode oscillations in complex plasma instabilities*, Phys. Rev. Lett., 100 (2008), 225005.

[162] A. Milik and P. Szmolyan, *Multiple time scales and canards in a chemical oscillator*, in Multiple-Time-Scale Dynamical Systems, C. Jones and A. Khibnik, eds., IMA Vol. Math. Appl. 122, Springer-Verlag, Berlin, New York, 2001, pp. 117–140.

[163] A. Milik, P. Szmolyan, H. Loeffelmann, and E. Groeller, *Geometry of mixed-mode oscillations in the 3-D autocatalator*, Internat. J. Bifur. Chaos Appl. Sci. Engrg., 8 (1998), pp. 505–519.

[164] K. Mischaikow, M. Mrozek, and J. F. Reineck, *Singular index pairs*, J. Dynam. Differential Equations, 11 (1999), pp. 399–425.

[165] E. F. Mishchenko and N. Kh. Rozov, *Differential Equations with Small Parameters and Relaxation Oscillations*, Plenum Press, New York, 1980 (translated from Russian).

[166] C. B. Muratov and E. Vanden-Eijnden, *Noise-induced mixed-mode oscillations in a relaxation oscillator near the onset of a limit cycle*, Chaos, 18 (2008), 015111.

[167] J. Nagumo, S. Arimoto, and S. Yoshizawa, *An active pulse transmission line simulating nerve axon*, Proc. IRE, 50 (1962), pp. 2061–2070.

[168] G. Neher, L. Pohlmann, and H. Tributsch, *Mixed-mode oscillations, self-similarity, and time-transient chaotic behaviour in the (photo-) electrochemical system $p - CuInSe_2/H_2O_2$*, J. Phys. Chem., 99 (1995), pp. 17763–17771.

[169] A. I. Neishtadt, *Asymptotic investigation of the loss of stability as a pair of eigenvalues slowly cross the imaginary axis*, Uspekhi Mat. Nauk, 40 (1985), pp. 190–191.

[170] J. Nowacki, S. H. Mazlan, H. M. Osinga, and K. T. Tsaneva-Atanasova, *The role of large-conductance calcium-activated $K^+$ (BK) channels in shaping bursting oscillations of a somatotroph cell model*, Phys. D, 239 (2010), pp. 485–493.

[171] R. M. Noyes and S. D. Furrow, *The oscillatory Briggs-Rauscher reaction. 3. A skeleton mechanism for oscillations*, J. Amer. Chem. Soc., 104 (1982), pp. 45–48.

[172] N. Okazaki and I. Hanazaki, *Photo-induced chaos in the Briggs-Rauscher reaction*, J. Chem. Phys., 109 (1998), pp. 637–642.

[173] L. F. Olsen, *An enzyme reaction with a strange attractor*, Phys. Lett. A, 94 (1983), pp. 454–457.

[174] L. F. Olsen and H. Degn, *Oscillatory kinetics of the peroxidase-oxidase reaction in an open system. Experimental and theoretical studies*, Biochim. Biophys. Acta, 523 (1978), pp. 321–334.

[175] D. L. Olson, E. P. Williksen, and A. Scheeline, *An experimentally based model of the Peroxidase-NADH biochemical oscillator: An enzyme-mediated chemical switch*, J. Amer. Chem. Soc., 117 (1995), pp. 2–15.

[176] F. W. J. Olver, D. W. Lozier, R. F. Boisvert, and C. W. Clark, *NIST Handbook of Mathematical Functions*, Cambridge University Press, Cambridge, UK, 2010.

[177] M. Orban and I. R. Epstein, *Chemical oscillators in group VIA: The Cu(II)-catalyzed reaction between hydrogen peroxide and thiosulfate ion*, J. Amer. Chem. Soc., 109 (1987), pp. 101–106.

[178] M. Orban, K. Kurin-Csorgei, G. Rabai, and I. R. Epstein, *Mechanistic studies of oscillatory copper(II) catalyzed oxidation reactions of sulfur compounds*, Chem. Eng. Sci., 55 (2000), pp. 267–273.

[179] C. L. Pando L., *Recurrent synchronism in the internal dynamics of $CO_2$ lasers*, Phys. Lett. A, 210 (1996), pp. 391–401.

[180] E. Peacock-Lopez, D. B. Radov, and C. S. Flesner, *Mixed-mode oscillations in a self-replicating dimerization mechanism*, Biophys. Chem., 65 (1997), pp. 171–178.

[181] B. Peng, V. Gaspar, and K. Showalter, *False bifurcations in chemical systems: Canards*, Phil. Trans. R. Soc. Lond. A, 337 (1991), pp. 275–289.

[182] V. Petrov, S. K. Scott, and K. Showalter, *Mixed-mode oscillations in chemical systems*, J. Chem. Phys., 97 (1992), pp. 6191–6198.

[183] F. Plenge, H. Varela, and K. Krischer, *Asymmetric target patterns in one-dimensional oscillatory media with genuine nonlocal coupling*, Phys. Rev. Lett., 94 (2005), 198301.

[184] L. Pohlmann, G. Neher, and H. Tributsch, *A model for oscillating hydrogen liberation at $CuInSe_2$ in the presence of $H_2O_2$*, J. Phys. Chem., 98 (1994), pp. 11007–11010.

[185] Y. Pomeau, J.-C. Roux, A. Rossi, S. Bachelart, and C. Vidal, *Intermittent behaviour in the Belousov-Zhabotinsky reaction*, J. Phys. Lett., 42 (1981), pp. 271–273.

[186] M. Rachwalska and A. L. Kawczynski, *New types of mixed-mode oscillations in the Belousov-Zhabotinsky reaction in continuously stirred tank reactors*, J. Chem. Phys. A, 103 (1999), pp. 3455–3457.

[187] M. Rachwalska and A. L. Kawczynski, *Period-adding bifurcations in mixed-mode oscillations in the Belousov-Zhabotinsky reaction at various residence times in a CTSR*, J. Chem. Phys. A, 105 (2001), pp. 7885–7888.

[188] P. Richetti, J. C. Roux, F. Argoul, and A. Arneodo, *From quasiperiodicity to chaos in the Belousov-Zhabotinskii reaction. II. Modeling and theory*, J. Chem. Phys., 86 (1987), pp. 3339–3355.

[189] J. Rinzel, *A formal classification of bursting mechanisms in excitable systems*, in Proceedings of the International Congress of Mathematicians (Berkeley, CA, 1986), AMS, Providence, RI, 1987, pp. 1578–1593.

[190] J. Rinzel and I. B. Schwartz, *One variable map prediction of the Belousov-Zhabotinskii mixed mode oscillations*, J. Chem. Phys., 80 (1984), pp. 5610–5615.

[191] O. E. Rössler, *Different types of chaos in two simple differential equations*, Z. Naturforschung Teil A, 31 (1976), p. 1664.

[192] O. E. Rössler, *Different types of chaos in two simple differential equations*, Bull. Math. Biol., 39 (1977), pp. 275–289.

[193] H. G. Rotstein, T. Oppermann, J. A. White, and N. Kopell, *The dynamic structure underlying subthreshold oscillatory activity and the onset of spikes in a model of medial entorhinal cortex stellate cells*, J. Comput. Neurosci., 21 (2006), pp. 271–292.

[194] H. G. Rotstein, M. Wechselberger, and N. Kopell, *Canard induced mixed-mode oscillations in a medial entorhinal cortex layer II stellate cell model*, SIAM J. Appl. Dyn. Syst., 7 (2008), pp. 1582–1611.

[195] J.-C. Roux, A. Rossi, S. Bachelart, and C. Vidal, *Experimental observations of complex dynamical behaviour during a chemical reaction*, Phys. D, 2 (1981), pp. 395–403.

[196] J.-C. Roux, R. H. Simoyi, and H. L. Swinney, *Observation of a strange attractor*, Phys. D, 8 (1983), pp. 257–266.

[197] J.-C. Roux and H. L. Swinney, *Topology of chaos in a chemical reaction*, in Nonlinear Phenomena in Chemical Dynamics, C. Vidal and A. Pacault, eds., Springer-Verlag, Berlin, New York, 1981, pp. 38–43.

[198] J. Rubin and M. Wechselberger, *Giant squid—hidden canard: The 3D geometry of the Hodgkin-Huxley model*, Biol. Cyb., 97 (2007), pp. 5–32.

[199] J. Rubin and M. Wechselberger, *The selection of mixed-mode oscillations in a Hodgkin-Huxley model with multiple timescales*, Chaos, 18 (2008), 015105.

[200] W. M. Schaffer, T. V. Bronnikova, and L. F. Olsen, *Nonlinear dynamics of the peroxidase-oxidase reaction. II. Compatibility of an extended model with previously reported model-data correspondences*, J. Phys. Chem., 105 (2001), pp. 5331–5340.

[201] A. Scheeline, D. L. Olson, E. P. Williksen, G. A. Horras, M. L. Klein, and R. Larter, *The peroxidase-oxidase oscillator and its constituent chemistries*, Chem. Rev., 97 (1997), pp. 739–756.

[202] M. Schell and F. N. Albahadily, *Mixed-mode oscillations in an electrochemical system. II. A periodic-chaotic sequence*, J. Chem. Phys., 90 (1989), pp. 822–828.

[203] S. Schmidt and P. Ortoleva, *Electric field effects on propagating BZ waves: Predictions of an Oregonator and new pulse supporting models*, J. Chem. Phys., 74 (1981), pp. 4488–4500.

[204] R. A. Schmitz, K. R. Graziani, and J. L. Hudson, *Experimental evidence of chaotic states in the Belousov-Zhabotinskii reaction*, J. Chem. Phys., 67 (1977), pp. 3040–3044.

[205] S. K. Scott, *Oscillations, Waves, and Chaos in Chemical Kinetics*, Oxford University Press, Oxford, 1994.

[206] L. P. Shil′nikov, *A case of the existence of a denumerable set of periodic motions*, Soviet Math. Dokl, 6 (1965), pp. 163–166.

[207] K. Showalter, R. M. Noyes, and K. Bar-Eli, *A modified Oregonator model exhibiting complicated limit cycle behaviour in a flow system*, J. Chem. Phys., 69 (1978), pp. 2514–2524.

[208] K. Sriram and M. S. Gopinathan, *Effects of delayed linear electrical perturbation of the Belousov-Zhabotinsky reaction: A case of complex mixed mode oscillations in a batch reactor*, React. Kinet. Catal. Lett., 79 (2003), pp. 341–349.

[209] C. G. Steinmetz, T. Geest, and R. Larter, *Universality in the peroxidase-oxidase reaction: Period doublings, chaos, period three, and unstable limit cycles*, J. Phys. Chem., 97 (1993), pp. 5649–5653.

[210] C. G. Steinmetz and R. Larter, *The quasiperiodic route to chaos in a model of the peroxidase-oxidase reaction*, J. Phys. Chem., 94 (1991), pp. 1388–1396.

[211] J. V. Stern, H. M. Osinga, A. LeBeau, and A. Sherman, *Resetting behavior in a model of bursting in secretory pituitary cells: Distinguishing plateaus from pseudo-plateaus*, Bull. Math. Biol., 70 (2008), pp. 68–88.

[212] M. N. Stolyarov, V. A. Romanov, and E. I. Volkov, *Out-of-phase mixed-mode oscillations of two strongly coupled identical relaxation oscillators*, Phys. Rev. E, 54 (1995), pp. 163–169.

[213] P. Szmolyan, *Transversal heteroclinic and homoclinic orbits in singular perturbation problems*, J. Differential Equations, 92 (1991), pp. 252–281.

[214] P. Szmolyan and M. Wechselberger, *Canards in $\mathbb{R}^3$*, J. Differential Equations, 177 (2001), pp. 419–453.

[215] J. Tabak, N. Toporikova, M. E. Freeman, and R. Bertram, *Low dose of dopamine may stimulate prolactin secretion by increasing fast potassium currents*, J. Comput. Neurosci., 22 (2007), pp. 211–222.

[216] F. Takens, *Constrained equations: A study of implicit differential equations and their discontinuous solutions*, in Structural Stability, the Theory of Catastrophes, and Applications in the Sciences, Lecture Notes in Math. 525, Springer-Verlag, Berlin, New York, 1976, pp. 143–243.

[217] D. Terman and E. Lee, *Uniqueness and stability of periodic bursting solutions*, J. Differential Equations, 158 (1999), pp. 48–78.

[218] A. N. Tikhonov, A. B. Vasil'eva, and A. G. Sveshnikov, *Differential Equations*, Springer Ser. Soviet Math., Springer-Verlag, Berlin, New York, 1985.

[219] K. Tomita, A. Ito, and T. Ohta, *Simplified model for Belousov-Zhabotinsky reaction*, J. Theoret. Biol., 68 (1977), pp. 459–481.

[220] P. Tracqui, *Mixed-mode oscillation genealogy in a compartmental model of bone mineral metabolism*, J. Nonlinear Sci., 4 (1994), pp. 69–103.

[221] W. C. Troy, *Mathematical analysis of the Oregonator model of the Belousov-Zhabotinskii reaction*, in Oscillations and Traveling Waves in Chemical Systems, R. J. Field and M. Burger, eds., Wiley-Interscience, New York, 1985, pp. 145–170.

[222] T. TURÁNYI, *Rate sensitivity analysis of a model of the Briggs-Rauscher reaction*, React. Kinet. Lett., 45 (1991), pp. 235–241.

[223] J. J. TYSON, *On scaling the Oregonator equations*, in Nonlinear Phenomena in Chemical Dynamics, C. Vidal and A. Pacault, eds., Springer-Verlag, Berlin, New York, 1981, pp. 222–227.

[224] J. J. TYSON, *A quantitative account of oscillations, bistability, and traveling waves in the Belousov-Zhabotinskii reaction*, in Oscillations and Traveling Waves in Chemical Systems, R. J. Field and M. Burger, eds., Wiley-Interscience, New York, 1985, pp. 93–144.

[225] B. VAN DER POL, *A theory of the amplitude of free and forced triode vibrations*, Radio Rev., 1 (1920), pp. 701–710.

[226] B. VAN DER POL, *On relaxation oscillations*, Philosophical Mag., 7 (1926), pp. 978–992.

[227] B. VAN DER POL, *The nonlinear theory of electric oscillations*, Proc. IRE, 22 (1934), pp. 1051–1086.

[228] F. VAN GOOR, D. ZIVADINOVIC, A. J. MARTINEZ-FUENTES, AND S. S. STOJILKOVIC, *Dependence of pituitary hormone secretion on the pattern of spontaneous voltage-gated calcium influx*, J. Biol. Chem., 276 (2001), pp. 33840–33846.

[229] O. VAUDEL, N. PÉRAUD, AND P. BESNARD *Synchronization on excitable pulses in optically injected semiconductor lasers*, Proc. SPIE, 6997 (2008),  0F.

[230] T. G. J. VAN VENROOIJ AND M. T. M. KOPER, *Bursting and mixed-mode oscillations during the hydrogen peroxide reduction on a platinum electrode*, Electrochimica Acta, 40 (1995), pp. 1689–1696.

[231] C. VIDAL, J.-C. ROUX, S. BACHELART, AND A. ROSSI, *Experimental study of the transition to turbulence in the Belousov-Zhabotinskii reaction*, Ann. New York Acad. Sci., 357 (1980), pp. 377–396.

[232] T. VO, R. BERTRAM, J. TABAK, AND M. WECHSELBERGER, *Mixed-mode oscillations as a mechanism for pseudo-plateau bursting*, J. Comput. Neurosci., 28 (2010), pp. 443–458.

[233] V. VUKOJEVIĆ, S. ANIĆ, AND LJ. KOLAR-ANIĆ, *Investigation of dynamic behaviour of the Bray-Liebhafsky reaction in the CSTR. Determination of bifurcation points*, J. Phys. Chem. A, 104 (2000), pp. 10731–10739.

[234] V. VUKOJEVIĆ, P. G. SØRENSEN, AND F. HYNNE, *Predictive value of a model of the Briggs-Rauscher reaction fitted to quenching experiments*, J. Phys. Chem., 100 (1996), pp. 17175–17185.

[235] G. WALLET, *Entrée-sortie dans un tourbillon*, Ann. Inst. Fourier (Grenoble), 36 (1986), pp. 157–184.

[236] M. WECHSELBERGER, *Extending Melnikov-theory to invariant manifolds on non-compact domains*, Dyn. Syst., 17 (2002), pp. 215–233.

[237] M. WECHSELBERGER, *Existence and bifurcation of canards in $\mathbb{R}^3$ in the case of a folded node*, SIAM J. Appl. Dyn. Syst., 4 (2005), pp. 101–139.

[238] M. WECHSELBERGER, *À propos de canards (apropos canards)*, Trans. Amer. Math. Soc., 364 (2012), pp. 3289–3309.

[239] M. WECHSELBERGER AND W. WECKESSER, *Bifurcations of mixed-mode oscillations in a stellate cell model*, Phys. D, 238 (2009), pp. 1598–1614.

[240] M. WECHSELBERGER AND W. WECKESSER, *Homoclinic clusters and chaos associated with a folded node in a stellate cell model*, Discrete Contin. Dyn. Syst. Ser. S, 2 (2009), pp. 829–850.

[241] S. WIECZOREK AND B. KRAUSKOPF, *Bifurcations of n-homoclinic orbits in optically injected lasers*, Nonlinearity, 18 (2006), pp. 1095–1120.

[242] A. WINFREE, *Spiral waves of chemical activity*, Science, 175 (1972), pp. 634–636.

[243] K. YOKOTA AND I. YAMAZAKI, *Analysis and computer simulation of aerobic oxidation of reduced nicotinamide adenine dinucleotide catalyzed by horseradish peroxidase*, Biochemistry, 16 (1977), pp. 1913–1920.

[244] N. YU, R. KUSKE, AND Y. X. LI, *Stochastic phase dynamics and noise-induced mixed-mode oscillations in coupled oscillators*, Chaos, 18 (2008), p. 15.

[245] A. M. ZHABOTINSKII, *The early period of systematic studies of oscillations and waves in chemical systems*, in Oscillations and Traveling Waves in Chemical Systems, R. J. Field and M. Burger, eds., Wiley-Interscience, New York, 1985, pp. 1–6.